

Carnegie Mellon University
MELLON COLLEGE OF SCIENCE

THESIS

SUBMITTED IN PARTIAL FULFILLMENT OF THE REQUIREMENTS
FOR THE DEGREE OF

DOCTOR OF PHILOSOPHY IN THE FIELD OF PHYSICS

TITLE: "Inter- and Intra-particle Interactions in Magnetic Nanoparticle Systems"

PRESENTED BY: Ryan Booth

ACCEPTED BY THE DEPARTMENT OF PHYSICS

Sara Majetich
SARA MAJETICH, CHAIR PROFESSOR

9/21/12
DATE

Gregg B Franklin
GREGG FRANKLIN, DEPT HEAD

9/29/2012
DATE

APPROVED BY THE COLLEGE COUNCIL

Fred Gilman
FRED GILMAN, DEAN

9/25/12
DATE

Inter- and Intraparticle Interactions in Magnetic Nanoparticle Systems

by

Ryan Anderson Booth

Submitted in partial fulfillment of
The requirements for the degree of
Doctor of Philosophy
At
Carnegie Mellon University
Department of Physics
Pittsburgh, Pennsylvania

Advised by: Professor Sara A. Majetich

September 7, 2012

UMI Number: 3533450

All rights reserved

INFORMATION TO ALL USERS

The quality of this reproduction is dependent upon the quality of the copy submitted.

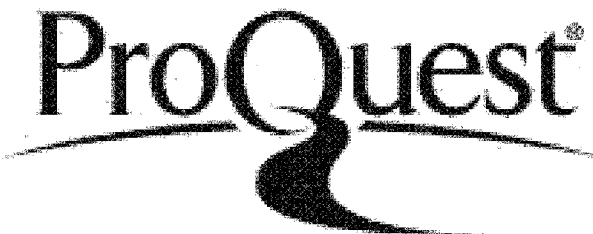
In the unlikely event that the author did not send a complete manuscript and there are missing pages, these will be noted. Also, if material had to be removed, a note will indicate the deletion.



UMI 3533450

Published by ProQuest LLC 2012. Copyright in the Dissertation held by the Author.
Microform Edition © ProQuest LLC.

All rights reserved. This work is protected against
unauthorized copying under Title 17, United States Code.



ProQuest LLC
789 East Eisenhower Parkway
P.O. Box 1346
Ann Arbor, MI 48106-1346

Abstract

We investigated deviations of magnetic nanoparticle behavior from the ideal, non-interacting behavior in the superferromagnetic regime. These deviations can be understood in greater detail by considering the magnetic components oriented orthogonally to the applied magnetic field. We demonstrated the novel measurement of the transverse magnetization of 7 nm iron oxide crystals and showed that it agrees qualitatively with the deviations between proposed interaction models and our experimental, longitudinal magnetization curves. Using polarization analyzed small angle neutron scattering (PASANS), we demonstrated the ability to probe the 3D magnetic structure in a sample of 9 nm iron oxide nanoparticle crystals, and discovered a 1.0 to 1.5 nm thick shell with the spins coherently oriented perpendicular to a 7 nm core aligned with the applied field, between temperatures of 160 K and 320 K under a nominally saturating 1.2 T field. Finally, we developed a novel synthesis for of highly monodisperse, 30 nm diameter MnO nanoparticles. These were oxidized to create an Mn_3O_4 shell of controllable thickness. We found the exchange bias parameters in this $\text{MnO}/\text{Mn}_3\text{O}_4$ core/shell system to be significantly lower than those commonly reported for the same system. We believe the anomalous literature values to be due to spin-glass like behavior and/or thermal training resulting from the use of poorly crystalline, or polycrystalline particles.

Acknowledgments

I would like to thank my advisor, Sara Majetich, for her unwavering support since the beginning of my graduate work, inspiring work ethic, and uncommon leadership. The members of her research group and our many collaborators have been a pleasure to work with.

I would like to thank all of the teachers—both professional and informal—who have helped me throughout my studies. I would especially like to thank: Bill Sheers, my undergraduate advisor, the man who set me on this path, and who reminded me, “graduate school will be the highest highs and the lowest lows of your life,” when I needed to hear it. Mike Sakash, my saxophone teacher, who helped me develop a lifelong hobby, outlet, and avenue through which I’ve met some of my closest friends. And, Mike Leichty, who taught me more about careful observation and problem solving than I have ever learned in a laboratory or classroom.

Chuck Gitzens contributions to the Carnegie Mellon community go unnoticed too often. Without his stockroom and help purchasing instruments and supplies I would likely be writing this a few years from now.

Finally, I would like to thank my family for always enthusiastically supporting me in everything that I do.

-Ryan Booth

Pittsburgh, PA
12 September 2012

Table of Contents

1. Introduction to Relevant Magnetism	1
1.1 Introduction.....	1
1.2 Diamagnetism.....	2
1.3 Paramagnetism.....	2
1.4 Ferromagnetism, antiferromagnetism, and ferrimagnetism	3
1.5 Magnetism in the context of nanoparticles	6
1.6 Magnetic nanoparticle Interactions.....	7
1.7 Exchange bias	9
1.8 References.....	11
2. Introduction to Relevant Magnetism	12
2.1 Introduction.....	12
2.2 Iron oxide particle synthesis and characterization	12
2.2.1 Particle size characterization	12
2.2.2 Magnetic characterization	15
2.2.3 Preparation of nanoparticle crystals.....	16
2.3 Magnetic Interactions	19
2.3.1 Region of interest.....	20
2.3.2 An effective field model of interactions	21
2.3.3 Discussion of effective field calculation results	24
2.3.4 Distribution of dipolar interaction fields model	24
2.4 Measurement of the transverse moment.....	27
2.5 References.....	30
3. Investigation of Intraparticle Magnetic Structure Using PASANS	31

3.1	Introduction and motivation	31
3.2	Traditional SANS Experiments.....	32
3.3	Polarization Analyzed Small Angle Neutron Scattering (PASANS)	34
3.3.1	The velocity selector.....	34
3.3.2	The supermirror	34
3.3.3	The flipper.....	36
3.3.4	The ^3He analyzer	36
3.3.5	The magnetic guide fields	37
3.4	Polarization corrections	38
3.5	Extraction of 3D magnetic structure from scattering data	40
3.6	Results and discussion.....	41
3.6.1	Interparticle interactions	41
3.6.2	Intraparticle structure.....	45
3.7	Conclusions.....	49
3.8	References.....	50
4.	Synthesis and Characterization of Highly Monodisperse, Single Crystal MnO Mn₃O₄ Nanoparticles with Variable Shell Thickness	31
4.1	Introduction.....	52
4.1.1	Exchange bias in nanoparticle systems.....	53
4.1.2	The MnO Mn ₃ O ₄ system	53
4.2	Experimental	54
4.2.1	Synthesis	54
4.2.2	Mn ₃ O ₄ shell formation	57
4.2.3	Magnetic measurements	59
4.2.4	3D self assembly	63
4.3	Discussion.....	64

4.3.1	Possible origins of anomalously high H_{ex}	64
4.3.2	Falsely attributed exchange bias	66
4.4	Conclusion	67
4.5	References.....	68
5.	Conclusions.....	70
5.1	Summary of results	70
5.2	Future work.....	71
5.3	References.....	72

List of Figures

- Figure 1.1: Schematic diagram of the spin arrangement relative to the applied field in a) a ferromagnet, b) a perfectly compensated antiferromagnet, c) an antiferromagnet showing uncompensated spins due to a missing sublattice and a vacancy, and d) a ferrimagnet.
- Figure 1.2: Schematic hysteresis loop illustrating the saturation magnetization, M_S , the remanent magnetization, M_R , the coercive field, H_C , and the coercivity which is equal to $2H_C$.
- Figure 1.3: Schematic of the Lorentz cavity field generated by a spherical hole in a uniformly magnetized material.
- Figure 1.4: Intuitive picture of exchange bias material in the context of a hysteresis loop.
- Figure 2.1: TEM image of a stained bovine liver catalase crystal recorded at 30,000x magnification. The lattice spacing is 8.75 nm parallel to the red line, and 6.85 nm perpendicular to it.
- Figure 2.2: TEM image of iron oxide nanoparticles recorded at 30,000x magnification and used to measure the particle size distribution. The scale bar is 50 nm.
- Figure 2.3: Selection from the upper-right corner of Figure 2.3, showing a) binary image showing particles in black and the background in white, and b) particle outlines as computed by ImageJ. The numbers inside the outline correspond to tabulated particle measurements.
- Figure 2.4: Histogram of particle diameters for 1567 nanoparticles measured from the TEM image shown in Figure 2.2. Particles under 4 nm in diameter and over 10 nm in diameter were not counted.
- Figure 2.5: Typical AAS calibration curve. As long as absorbance of a sample lies within the calibrated region its concentration can be known very accurately.
- Figure 2.6: Initial state of nanoparticle crystal preparation. The test tube was photographed with a straight line in the backdrop so that the change in the index of refraction emphasizes the transition between layers.
- Figure 2.7: TEM image of iron oxide nanoparticle crystals.

- Figure 2.8: SAXS profile showing the clear distinction between well-ordered, FCC nanoparticle crystals and disordered assemblies of 8.5 nm iron nanoparticles. (Reproduced from Ref. 6). In this thesis, a similar procedure was used to prepare Fe_3O_4 nanoparticle crystals for neutron small angle scattering (SANS). The angular range for SANS is lower than for SAXS, and only the region of the (111) and (200) peaks is probed.
- Figure 2.9: Zero-field cooled (ZFC) magnetization curve measured under a 200 Oe applied for a 6.7 nm iron oxide nanoparticle crystals.
- Figure 2.10: Magnetization curves for 6.7 nm iron oxide crystals and a dilute suspension of 6.7 nm iron oxide particles frozen in toluene.
- Figure 2.11: Magnetic isotherms showing the measured magnetization of the 6.7 nm nanoparticle crystals and the calculated Langevin function at various temperatures between 10 and 300 K. All magnetization values are normalized to the saturation magnetization at 10 K.
- Figure 2.12: Illustration of the effective field used to map the experimental data onto the Langevin function.
- Figure 2.13: Plot of the calculated effective fields as a function of temperature and applied field including the Lorentz cavity field which represents the maximum physical demagnetizing field.
- Figure 2.14: Distribution of dipolar interaction fields model fit to experimental isotherms for 7 nm iron oxide colloidal crystals at temperatures of 10, 20, 100, 160, 200, and 320 K.
- Figure 2.15: Magnetization curves calculated from the distribution of dipolar interaction fields model. These curves were calculated using the physical properties of 6 nm cobalt nanoparticles. (Reproduced from Ref. 18)
- Figure 2.16: Longitudinal MPMS SQUID flux pickup coils (left), and transverse flux pickup coils (right). (Reproduced from Ref. 19).
- Figure 2.17: Scaled transverse magnetic moment at 100 K plotted with the difference between a) the effective demagnetizing field model discussed in Section 2.3.2 and the experimentally measured longitudinal moment, and b) the distribution of dipolar fields model discussed in Section 2.3.5 and the experimentally measured longitudinal moment.
- Figure 3.1: Schematic of unpolarized neutron scattering experiment. The 2-D detector array is located in the X,Y-plane as illustrated. A magnetic sample saturated along the applied field direction (x-axis) only contains nuclear scattering in the x-direction.

- Figure 3.2: A simplified schematic of an FeSi neutron supermirror cavity showing the preferential reflection of spin up neutrons and the transmission of spin down neutrons. The angle between the incident wave vector and the mirror is shown as α . In reality there would be many more multilayers.
- Figure 3.3: a) Schematic of experimental setup including the supermirror, flipper, sample, applied magnetic field, ^3He cell, and detector from left to right. Notice that as long as the polarization axis varies slowly, spin information is retained. This allows for the use of convenient geometries for the applied magnetic field and the ^3He polarization axis. b) 2D polarization corrected SANS data taken at 1.2 T and 200 K. Notice that θ is measured with respect to the x-axis. (Reproduced from Ref. 34).
- Figure 3.4: Scattering at 50 K in a remanent field of about 25 G. The horizontal and vertical axes represent the pixel number. The image on the left shows NSF scattering dominated by nuclear scattering. The image on the right shows SF scattering is asymmetric due to the M_z scattering along the y-direction, and $M_z + M_y$ scattering along the x-direction. All four cross-sections are not shown due to the similarity between the two NSF patterns and the two SF patterns. (Reproduced from Ref. 17).
- Figure 3.5: Nuclear and magnetic scattering profiles at 50 K and in a remanent field of approximately 25 G. The nuclear scattering exhibits a Bragg peak as expected at 0.083 \AA^{-1} . The magnetic scattering is nearly isotropic, but slightly favors the x-direction because it is the direction of the remanent field. (Reproduced from Ref. 17).
- Figure 3.6: Low-Q magnetic scattering in the x-direction in 25 G remanent field representing decreasing long range order as a function of increasing temperature. The ordering continues to decrease well above the blocking temperature of 60 K. (Reprinted from Ref. 17).
- Figure 3.7: Nuclear, and magnetic scattering parallel and perpendicular to a 1.2 T applied field at 50 K. The nuclear scattering shows the interparticle Bragg peak, and the magnetic scattering is dominated by scattering parallel to the magnetic field. (Reproduced from Ref. 17).
- Figure 3.8: The four, polarization corrected cross sections recorded at 1.2 T and 200 K. (Reproduced from Ref. 34).
- Figure 3.9: a) Nuclear and parallel magnetic scattering profiles at 1.2 T and 200 K. The data were scaled so that the nuclear peak had a value of 1000. Notice the large difference between the magnitude of the parallel scattering (right axis) and the nuclear scattering (left axis). The parallel magnetic scattering

is presented as calculated using Eq. 3.11 and Eq. 3.13 in order to show their equivalence. The blue and purple fit lines are associated with the model given in Figure 3.8 b) The perpendicular magnetic scattering shows a prominent dip at about 0.075 \AA^{-1} . The green line shown is associated with the model given in Figure 3.8. (Reproduced from Ref. 34).

Figure 3.10: Transmission electron microscope (TEM) image showing part of a nanoparticle crystallite made up of FCC packed 9 nm iron oxide nanoparticles.

Figure 3.11: a) N^2 , M^2_{PARL} (black triangles and pink curve), and M^2_{PERP} (green curve) structure factors including instrumental broadening. b) Spherical form factors calculated for several structures showing the strong sensitivity of the dip position to the structure. The structure factors in a) and form factors in b) were convoluted to produce the fits shown in Figure 4.9. c) A composite model is depicted containing a 7.4 nm magnetic core and a coherently perpendicular magnetic shell with a thickness between 0.8 and 1.2 nm. (Reproduced from Ref. 34).

Figure 3.12: a) Temperature dependence of M^2_{PERP} . The temperature was varied in an applied field of 1.2 T and shows the presence of canted magnetic shells at 160, 300, and 320 K, but no ordered shell was found after zero-field cooling to 10 K before the application of a the 1.2 T field. b) At 300 K in a remanent field of 0.005 T, $M^2_{\text{PERP}} = M^2_{\text{PARL}}$ and fits the modeled scattering from a 9.0 nm sphere lacking a distinct shell. (Reproduced from Ref. 34).

Figure 4.1: a) nanocross morphology caused by the presence a very small amount of water and b) micron sized particles caused by the condensation of acetone into the solution.

Figure 4.2: Temperature of the reaction as a function of time. The last 15 minutes of the drying cycle, the fast ramping to 350°C , and the cooling can be seen clearly.

Figure 4.3: Reaction vessel at a) about 200°C after precursor had dissolved completely, b) beginning to turn clear yellow, c) turning brownish-yellow, d) turning to a white milky-green, e) turning to a deeper milky green, f) synthesis is complete with a deep milky-green. The total time shown in the figure is about 3 minutes.

Figure 4.4: Photographs of manganese oxide nanoparticle suspensions showing a) the green color of MnO and b) the brown color of Mn_3O_4 .

Figure 4.5: a) particles oxidized at room temperature, and by bubbling air into particles suspended in trioctylamine at 100°C for b) 3 hours and c) 80 hours.

Figure 4.6: High resolution TEM image of MnO|Mn₃O₄ nanoparticle showing contrast variation between the core and shell due to Bragg orientation, and a lattice spacing variation between the core and shell. The parallel orientation of the lattice fringes for the core and the shell are evidence of the epitaxial registry. (Courtesy of Yoosuf Picard).

Figure 4.7: Hysteresis loops of unoxidized MnO particles and oxidized MnO|Mn₃O₄ particles of varying oxidation times and shell thicknesses recorded after field cooling in a 55 kOe field from 250 K to 10 K. Inset shows detail at the zero crossing.

Figure 4.8: Coercive and exchange fields as a function of oxidation time for MnO nanoparticles. Notice the large discrepancy between particles that were and were not annealed. Error in the measured field is on the order of 50 Oe, error in the oxidation time is on the order of 0.25 hours.

Figure 4.9: TEM image of particles oxidized at 300 °C for 6 hours. Notice the shell thickness of 2-3 nm is comparable to the sample shown in Figure 4.6b, but the Bragg contrast in the core is much less uniform indicating poorer crystallinity.

Figure 4.10: Remanent (blue) and standard hysteresis loop (green) for unannealed MnO|Mn₃O₄ particles in which the shell was formed by oxidizing the particles in solution for 6 hours at 300 °C.

Figure 4.11: HR-SEM micrographs showing colloidal crystals of MnO nanoparticles. The images show a) the large size and faceting of the crystallites, and b) the high degree of long range order.

Figure A1.1: Empty drinking straw attached to sample rod.

Figure A1.2: Left to right, disassembly and nesting of gelatin capsule.

Figure A1.3: Assembled sample prepared with gelatin capsules. Notice that the nested capsules containing the sample open to the right. Underneath, opening to the left is an empty set of nested capsules to increase the symmetry of the diamagnetic contribution from the gelatin capsules. Above and below the capsules folded pieces of drinking were inserted into the main straw to support sample. Please take note of the approximate position of the sample inside the straw.

Figure A1.4: Glass ampoule with liquid sample taped inside drinking straw.

Figure A1.5: Wafer taped to straw for in-plane measurement.

Figure A1.6: Example of a small piece of straw with a sample taped to it supported inside main straw with folded pieces of straw. Use this arrangement or similar technique for out of plane measurements.

Figure A2.1: Diagrams of the a) $R_l=0.97$ cm radius, longitudinal pickup coils and b) the $R_t=0.8$ cm radius transverse pickup coils for the MPMS SQUID magnetometer. $L=0.97$ cm, $d=0.0508$ cm, and $a=1.529$ cm.¹ (Reproduced from Ref. 2 and modified).

Figure A2.2: Illustration of the magnetic flux sign convention. In the context of the SQUID detection coils, the arrow indicates the chirality of a given loop.

Figure A2.3: Ideal longitudinal SQUID response voltage, $V_l(z)$, to a centered, longitudinal, point dipole. Note that the center of the pickup coils is taken to be $z=2$ cm. (Reproduced from Ref. 2)

Figure A2.4: Ideal transverse SQUID response voltage, $V_t(z)$, to a centered, transverse, point dipole. Note that the center of the pickup coils is taken to be $z=2$ cm. (Reproduced from Ref. 2).

Figure A2.5: A transverse moment oriented in the y-direction does not generate a signal. A transverse moment oriented in the x-direction, towards the center of the pickup coils generates the maximum signal. (Reproduced from Ref. 2).

Figure A2.6: Diagram of flux generated by a perfectly centered longitudinal point dipole. The angle between the area vector, dA , and the enclosed magnetic field, B , defines the sign of the magnetic flux, Φ . Their product defines the magnitude.

Figure A2.7: Diagram of flux generated by an off-center, longitudinal point dipole. The angle between the area vector, dA , and the enclosed magnetic field, B , defines the sign of the magnetic flux, Φ . Their product defines the magnitude.

Figure A2.8: Transverse SQUID response to an off-center longitudinal moment from a measurement of a nickel sphere. The response is the combination of small, functionally even contribution from a transverse component, and a functionally odd contribution from the off center longitudinal component. (Reproduced from Ref 2).

Figure A2.9: Schematic of the transverse pickup coil response to a transverse moment. The sign is the same for the flux through each coil.

Chapter 1

Introduction to Relevant Magnetism

1.1 INTRODUCTION

Human beings have known about the existence of magnetism for at least 2500 years beginning with observations that naturally magnetized pieces of Magnetite (Fe_3O_4) called lodestones, attracted pieces of iron and other lodestones. Interestingly, there is evidence that such geometrically diverse ancient societies as the Olmec tribe in the Americas,¹ the Han Chinese,¹ and the Greeks were all familiar with the magnetic behavior of Fe_3O_4 . Under the long lens of history, it didn't take very long for these ancient cultures to discover that needle-shaped pieces of lodestone, or iron that had been rubbed with lodestone would point consistently in the same direction when arranged so that they could float and rotate freely on water to align with the earth's magnetic field. These early magnetic compasses were a profound application of the mysterious force and showed at least an empirical understanding of the ability of shape anisotropy to favor certain magnetization directions.

The development of a formal mathematical understanding of magnetism began much later in the mid-19th century with the work of Oersted, Faraday, and Maxwell, and was supplemented in the early 20th century by a growing understanding of the force's quantum mechanical origins. Today we see magnets and the application of magnetic principles almost everywhere. Amazingly, even after humans have carried around bits of Fe_3O_4 for millennia, aspects of its behavior are still mysterious and surprising when first encountered.

The simplest system for understanding the fundamental physics of magnetic interactions is the single magnetic domain, which is commonly found in a nano-size particle. Chapter 2 will discuss direct measurements and models of the interactions between Fe_3O_4 nanoparticles and how these help advance our basic understanding and predictive modeling of such systems. Chapter 3 will discuss the structure of magnetic moments inside single Fe_3O_4 nanoparticles and the development of the polarization analyzed small angle neutron scattering (PASANS) technique that was used to probe the intraparticle magnetic structure. In Chapter 4, we examine exchange bias interactions in $\text{MnO}/\text{Mn}_3\text{O}_4$ core/shell manganese oxide particles. Unlike more commonly studied exchange bias core/shell particles like Co/CoO or Fe/FeO, the $\text{MnO}/\text{Mn}_3\text{O}_4$ system has epitaxial interfaces,² and is therefore a preferred nanoparticle system for the rigorous study of exchange bias. We will discuss situations in which we believe exchange bias-

like properties have been misinterpreted in exchange biased nanoparticle structures and present supporting evidence.

Chapter 1 will introduce the terminology and physics relevant to support the understanding of the chapters that follow. Diamagnetism, paramagnetism, ferromagnetism, ferrimagnetism, and antiferromagnetism will be discussed along with the associated physics, including the exchange interaction, magnetocrystalline anisotropy, and magnetostatic interactions will be discussed. All concepts and terms will be discussed in the context of bulk and nanoparticle systems. Finally, building upon this context, a simplified, intuitive explanation of exchange bias will be given. The two focus areas of this thesis are magnetostatic interactions *among* nanoparticles in an assembly, and interactions *within* a single nanoparticle due to chemical differences (core/shell particles) and symmetry breaking at the surface (surface anisotropy).

1.2 DIAMAGNETISM

Electrons have a magnetic moment due to their spin and orbital angular momenta. This can be thought of in terms of the simplest model of the atom, the Bohr model, where an electron orbits the nucleus of an atom in a circular path. The circular motion of the electron around the nucleus is analogous to a current of electrons flowing through a circular loop of wire. We know the latter to as an electromagnet. As Fermions, electrons fill the orbitals around an atomic nucleus in pairs with opposing spins of +1/2 or -1/2, each canceling the moment of the other. If the moments of all electrons in an atom are cancelled in this way, the material is said to be diamagnetic. In reality this picture is far more complex, and the magnetic moment is due to a combination of spin and orbital angular momentum. Diamagnetism is not relevant to this chapter as the cases of interest to us depend on a net magnetic moment coming from atomic orbitals that are not completely filled.

1.3 PARAMAGNETISM

In the simplest case, the moments from unfilled orbitals behave paramagnetically. Absent an applied magnetic field a paramagnetic (PM) material, composed of many paramagnetic atoms has no net magnetic moment because of thermal fluctuations in the orientations of individual spins. An applied magnetic field competes with the randomizing thermal energy and partially aligns paramagnetic moments in the direction of the applied field such that the magnetization, M , follows the Curie Law, $M = \chi H$, where χ is the magnetic susceptibility and H is the applied magnetic field. For small applied fields the susceptibility is linear and in paramagnets it is always positive.

A more comprehensive understanding of paramagnetism was developed by Langevin who derived the response of a magnetic moment, μ , to an applied field, H , at a given temperature, T , by integrating the magnetic energy, E , distributed according to the Boltzmann factor, $e^{-E/kT}$, through a hemisphere of possible orientations. The result is referred to as the Langevin function:

$$L(H, T) = \coth\left(\frac{\mu H}{kT}\right) - \left(\frac{kT}{\mu H}\right), \quad (1.1)$$

where k is Boltzmann's constant.

1.4 FERROMAGNETISM, ANTIFERROMAGNETISM, and FERRIMAGNETISM

Unlike paramagnetic and diamagnetic materials, once magnetized, ferromagnetic materials retain long-range order in the absence of an applied magnetic field. This order is the result of the quantum mechanical exchange interaction, which unlike many magnetic phenomena, is without a classical analog.

The exchange interaction is most simply explained by considering the interactions between two hydrogen atoms in close proximity. Each hydrogen atom has one electron and one proton. The protons and electrons both repel their like counterparts through the Coulombic repulsion. Similarly, the electrons and protons are attracted to each other. If the hydrogen atoms become close enough that the quantum mechanical wavefunctions of the electrons overlap (*i.e.* the electrons can be “exchanged”), it becomes necessary to consider the energy levels of the combined system instead of treating the two atoms separately. In the combined system, according to the Pauli Exclusion Principle the electrons must have opposite spin. The attractive minimum energy state associated with anti-parallel electron spins competes with the minimum energy state associated with the Coulombic repulsion. In the end, the favored spin alignment depends on the distance between the two atoms and defines the exchange constant, J_{ex} , which is part of the exchange energy, $E_{ex} = -2J_{ex} S_i S_j$, where S_i and S_j are the spin-angular momenta of the two atoms. When J_{ex} is positive, parallel alignment of the electrons is favored and a material is ferromagnetic. Likewise, when J_{ex} is negative, anti-parallel arrangement of the electrons is favored and a material is antiferromagnetic. The relationship between atomic spacing and electron separation was distilled into the Bethe-Slater curve which postulates a relationship between exchange constant and the ratio of the atomic radius to the radius of the 3d electron shell.³ Although the details of this relationship between atomic spacing and magnetism are not yet rigorously understood it is clear that it has a great deal to do with how materials behave magnetically.

Antiferromagnetism (AFM) exists when the exchange constant is negative and causes the uncompensated electrons of adjacent atoms to align anti-parallel. In these structures, one refers to sublattices of the total crystal structure inside which electron spins are parallel, and between which electron spins are anti-parallel. This is illustrated schematically in Figure 1.1b.

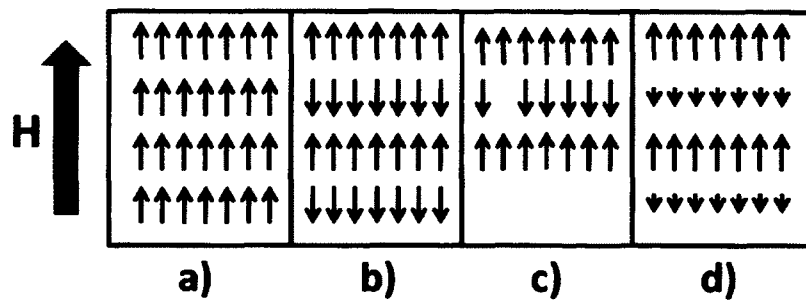


Figure 1.1: Schematic diagram of the spin arrangement relative to the applied field in a) a ferromagnet, b) a perfectly compensated antiferromagnet, c) an antiferromagnet showing uncompensated spins due to a missing sublattice and a vacancy, and d) a ferrimagnet.

The sublattice structures come in a wide variety. Just as we talk about filled electron shells being compensated (having no net moment) and unfilled shells being uncompensated (having a net magnetic moment), we talk of these magnetic sub lattices being compensated such that the material has no net magnetic moment, as in Figure 1.1b, or uncompensated so that the material has a net magnetic moment as shown in Figure 1.1c. Realistically, it is impossible to construct a perfectly compensated antiferromagnet, and there is always a very small, but finite moment. A lack of perfect compensation is common at surfaces, or the interface between two materials and is the basis for exchange bias, a phenomenon we will discuss shortly. The AFM structure was first proposed by Neél in 1948⁴ and confirmed by Shull and Smart in 1949.⁵ Coincidentally, this confirmation of Neél's structure was made using neutron diffraction to probe the magnetic structure of MnO, incorporating both a material and a technique that will be discussed at length in the following chapters.

Ferrimagnetism (FiM) occurs in materials having spin arrangements that are very similar to antiferromagnets in that the exchange energy favors neighboring spins to be aligned antiparallel. The difference comes from the fact that in a FiM the different sublattices have different moments, as shown in Figure 1.1d. Thus, even in a material with two sublattices that are perfectly compensated, in the sense that each spin has an oppositely oriented neighbor, there is a net moment because the magnitude of the moment from the spins on the different sublattices is different. Because of this ferrimagnets have a net moment and in that sense behave very much like ferromagnets. Both Fe₃O₄ and Mn₃O₄ are studied in the following chapters. The asymmetry between their sublattices comes from the different magnetic contributions of the Fe²⁺ and Fe³⁺, or Mn²⁺ and Mn³⁺ valences.

While the exchange energy favors certain spin arrangements in ferromagnets, antiferromagnets, and ferrimagnets there is also a competition between the order favoring magnetic interactions which depend on the applied magnetic field and disordering thermal interactions which depend on temperature. At a certain critical temperature for all magnetic materials the thermal disorder overcomes magnetic order. In ferromagnets and ferrimagnets, this temperature is called the Curie temperature, T_C . The Curie temperatures of the ferrimagnets studied in here are 858 K and 42 K, for Fe₃O₄ and

Mn_3O_4 , respectively.⁶ In antiferromagnets, it is called the Ne  l temperature, T_N . The Ne  l temperature of MnO is 122 K.⁷

In ferromagnets and ferrimagnets, when the magnetization is measured as a function of applied magnetic field we define the saturation magnetization, M_S , as the magnetic moment normalized by mass or volume when all spins are completely aligned. In the strictest sense, to remove thermal fluctuations, M_S should be measured at absolute zero, but it is a useful metric at all temperatures. The remaining magnetic moment after the application and subsequent removal of a field is referred to as the remanent magnetization, M_R , and the magnitude of the field opposing the magnetization of a material required to reduce the magnetization to zero is called the coercive field, H_C . Although easily measured, the remanent magnetization is not an inherent material property and depends on the distribution of crystallographic orientation in a sample. The coercivity is defined as the width of the hysteresis loop or twice the coercive field. All of these terms are most useful when visualized in the context of a hysteresis loop which is the measured magnetization of a material as a function of the applied magnetic field as shown in Figure 1.2.

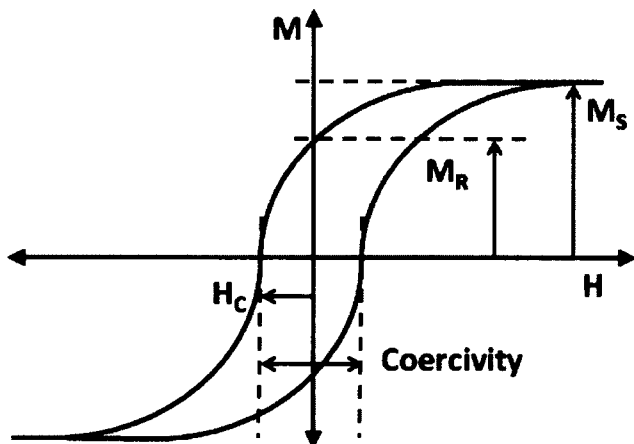


Figure 1.2: Schematic hysteresis loop illustrating the saturation magnetization, M_S , the remanent magnetization, M_R , the coercive field, H_C , and the coercivity which is equal to $2H_C$.

Different magnetic materials approach saturation in an applied magnetic field differently. Generally, “hard” magnetic materials are slow to approach saturation and only saturate at large applied fields. Hard materials also tend to have a large remanent magnetization and a large coercive field. They are useful for data storage or for permanent magnet materials where it is important that once set the magnetization is maintained. Conversely, “soft” magnetic materials approach saturation quickly and saturate at relatively low fields. They also tend to have lower remanent magnetization and coercive field values and are used when it is important to switch the magnetization quickly with minimal energy loss, as in inductors and transformer cores. The area enclosed by a hysteresis loop corresponds to the energy lost in one cycle of the magnetization from positive saturation to negative saturation and back. Magnetic

hardness or softness in the approach to saturation is governed by a material's inherent magnetocrystalline anisotropy, K .

In crystalline, bulk materials, magnetocrystalline anisotropy depends on the relative orientation of the applied magnetic field to certain crystallographic axes. Along one axis a material may be very soft and saturate quickly while along another axis it is very hard to saturate. In this case, the soft axis is referred to as the magnetic easy-axis. Very symmetric structures, like cubic materials, tend to have relatively low anisotropy values and don't dramatically favor the magnetization along one axis over another. Structures with low symmetry, such as hexagonal or tetragonal materials, tend to have high values of anisotropy and show a strong preference a certain easy-axis.

1.5 MAGNETISM IN THE CONTEXT OF NANOPARTICLES

In the context of magnetic nanoparticles, it is useful to define some additional terms. Nanoparticles warrant being treated separately for several reasons. First, they are small enough that they are monodomain. In large pieces of magnetic material, energy minimization causes the formation of magnetic domains that arrange such that they minimize the stray flux. Within a domain, the direction of the individual magnetic spins is coherent. How small a particle needs to be to be monodomain is traditionally given by the relationship,

$$d_{cr} = \pi S \sqrt{\frac{J}{K \cdot a}} \quad (1.2)$$

Where d_{cr} is the size under which a particle is monodomain, S , is the magnetic moment per atom, J , is the exchange constant, K , is the uniaxial anisotropy, and a is the lattice constant.⁸ I emphasize that this is the traditional limit, because the polarization analyzed small angle neutron scattering (PASANS) results presented in Chapter 2 show conclusive evidence of non-uniform intraparticle magnetic structure in 9 nm iron oxide particles. For the simplicity of this introduction, we will consider iron oxide nanoparticles under 10 nm to be monodomain and therefore, all of the spins in the particle to behave coherently as a single magnetic moment per particle. The coercivity of monodomain particles eventually decreases to zero, below which the particles are considered to be superparamagnetic.⁹

Because of the relationship between thermal fluctuations in the orientation of the particle moments and the time it takes to measure them, characterizing the temperature at which a collection of particles become superparamagnetic is not straightforward. To understand this we consider the balance between destabilizing thermal energy given by kT , and stabilizing anisotropy energy given by KV , where V is the volume of the particle. For thermal energy to flip a particle moment it must overcome the energy barrier given by KV . It attempts to do this at approximately the Larmor precession frequency of $\tau_0 \sim 10^9$ s⁻¹ and the time for the moment to equilibrate at a given temperature is given by the Arrhenius Law as,

$$\tau = \tau_0 e^{KV/kT}. \quad (1.3)$$

If τ is less than the time it takes to measure a system in a given state, then the no hysteresis—or coercivity—will be observed and the particles will be superparamagnetic. If τ is longer than the measurement time, τ_m , then equilibrium is never reached during a measurement at low temperatures. When this is the case particles only become superparamagnetic above a certain temperature at which the time to reach equilibrium the same as the measurement time. This temperature is called the Blocking temperature and is given by,

$$T_B = K V \ln \left(\frac{\tau_m}{\tau_0} \right). \quad (1.4)$$

The Blocking temperature is typically measured by preparing a collection of particles in a magnetically disordered state by cooling it in zero-field (ZFC) to a low temperature, and then measuring the magnetization at a very low field while warming.⁹ In a superconducting quantum interference device (SQUID) magnetometer typically used for these measurements, the time to measure a single state is on the order of 100 s. The SQUID sensor, at the heart of the magnetometer, uses Josephson junctions and the wave nature of electrons to measure extremely small currents induced by the Faraday effect in the magnetometer's pickup coils. When τ_m is comparable to the equilibration time of the particle moments, a peak is observed in the ZFC magnetization as a function of temperature. The peak is analogous to a movie scene where the wheel of a moving car appears to be motionless because it rotates exactly once for each frame of film. At the peak temperature of a ZFC curve the moments have the optimum time to fully align. Above this temperature, T_B , the measured magnetization begins to decrease due to disordering thermal fluctuations. The measurement of T_B and the relationship given in Eq. 4.4 is often used to experimentally measure the anisotropy in nanoparticle systems.

The term superparamagnetic can be somewhat confusing because it refers to particles that are still ferro- or ferrimagnetic, and therefore certainly not paramagnetic. However, in the dilute, non-interacting limit the average spin of a single particle behaves like an individual spin in a paramagnet. Because non-interacting superparamagnetic particles behave like a paramagnet, their behavior can be fit to the Langevin function given by Eq. 1.1. I have carefully emphasized that superparamagnetic particles only fit the Langevin function in the non-interacting limit because there is an interesting region above the Blocking temperature where the measured magnetization curves do not match Langevin behavior due to interparticle interactions. This is referred to as the superferromagnetic region. The term implies cooperative interactions between nanoparticles that if isolated would behave individually as superparamagnets. An explanation of methods to explore the nature of how these interactions manifest themselves as deviations from the ideal Langevin behavior is the topic of Chapter 2.

1.6 MAGNETIC NANOPARTICLE INTERACTIONS

Interactions between magnetic nanoparticles primarily include exchange interactions and magnetostatic dipolar interactions. It is possible to have weak exchange interactions between the outer atoms of nearest neighbor particles if they are in direct contact with one another. However, in all systems that will be discussed in the following chapters, our particles are separated from their nearest neighbors by 2-3 nm of surfactants composed of either oleic acid or a combination of oleic acid and olyelyamine. Because exchange interactions require the overlap of the electronic wave functions and our particle separation is too great to allow for exchange interactions we will not discuss it any further than we did earlier in this chapter.

Magnetostatic fields caused by the dipole-dipole interaction between two particles are of sufficiently long range to be significant in our systems. If spherical particles are treated as point dipoles, the dipolar field created by a magnetized particle with moment μ at a point separated from the center of the particle by a distance r is given by,

$$\mathbf{H}(\mathbf{r}) = -\frac{1}{4\pi r^3} \left[\mu - \frac{3}{r^3} (\mu \cdot \mathbf{r}) \mathbf{r} \right] \quad (1.5)$$

where vectors are denoted by bold text.¹⁰ Using this relationship at a center-to-center distance of 9 nm, which assumes 7 nm diameter particles with 2 nm of surfactant between them, the field would be about 10 Oe and is not negligible.

A useful upper limit on interaction fields generated by an assembly of nanoparticles is the Lorentz cavity field. The Lorentz cavity field is the field generated by a spherical void in a uniformly magnetized material. It is opposite in sign to the magnetization in the material as shown in Figure 1.3.

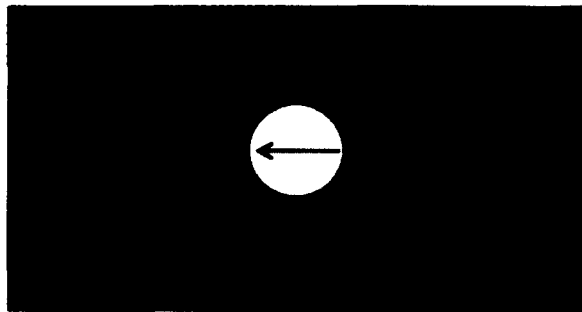


Figure 1.3: Schematic of the Lorentz cavity field generated by a spherical hole in a uniformly magnetized material.

The Lorentz cavity field at the center of a spherical void has a magnitude of $(4\pi/3) M_s$. Our iron oxide nanoparticles have a saturation value of 85 emu/g or 442 emu/cc assuming the bulk density for Fe_3O_4 of 5.2 g/cc. Therefore, the maximum Lorentz cavity field would be about 1850 Oe. If the saturation magnetization in the calculation was scaled to account for the close packing of our nanoparticles and the 2 nm surfactant shell this value would be less than 1000 Oe.

1.7 EXCHANGE BIAS

Finally, as discussed in the previous section, exchange interactions are nonexistent between magnetic nanoparticles with a surfactant coating. At an interface between two materials, however, exchange interactions are very prominent. Exchange bias can be thought of as an interfacial anisotropy caused by the exchange interaction between uncompensated antiferromagnetic spins, and ferromagnetic or ferrimagnetic spins at an AFM/FM or AFM/FiM interface. This can be understood by examining the spin orientations at several points in a hysteresis loop for an exchange biased material as shown in Figure 1.4.

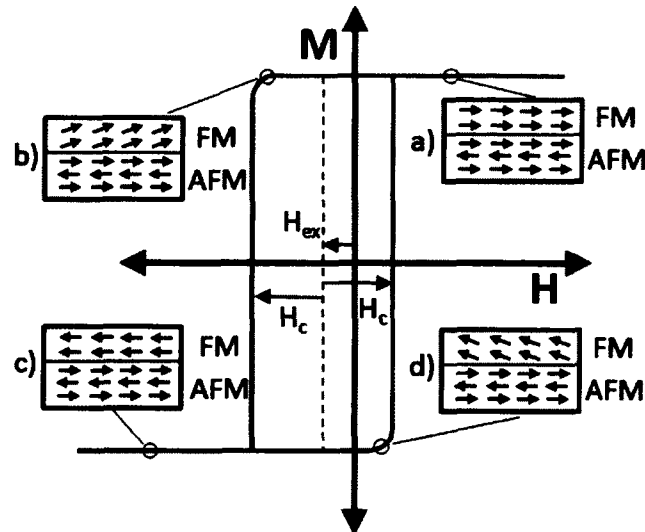


Figure 1.4: Intuitive picture of exchange bias material in the context of a hysteresis loop.

The state in position a) is accessed by cooling the material through both the Curie temperature (T_C) and the Neél temperature (T_N) under a large (typically > 50 kOe) applied field. The Curie temperature and Neél temperature are the temperatures below which the materials transform from paramagnetic to ferromagnetic or antiferromagnetic, respectively. For the intuitive model it is simplest to ignore whether $T_N > T_C$ or not. In this saturated state, all FM spins are aligned parallel to the applied field and the AFM spins are aligned either parallel or antiparallel to the interface. In the ideal case all AFM spins would be compensated, meaning each spin parallel to the field would be compensated by a spin antiparallel to the field. In reality, because of surface and interfacial effects AFM spins are never perfectly compensated. Here, the uncompensated AFM spins at the interface are aligned with the FM spins at the interface as is favored by the exchange interaction. At position b), the FM spins are beginning to flip in the direction favored by the applied field direction, but because the interfacial spins prefer to be parallel because of the exchange interaction this happens at a higher negative applied

field than in a non-exchange biased system. In the presence of a saturating negative applied field shown at position c) all of the FM spins are aligned in the field direction and the interfacial spins oppose each other. Note that the arrangement of the AFM spins in this case is for an AFM material with large intrinsic anisotropy (K_{AFM}). This case is simplest for the intuitive understanding of the system. Finally, position d) shows that the FM spins return to saturation in the positive direction at a much lower field than in the negative direction because the exchange interaction strongly favors aligned FM and AFM spins at the interface.

1.8 REFERENCES

-
- ¹ J. B. Carlson, *Science* 189, (1975), 753-760.
 - ² A. E. Berkowitz, G. F. Rodriguez, J. I. Hong, K. An, T. Hyeon, N. Agarwal, D. J. Smith, and E. E. Fullerton, *J. Phys. D: Appl. Phys.* 41 (2008), 134007.
 - ³ B. D. Cullity, C. D. Graham, "Introduction to Magnetic Materials," John Wiley & Sons: New Jersey, 2009.
 - ⁴ L. Neél, *Annales de Physique* 3 (1948), 137.
 - ⁵ C. G. Shull, and J. S. Smart, *Phys. Rev.* 76 (1949), 1256.
 - ⁶ K. Dwight, and N. Menyuk, *Phys. Rev.* 119 (1960), 1470.
 - ⁷ C. G. Shull, and J. S. Smart, *Phys. Rev.* 76 (1949), 1256.
 - ⁸ F. E. Luborsky, *J. Appl. Phys.* 32 (1961), 171S.
 - ⁹ S. A. Majetich, J. H. Scott, E. M. Kirkpatrick, K. Chowdary, K. Gallagher, and M. E. McHenry, *Nanostruct. Mat.* 9 (1997), 291-300.
 - ¹⁰ J. D. Jackson, "Classical Electrodynamics: Third Edition," Hamilton Publishing Co., 1999.

Chapter 2

Fe₃O₄ Nanoparticle Interactions

2.1 INTRODUCTION

As discussed in the introduction, monodomain magnetic nanoparticle behavior can be characterized using temperature and field dependent measurements of the magnetization. Arrehnius-like relaxation models balancing both anisotropy energy and thermal energy can accurately describe the onset of superparamagnetism. At temperatures above the onset of superparamagnetism, the behavior of ideal, non-interacting particles is well described by a Langevin function. Interacting particles, however, exhibit deviations from the ideal behavior in a region between the blocking temperature and the onset of true superparamagnetism. Here we are interested in investigating the nature of the particle interactions that cause deviations from the truly decoupled Langevin-like behavior in this superferromagnetic region.

2.2 IRON OXIDE PARTICLE SYNTHESIS and CHARACTERIZATION

Iron oxide nanoparticles were synthesized using the high temperature decomposition of iron acetylacetone in the presence of 1,2-hexadecanediol, oleic acid, and oleylamine as described by Sun *et al.*¹ These nanoparticles are monodispersed and 6.7 ± 1.0 nm in size where the margin given is plus or minus one standard deviation for a sample size of 1567 particles.

2.2.1 PARTICLE SIZE CHARACTERIZATION

The particle size distribution was carefully measured after checking the calibration of the TEM. Crystals of bovine liver catalase are suitable for use as a calibration standard in this size range because they have lattice spacings of 8.75 and 6.85 nm that can be reproducibly measured within 2.5%.² The catalase crystals are stained using a heavy metal (high-Z) salt to obtain greater electron contrast from the enzyme. A

TEM image taken at 30,000x magnification was used for the microscope calibration and is shown in Figure 2.1.

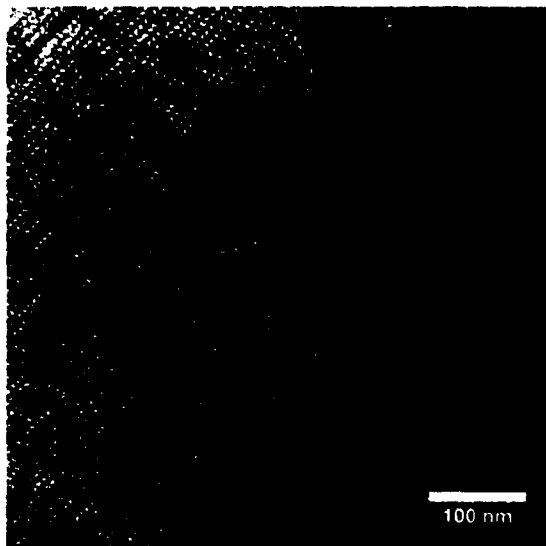


Figure 2.1: TEM image of a stained bovine liver catalase crystal recorded at 30,000x magnification. The lattice spacing is 8.75 nm parallel to the red line, and 6.85 nm perpendicular to it.

The calibration factor used to convert pixels on the CCD detector to nanometers was measured to be 4.81 pixels/nm. If this procedure was not performed and the existing calibration of 4.44 pixels/nm was used, particles would appear to be about 7% larger.

Following the calibration of the CCD scaling, the particles were imaged, then the size distribution was calculated using the ImageJ software package.³ The TEM image used to calculate the size distribution is shown in Figure 2.2 and is representative of the sample.

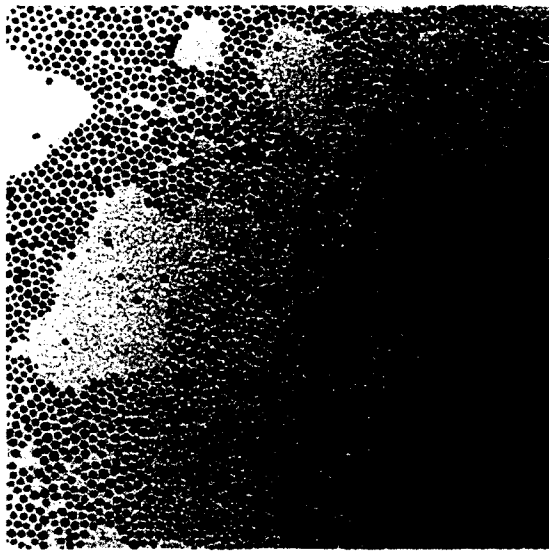


Figure 2.2: TEM image of iron oxide nanoparticles recorded at 30,000x magnification and used to measure the particle size distribution. The scale bar is 50 nm.

Using ImageJ, the raw TEM image was thresholded to create a binary image in which the particles are black and the background is white as shown in Figure 2.3a. The software can then identify and calculate the area of each particle. Figure 2.3b shows the computed outlines for a selection of particles. In order to avoid artifacts, particles under 4 nm in diameter, over 10 nm in diameter, and on the border of the image were not counted.

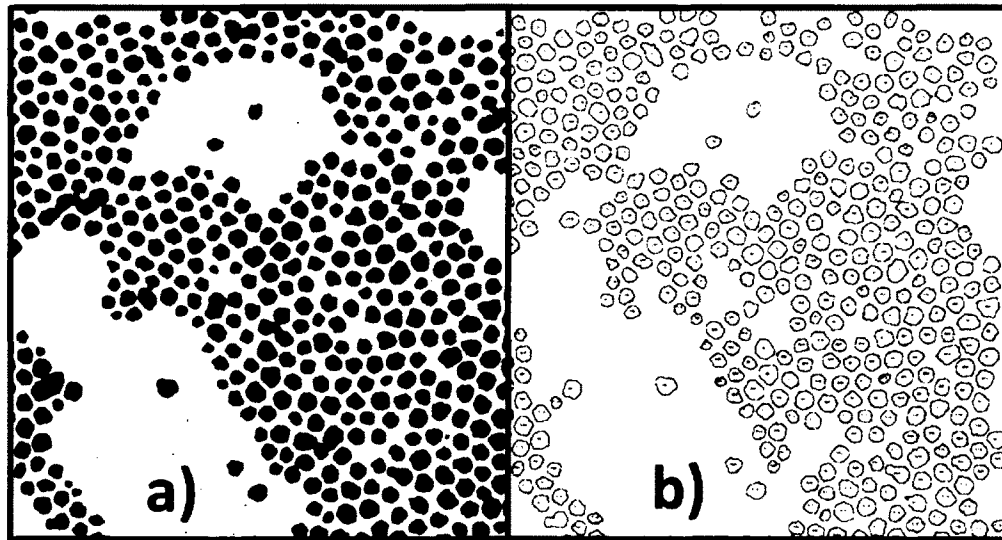


Figure 2.3: Selection from the upper-right corner of Figure 2.3, showing
a) binary image showing particles in black and the background in white,

and b) particle outlines as computed by ImageJ. The numbers inside the outline correspond to tabulated particle measurements.

The particle diameters were plotted in a histogram as shown in Figure 2.4 to verify that the imposed upper and lower bounds did not artificially skew the distribution. Upon close examination it seems limiting the counted particles to those over 4 nm in size was slightly overzealous, but likely had little effect on the mean diameter.

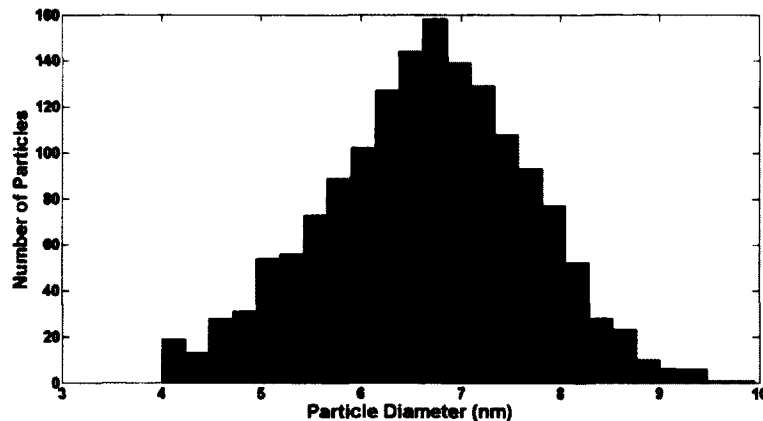


Figure 2.4: Histogram of particle diameters for 1567 nanoparticles measured from the TEM image shown in Figure 2.2. Particles under 4 nm in diameter and over 10 nm in diameter were not counted.

2.2.2 MAGNETIC CHARACTERIZATION

The saturation magnetization, M_s , was measured to be 85 emu/g at 300 K. The error in the moment measured by the SQUID magnetometer is negligible, but because the saturation magnetization is normalized by the mass of the magnetic material in a sample, it is critical that the mass be measured carefully. Simply weighing a sample is not sufficient. If a sample is weighed without accounting for the mass of the surfactant coating there will be significant error.

In this case we measured the mass indirectly, but with high accuracy. To begin, a known volume of the stock nanoparticle solution was dried and digested completely in a known volume of 70% nitric acid. The concentration of iron atoms in the liquid sample is then measured using a technique called atomic absorption spectroscopy (AAS).

In an AAS measurement, the solution of iron atoms is ionized in a flame through which the iron spectrum from a hollow cathode lamp was passed and its absorption by the iron ions in the sample is measured. The absorption is linear with the concentration of iron ions and is calibrated using a series of standards with known iron concentrations. Typically this concentration is in the range of 1 – 1000 ppm (equivalently $\mu\text{g/mL}$) iron. A typical calibration curve is shown in Figure 2.5.

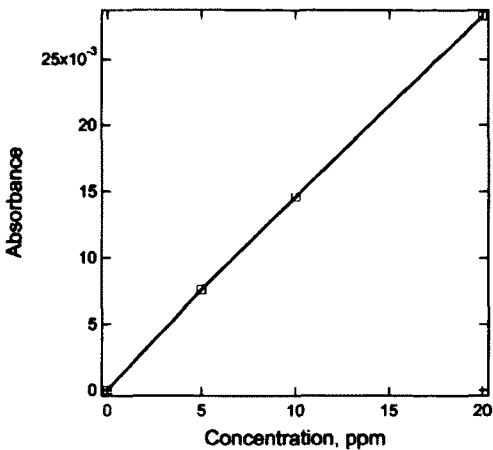


Figure 2.5: Typical AAS calibration curve. As long as absorbance of a sample lies within the calibrated region its concentration can be known very accurately.

Knowing the concentration of iron in the AAS sample—and by extension the concentration of iron in the stock nanoparticle solution—the weight of iron oxide in a known volume of nanoparticles can be calculated assuming the Fe_3O_4 stoichiometry as shown in Eq. 2.1,

$$C_{AAS} \left[\frac{\mu\text{g}}{\text{mL}} \right] * V[\text{mL}] * \alpha * \frac{M_{\text{Fe}_3\text{O}_4}}{M_{\text{Fe}_3}} \left[\frac{\text{g/mol}}{\text{g/mol}} \right] = m_{\text{sample}} [\mu\text{g}] \quad (2.1)$$

where C_{AAS} is the measured concentration of the AAS sample, V is the volume of the nanoparticle solution used to make the magnetometry sample, and α adjusts for any dilutions made in the sample preparation so the concentration is in the optimized range for AAS. Finally, the ratio of molecular weights in the next term, with $M_{\text{Fe}_3\text{O}_4}=231.55$ g/mol and $M_{\text{Fe}_3}=167.55$ g/mol, adjusts from the measured iron concentration to Fe_3O_4 concentration. Using the bulk magnetite density of 5.2 g/cc and the average particle size from the TEM measurement, the sample mass can be converted to the total volume or number of particles.

A SQUID sample is prepared by drying sample volume, V , in a 5 mm gelatin capsule. Gelatin capsules are convenient because they have low background susceptibility and fit conveniently into plastic straws used to mount the sample inside the SQUID. The procedure for the ideal preparation of SQUID samples can be found Appendix I. Once the saturation magnetization of a stock solution of nanoparticles is calibrated, it can be used as a reference for subsequent samples.

2.2.3 PREPARATION OF NANOPARTICLE CRYSTALS

Because we are concerned with the nature of interparticle interactions, it is advantageous to have a sample with well known interparticle spacing. We created close-packed nanoparticle crystals by a slow, controlled destabilization of the nanoparticles in

solution. If nanoparticles are destabilized slowly, they cluster and stick to each other in the lowest energy position. Crystallites formed in this way pack with coherent long range order over about 100 particle diameters. Following previous work,^{4,5} we diluted our stock solution of particles in toluene by about a factor of 10:1 and filled the bottom 6 cm of a 1 cm diameter test tube. A layer of 2-propanol about 2 cm thick was carefully placed on top of the nanoparticle solution and due to its strong polarity and lower density floated on top of the toluene. Finally, a 6 cm layer of ethanol was carefully placed on top of the 2-propanol. The prepared test tube in its initial state is shown in Figure 2.6. Over a period of weeks the ethanol diffused through the 2-propanol barrier and slowly destabilized the nanoparticles.



Figure 2.6: Initial state of nanoparticle crystal preparation. The test tube was photographed with a straight line in the backdrop so that the change in the index of refraction emphasizes the transition between layers.

The nanoparticles are stable in non-polar solutions because their hydrophobic surfactant coating extends for 2-3 nm from the surface of the particle increasing their hydrodynamic volume. Because the density of the surfactant is significantly less than that of the iron oxide, but accounts for a significant portion of the hydrodynamic volume, particles with a surfactant coating are much more buoyant. The introduction of even a small amount of polar solvent causes the surfactant coating to retract, reducing the buoyancy and destabilizing the solution. Slow destabilization is critical in achieving long range order in the nanoparticle crystals. If particles are destabilized too quickly, they don't have time to find their minimum energy position after landing and are pinned in glassy order by the particles landing after them.

A representative TEM image of the nanoparticle crystals is shown in Figure 2.7. These crystals are notoriously difficult to characterize as scanning electron microscopy (SEM) just shows the surface order, and TEM is only useful in regions less than five particle layers thick.

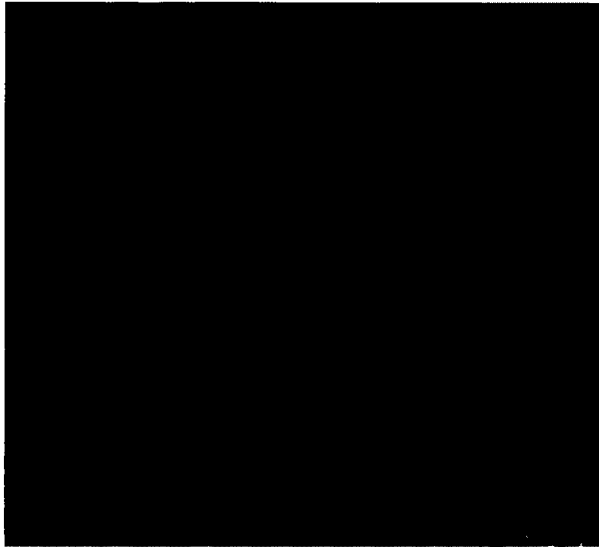


Figure 2.7: TEM image of iron oxide nanoparticle crystals.

For this reason, it is also useful to characterize nanoparticle crystals using small-angle scattering techniques that are sensitive to their ordering length scale. Figure 2.8 shows a small-angle x-ray scattering (SAXS) profile for nanoparticle crystals of 8.5 nm iron nanoparticles that is representative of the technique.⁶ Notice the dramatic difference between the ordered and disordered assemblies illustrating the clarity with which scattering data can confirm the existence of long range structural order in nanoparticle crystals. We were recently confronted with the importance of using scattering to verify long range order when SEM results showed beautiful ordering that was not confirmed by SAXS in an unrelated experiment. We believe this disparity was due to a lack of registry between consecutive layers of well ordered particles.

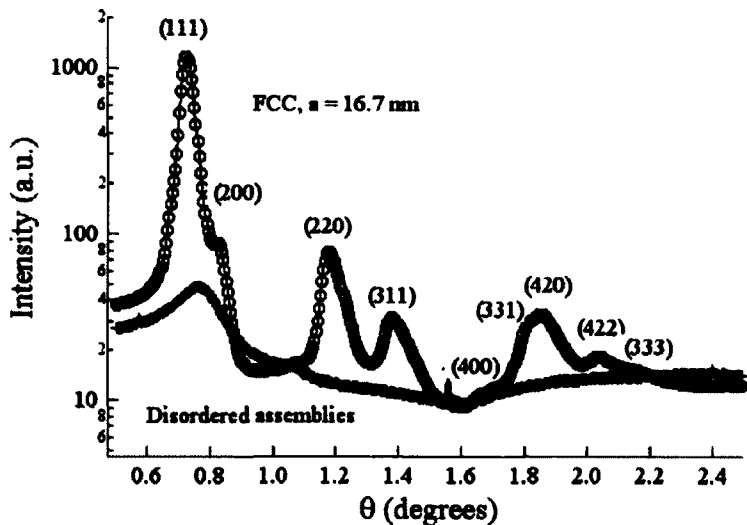


Figure 2.8: SAXS profile showing the clear distinction between well-ordered, FCC nanoparticle crystals and disordered assemblies of 8.5 nm iron nanoparticles. (Reproduced from Ref. 6). In this thesis, a similar procedure was used to prepare Fe_3O_4 nanoparticle crystals for neutron small angle scattering (SANS). The angular range for SANS is lower than for SAXS, and only the region of the (111) and (200) peaks is probed.

2.3 MAGNETIC INTERACTIONS

Ideal monodomain nanoparticles behave superparamagnetically above the blocking temperature. However, in real systems with appreciable particle density (typically > 1 vol. %), interparticle interactions lead to notable deviations from Langevin-like behavior. This region above the blocking temperature, but below the temperature of true superparamagnetism is called the superferromagnetic region.⁷ The term superferromagnetic refers to particles that in the dilute limit would be superparamagnetic, but otherwise have cooperative magnetic interactions. The remainder of this chapter will focus on developing a context for understanding how these interactions modify superparamagnetic behavior.

There is a strong need for models that accurately describe and account for the effects of nanoparticle interactions in the superferromagnetic region. Currently, despite the deviations from ideal superparamagnetic behavior, the Langevin function is often fit to magnetization curves in order to extract the nanoparticle moment or nanoparticle volume following the relationship $\mu = M_S V_{pt}$. Here, μ is the particle moment, M_S is the volume normalized saturation magnetization, and V_{pt} is the volume of the particle. This is an extremely common source of errors in the literature.^{8,9,10,11,12} For the remainder of this chapter we will discuss possible models for describing the deviation from the Langevin function in terms of interparticle interactions using well characterized, well ordered, monodispersed iron oxide nanoparticle crystals as a test case.

2.3.1 REGION OF INTEREST

As discussed in Chapter 1, the zero-field cooled (ZFC) magnetization curve defines the blocking temperature for a given sample and a given measurement time, and is thus a good starting point for characterizing the interactions in a sample. The ZFC magnetization curve shown in Figure 2.9 was measured for nanoparticle crystals of 6.7 nm iron oxide particles under a 200 Oe applied field. As shown by the peak in the ZFC, the average blocking temperature was found to be 60 K.

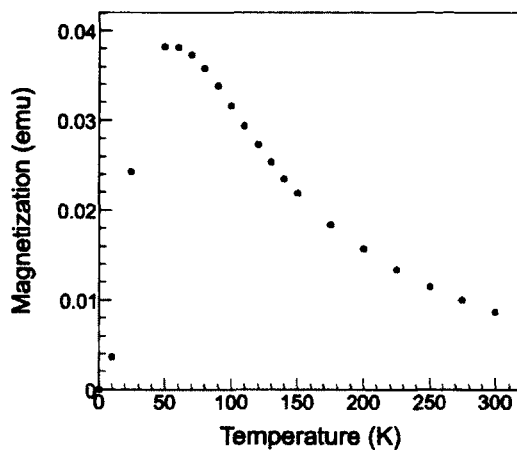


Figure 2.9: Zero-field cooled (ZFC) magnetization curve measured under a 200 Oe applied for a 6.7 nm iron oxide nanoparticle crystals.

In the case of an ideal, non-interacting, monodomain particle system we consider the particles to be superparamagnetic above 60 K. The ZFC curve can be modeled for ideal monodomain particles following the model presented by Sappey, *et al.*,¹³ which indicates that they are blocked below 60 K, where $KV > 25kT$, as given by Eq. 1.4. When they are superparamagnetic, $KV < 25kT$ as given by Eq. 1.4. For the remainder of the chapter, we will describe the region between the blocked state and the purely superparamagnetic where the particles behave superferromagnetically.

We can be sure that any deviations from the Langevin function at any temperature above the blocking temperature are caused by interactions by considering the magnetization curve taken at 60 K as shown in Figure 2.10.

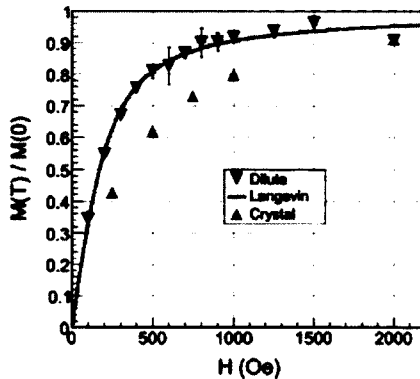


Figure 2.10: Magnetization curves for 6.7 nm iron oxide crystals and a dilute suspension of 6.7 nm iron oxide particles frozen in toluene.

The dilute sample was prepared by diluting a suspension of 6.7 nm iron oxide nanoparticles to a concentration of less than 1% by volume, sealing the suspension in a glass ampoule under vacuum, and freezing the suspension before the application of a magnetic field.

Since the moment per particle in our system is well known, there is no ambiguity in our fits to the Langevin function. We will show in the following sections that the magnetic response of our 6.7 nm iron oxide nanoparticle crystals fits the Langevin function for temperatures above 200 K. Thus, our system is superferromagnetic from 60 K to 200 K and we will focus our efforts on developing an understanding of the interparticle interactions in this regime.

2.3.2 AN EFFECTIVE FIELD MODEL OF INTERACTIONS

Figure 2.10 shows that the deviations in the magnetization from the Langevin function are demagnetizing in nature as the moment of the crystal is lower than the moment given by the Langevin function at moderate fields. The fit at moderate fields is emphasized because the extreme slope at very low and very high fields can lead to fitting artifacts. All magnetization curves were normalized to the saturation magnetization obtained at 10 K. The magnetization is plotted as a function of H/T (Oe/K) because it simplifies the argument of the Langevin function ($x = \mu H/k_B T$). Figure 2.11 shows the calculated Langevin function using the magnetic moment, μ , determined according to the method described in Section 1.2 plotted with the experimental data for the 6.7 nm nanoparticle crystals as a function of temperature.

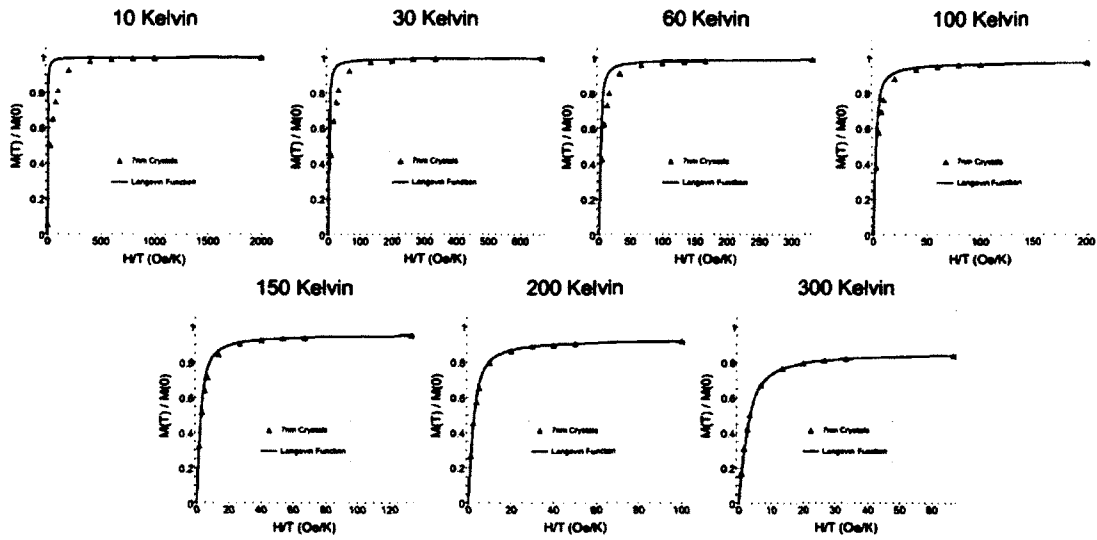


Figure 2.11: Magnetic isotherms showing the measured magnetization of the 6.7 nm nanoparticle crystals and the calculated Langevin function at various temperatures between 10 and 300 K. All magnetization values are normalized to the saturation magnetization at 10 K.

In the first approach to quantifying the effect of interactions, the sample was assumed to obey the Langevin function with a local field equal to the external field minus an effective demagnetizing field, H_{eff} . H_{eff} was calculated for each isotherm by re-fitting the Langevin function to the experimental data using the modified argument $x = \mu(H-H_{\text{eff}}) / k_B T$, where μ is the single particle moment of 7.1×10^{-16} emu, H is the applied field, k_B is Boltzmann's constant, and T is the temperature. The effective field can be thought of as the average negative field that would need to be applied over the whole sample in order to map the experimental data to the Langevin function as illustrated in Figure 2.12. Note that it is appropriate for H_{eff} to have some field dependence because as particles begin to switch the local fields will change. Also, due to the asymptotic approach to saturation, the error bars are the largest at large applied fields. Some sources of this negative field could be from flux closure pathways or spin canting as will be discussed later.

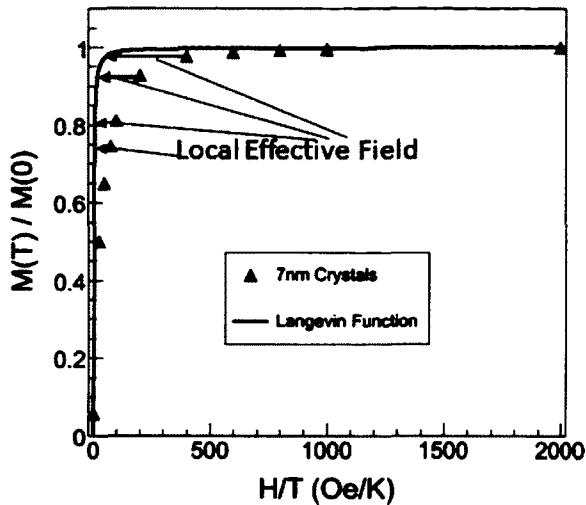


Figure 2.12: Illustration of the effective field used to map the experimental data onto the Langevin function.

The fits of the effective field are presented in Figure 2.13. Notice that close to saturation it is possible that the effective field can become non-physically large due to only a slight mismatch in the measured and Langevin moments. No effort was made in the fitting to threshold these values to avoid non-physical artifacts because the true region of interest for the interactions is in the intermediate field range.

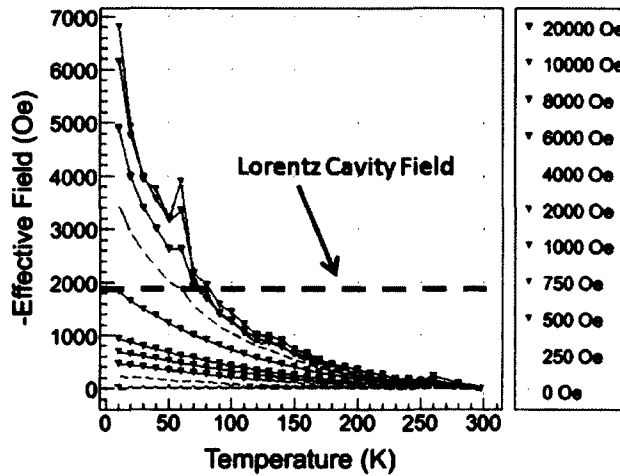


Figure 2.13: Plot of the calculated effective fields as a function of temperature and applied field including the Lorentz cavity field which represents the maximum physical demagnetizing field.

Some of the overall trends in the calculated effective field values are very reasonable. For instance, in the region of low applied field the initial susceptibility is high and in the

effective field is low. In the intermediate fields where the fits of the effective field would be the most reasonable and least prone to artifacts because the slope of the magnetization curve is not extreme, the results are what would be expected qualitatively, but the magnitudes perhaps unphysically large.

2.3.3 DISCUSSION OF EFFECTIVE FIELD CALCULATION RESULTS

To estimate the maximum effective field, we turn to simple magnetostatic calculations. For instance, a simple dipolar field of one particle being felt by its neighbor is well understood and can be easily calculated as discussed previously using Eq. 1.5 to be on the order of tens of Oersteds. While a field of this magnitude is certainly not negligible, especially for low applied fields, it is at least two orders of magnitude lower than our calculated effective fields. We can also make an estimate of the Lorentz cavity field which as we have described previously in Section 1.6 is the field established in a cavity inside a uniformly magnetized sample that opposes the magnetization. In our sample this could arise from nanoparticle voids or packing dislocations. Simply taking the saturation magnetization of our particles and not accounting for the packing fraction of our surfactant-coated spheres, the maximum Lorentz cavity field would be 1850 Oe. None of these values are high enough to account for our calculated effective fields, so this model cannot fit the experimental data.

The vast majority of the literature on quantitative modeling of nanoparticle interactions between nanoparticles does not compare directly to experimental results.^{14,15,17} One model that does incorporates a new temperature $T^* = \alpha\mu^2/(k_B D^3)$ where α is derived from the sum of dipolar energy contributions, μ is the particle moment, k_B is the Boltzmann constant, and D is the average interparticle distance into the denominator of the Langevin argument such that $x = [\mu H/k_B(T+T^*)]$.¹⁶ Physically this is equivalent to our effective demagnetizing field approach. Both cases have an energy barrier and consider adjusting the available energy to overcome it. The authors use the model to describe the deviations from the Langevin function measured on nanocrystalline CuCo melt spun ribbon system that is very different from our nanoparticle assemblies. Separately, Mao *et al.* model deviations from the Langevin function in assemblies of cobalt particles.¹⁷ Their results show an increase in the demagnetizing deviations from the Langevin function with increasing particle density. However, their model assumes their particles pack cubically which shows their fundamental ignorance of the samples that can realistically be made to verify their work. We conclude that interparticle interactions leading to a demagnetizing deviation from purely superparamagnetic behavior cannot be described accurately by a simple demagnetizing effective field because the interaction effects are so strong that any calculated effective field is non-physically large.

2.3.4 DISTRIBUTION OF DIPOLAR INTERACTION FIELDS MODEL

Recently Al Saei *et al.* published a new model incorporating a distribution of dipolar interaction fields into the Langevin model as a means of describing interparticle interactions.¹⁸ This group is very well known for its computational studies of nanoparticle systems and has developed robust numerical tools for approaching these difficult problems over the last several decades. From their numerical simulations, they concluded that there is a distribution of dipolar fields in all directions, and assumed a Gaussian form with a mean close to zero. They concluded that the deviations from the Langevin function in interacting samples cannot be described as demagnetizing because a demagnetizing distribution would have a negatively skewed mean dipolar field. They show that the magnetization of a system of particles with interactions is always lower than that for the non-interacting case for any symmetric distribution of dipolar interaction fields due to the non-linear shape of magnetization curves.¹⁸ Because the magnetization curve for positive applied fields is concave-up, the slope is decreasing for increasing applied fields. This means that with a symmetric distribution of interaction fields the interaction field acting against the applied field will always lower the magnetization to a greater degree than the interaction field of the same magnitude acting with the applied field will raise it.

In a nod to experimentalists, Al Saei *et al.* reduced their dipolar interaction model to a case that only considers distributions of dipolar interaction fields in the z-direction since typical magnetometers are restricted to measuring the component of the magnetization along the direction of the applied field. This model takes the form,

$$\overline{M}_{\text{int}}(H_a) = \int_{-\infty}^{\infty} L(B)f(H_{iz})dH_{iz}, \quad (2.2)$$

where,

$$B = \mu(H_a + H_{iz})/k_B T \quad \text{and} \quad f(H_{iz}) = e^{-H_{iz}^2/2\sigma_{H_{iz}}^2} / \sqrt{2\pi}\sigma_{H_{iz}}. \quad (2.3)$$

Here, H_a is the applied field, H_{iz} is a value of the interaction field in the Gaussian distribution of interaction fields with a standard deviation of $\sigma_{H_{iz}}$. We fit this model to experimental isotherms measured on the 7 nm iron oxide colloidal crystals discussed previously in this chapter. The only free parameter was $\sigma_{H_{iz}}$, and the best fit was determined using a least-squares method. The best values of $\sigma_{H_{iz}}$ were found to be 508, 487, 230, 4, 10, and 3 Oe for isotherm temperatures of 10, 20, 100, 160, 200, and 230 K respectively. The experimental curves and fits are shown in Figure 2.14.

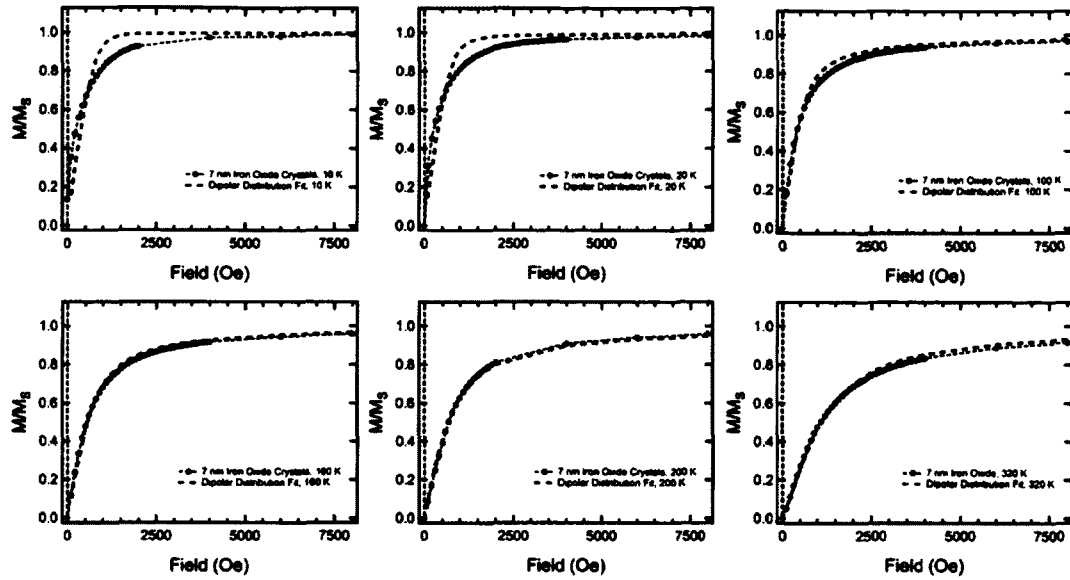


Figure 2.14: Distribution of dipolar interaction fields model fit to experimental isotherms for 7 nm iron oxide colloidal crystals at temperatures of 10, 20, 100, 160, 200, and 320 K.

Notice that there is a strong disagreement between the fits and the data at temperatures below the blocking temperature as would be expected. Also, above 160 K, with a negligible $\sigma_{H_{\text{iz}}}$ of a few Oersted the curve fits very nicely. In the limit of small $\sigma_{H_{\text{iz}}}$, the distributed dipolar interaction fields model reduces to the Langevin function. At the interesting intermediate temperature of 100 K, the fit and the magnitude of the interaction field is very reasonable and well within the physical limits of the interaction field, though the model still overestimates the magnetic moment of the sample.

Al Saei *et al.* show the difference in their calculated isotherms when they included interaction fields in all directions and when the included interaction fields only in the z-direction (along direction of the applied field). Their figure is reproduced in Figure 2.15.

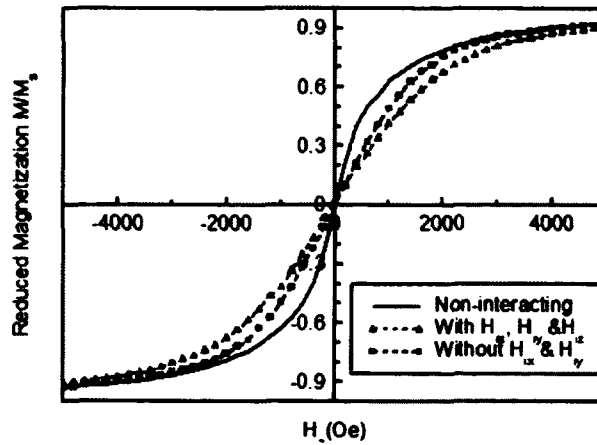


Figure 2.15: Magnetization curves calculated from the distribution of dipolar interaction fields model. These curves were calculated using the physical properties of 6 nm cobalt nanoparticles. (Reproduced from Ref.18)

Notice that the curve including interaction fields in all directions is lower in magnetization at intermediate applied field values than the curve containing interaction fields only in the z-direction. Qualitatively, it seems that if a model containing interaction fields in all directions was available to fit to our experimental data there is a better chance of having strong agreement. Unfortunately, it is difficult to fit such a model to data collected exclusively in the z-direction.

2.4 MEASUREMENT OF THE TRANSVERSE MOMENT

It is clear from the promise of model presented by Al Saei *et al.*¹⁸ that any measurement of a nanoparticle system including information in along at least two orthogonal directions would be extremely useful in the validation of proposed models for nanoparticle interactions. Our Magnetic Properties Measurement System Superconducting Quantum Interference Device Magnetometer (MPMS SQUID) made by Quantum Design includes the optional transverse pickup coil system, and thus in theory has the capability to measure the magnetization of a nanoparticle sample in a direction orthogonal to the applied field.

Naively, one would not expect a transverse moment to be measurable on a macroscopic sample of nanoparticles. In an ideal sample there would be nothing to break symmetry and any transverse moment should average to zero across the sample. Luckily, in practice we do not believe this to be the case.

The longitudinal and transverse flux pickup coils of the MPMS SQUID magnetometer are shown below in Figure 2.16.

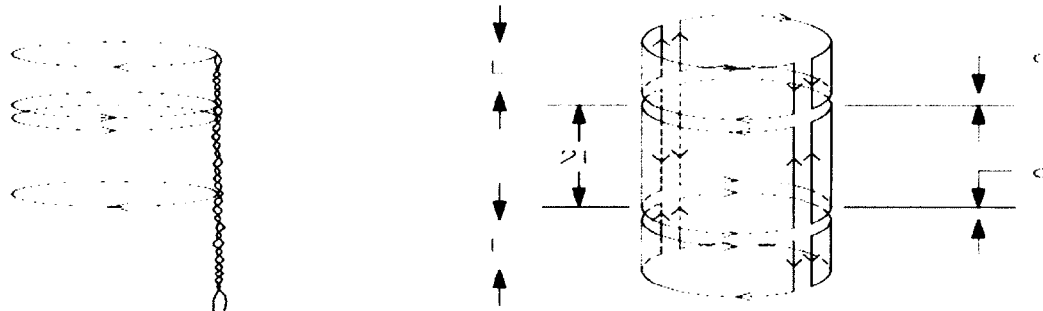


Figure 2.16: Longitudinal MPMS SQUID flux pickup coils (left), and transverse flux pickup coils (right). (Reproduced from Ref. 19).¹⁹

The longitudinal coils are a familiar design with alternating chirality in different loops so as to measure only the gradient of the longitudinal magnetic moment and cancel out any

stray field that is constant. Therefore, the spatially uniform applied field from the superconducting magnet in this region is not measured by the pickup coils.

The transverse coils are far more complicated, and in fact the response function provided by Quantum Design is not analytic, but rather was calculated using a Math-CAD program.²⁰ After centering a sample in the longitudinal transverse coils, it was rotated until the maximum response in the transverse pickup coils was achieved. By doing this, the slight imperfections in the coil design, sample shape, and preparation of the nanoparticle crystals become advantages. First, the pickup coils are more sensitive to closer magnetic moments, and samples are never *perfectly* centered about the z-axis. Second, while the nanoparticle samples are extremely well ordered on the length scale of hundreds of particles, at scales greater than this the sample is polycrystalline in nature. Finally, nanoparticle samples are never perfect disks, but rather a somewhat uneven distribution of crystallites within a disk. These three factors combine to allow a measurably large transverse moment even though the absolute magnitude cannot be quantified. However, the temperature dependence of the transverse moment is meaningful and relevant to the investigation of nanoparticle interactions. There are many more processing steps required to extract the transverse moment from spurious signals, and the details of the procedure used to process the raw data are given in the Appendix. In the end, the transverse moment measured is a fraction of the total transverse moment of the sample and therefore a linear adjustment to scale the measured transverse moment to the total transverse moment is necessary. This linear scaling is physically justifiable. At any rotation of the sample, the measured transverse moment is the vector sum of transverse moments convolved with the axial sensitivity of the pickup coils. The decrease in the magnitude of a measured longitudinal magnetization due to the existence of a transverse moment would only be due to the fact that the transverse moment is orthogonal to the longitudinal moment, not its orientation in the transverse plane. Therefore, it is quite reasonable to scale any measured transverse moment to account for the transverse moments that cancel.

To investigate the deviations between the experimental isotherms and the two models discussed above the transverse moment was measured at 100 K and scaled to fit the difference between each model and the experimental longitudinal isotherms. The scaling factor was calculated using a least squares method between applied fields of 500 and 30000 Oe. The low field region (below 500 Oe) was ignored in the least squares calculation because the difference between the model and the experimental data is negative in that region and its influence dominated the least squares. The negative value was due to a low field crossing of the measured transverse moment and the difference between the models and the experimental longitudinal values. The data are presented below in Figure 2.17.

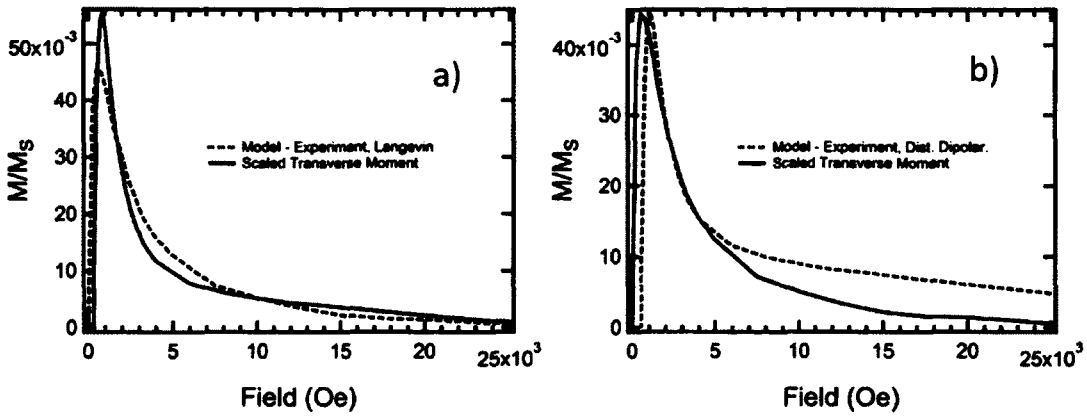


Figure 2.17: Scaled transverse magnetic moment at 100 K plotted with the difference between a) the effective demagnetizing field model discussed in Section 2.3.2 and the experimentally measured longitudinal moment, and b) the distribution of dipolar fields model discussed in Section 2.3.5 and the experimentally measured longitudinal moment.

The strong agreement between the measured transverse moment and the residuals between the measured longitudinal moment and models discussed earlier in this chapter suggests that the transverse measurement presented here is physical. The fact that a measurable transverse moment exists provides useful information about its relevant length scales. For instance, interactions involving flux closure pathways would have to be extremely large geometrically in order to give a net transverse moment in this measurement scheme. Similarly, models in which there would not be a net transverse moment from a single particle can be eliminated. This includes such colorfully coined surface spin configurations as the “hedgehog” structure in which surface spins point outward from the surface,^{21,22,23,24} the “artichoke” structure where spins are parallel to the surface and point from one pole to another,²³ and the “throttled” structure where spins are tilted slightly inward at the south pole and slightly outward at the north pole.²³ The model recently proposed to explain experimental polarized neutron scattering results by Krycka *et al.* in which clusters of 9 nm iron oxide nanoparticle crystals have a surface layer in which the spins are coherently aligned perpendicular to the applied magnetic field would agree with these results well.²⁵ Although it should be emphasized that PASANS measures the perpendicular magnetization on a dramatically different length scale. A complete description of this experiment and model will be given in the next chapter.

2.5 REFERENCES

- ¹ S. Sun, H. Zeng, D. B. Robinson, S. Raoux, P. M. Rice, S. X. Wang, and G. X. Li, *J. Am. Chem. Soc.* 126 (2004).
- ² N. Wrigley, *J. Ultrastructure Res.* 24 (1968), 454.
- ³ ImageJ is available for download at: <http://rsbweb.nih.gov/ij/>.
- ⁴ Talapin, E. V. Shevchenko, A. Kornowski, N. Gaponik, M. Haase, A. L. Rogach, and H. Weller, *Adv. Mater.* 13, No. 24 (2001), 1868.
- ⁵ Shevchenko, D. Talapin, A. Kornowski, F. Wiekhorst, J. Kotzler, M. Haase, A. Rogach, and H. Weller, *Adv. Mater.* 14, No. 4 (2002), 287.
- ⁶ D. Farrell, Y. Cheng, S. Kan, M. Sachan, Y. Ding, S. A. Majetich, and L. Yang, *J. of Phys: Conf. Series* 17 (2005), 185-195.
- ⁷ S. Mørup and G. Christiansen, *J. Appl. Phys.* 73 (1993), 6955.
- ⁸ C. Pascal, J. L. Pascal, F. Favier, M. L. Elidrissi Moubtassim, and C. Payen, *Chem. Mater.* 11 (1999), 141-147.
- ⁹ K. Yakushiji, S. Mitani, K. Takanashi, J. G. Ha, and H. Fujimori, *J. Magn. Magn. Mater.* 212 (2000), 75-81.
- ¹⁰ I. Abu-Aljarayesh, A. Al-Bayrakdar, and S. H. Mahmood, *J. Magn. Magn. Mater.* 123 (1993), 267-272.
- ¹¹ D. K. Kim, Y. Zhang, W. Voit, K. V. Rao, M. Muhammed, *J. Magn. Magn. Mater.* 225 (2001), 30-36.
- ¹² G. F. Goya, *Solid State Comm.* 130 (2004), 783-787.
- ¹³ R. Sappey, E. Vincent, N. Hadacek, F. Chaput, J. P. Boilot, and D. Zins, *Phys. Rev. B* 56 (1997), 14551.
- ¹⁴ D. Kechrakos and K. N. Trohidou, *J. Magn. Magn. Mater.* 262 (2003), 107-110.
- ¹⁵ E. de Biasi, C. A. Ramos, and R. D. Zysler, *J. Magn. Magn. Mater.* 262 (2003), 235-241.
- ¹⁶ P. Allia, M. Coisson, P. Tiberto, F. Vinai, M. Knobel, M. A. Novak, and W. C. Nunes, *Phys. Rev. B* 64 (2001), 144420.
- ¹⁷ Z. Mao, D. Chen, and Z. He, *J. Magn. Magn. Mater.* 320 (2008), 2335-2338.
- ¹⁸ J. Al Saei, M. El-Hilo, and R. W. Chantrell, *J. Appl. Phys.* 110 (2011), 023902.
- ¹⁹ MPMS Application Note, 1014-202 A (2000), Quantum Design Inc.
- ²⁰ Communication with Jim O'Brien of Quantum Design.
- ²¹ J. Mazo-Zuluaga, J. Restrepo, and J. Majía-López, *Physica (Amsterdam)* 398B (2007), 187.
- ²² J. Mazo-Zuluaga, J. Restrepo, F. Munoz, J. Mejia-Lopez, *J. Appl. Phys.* 105 (2009), 123907.
- ²³ L. Berger, Y. Labaye, M. Tamine, and J. M. D. Coey, *Phys. Rev. B.* 77 (2008), 104431.
- ²⁴ Y. Hua and Du, *J. Nanosci. Nanotechnol.* 9 (2009), 5829.
- ²⁵ K.L. Krycka, R. A. Booth, C. R. Hogg, Y. Ijiri, J. A. Borchers, W. C. Chen, S. M. Watson, M. Laver, T. R. Gentile, L. R. Dedon, S. Harris, J. J. Rhyne, and S. A. Majetich, *Phys. Rev. Lett.* 104 (2010), 207203.

Chapter 3

Investigation of Intraparticle Magnetic Structure Using PASANS

3.1 INTRODUTCTION AND MOTIVATION

Neutron scattering is a very useful tool for the evaluation of length scales of magnetic and nuclear structures for sizes ranging from tens of nanometers to a few angstroms. Neutrons interact magnetically due to their quantum mechanical spin of $\frac{1}{2}$. Because they lack charge, they have a very low absorption cross-section in most materials which allows them to probe macroscopically thick samples. These characteristics are the primary advantage of neutrons as a scattering probe. The main disadvantage is the high cost and security concerns related to the production of neutrons at a usefully large flux.

The sources for neutron scattering facilities are either spallation sources or nuclear reactors. Spallation sources create neutrons by using a particle accelerator to bombard a heavy metal target so that it releases neutrons. They are easily pulsed, and are thus useful for time dependent measurements. A reactor source is a small nuclear reactor with holes in the containment shield that allow neutrons to exit and be guided into experiments. The experiments discussed here were completed at the National Institute of Standards and Technology (NIST) Center for Neutron Research (NCNR) in Gaithersburg, MD using a 20 MW heavy-water nuclear reactor as a neutron source. The neutrons used in these experiments are considered thermal neutrons. They lose energy in the heavy water mediator of the reactor and are in thermal equilibrium with their surroundings by the time they reach the experiment. The distribution in their energies follows the Maxwell-Boltzmann relation at room temperature.

This chapter introduces the technique of polarization analyzed small angle neutron scattering (PASANS) which was developed over the course of the work presented here. We discuss its use in determining the intraparticle magnetic structure of 9 nm iron oxide nanoparticle crystals prepared with the same techniques outlined in previous chapters.¹ The use of magnetic materials at small length scales is becoming increasingly important for applications from medicine² to data storage.³ Iron oxide is used for medical applications because of its inherent biocompatibility and low cost. Although it will not likely be used for data storage because of its low anisotropy, similar

sized structures will be used and the techniques developed here to investigate these structures will be extremely useful. Single phase Magnetite particles of this size are usually considered to be monodomain—meaning that all atomic spins act coherently as one spin—in reality, their structures are far more complex.⁴ The measurements presented in this chapter show the application of a novel technique to and the subsequent determination of a novel, counterintuitive intraparticle magnetic structure. Most of the results discussed in this chapter have been published.^{34,17,30,31,5}

3.2 TRADITIONAL SANS EXPERIMENTS

Small angle neutron scattering (SANS) is physically very similar to small angle x-ray scattering (SAXS) in terms of the length scales probed, but while x-rays interact primarily with electrons, neutrons interact primarily with nuclei. For many experiments, the dramatically higher flux from x-ray sources compared to neutron sources favors the use of x-ray experiments, but specific conditions favor the use of neutrons. For instance, x-ray scattering scales with the number of electrons in an atom. In low-Z materials like polymers and biological materials which are primarily composed of hydrogen and carbon atoms, the higher flux of x-ray sources is compensated by the higher scattering rate from neutron sources.

Additionally, the neutron scattering length density of hydrogen is very similar in magnitude, but opposite in sign from deuterium. Because hydrogen is easily substituted for deuterium in most compounds this allows for a very accurate tailoring of neutron scattering contrast.⁶ For instance, if the length scales of a polymer suspended in hexane were of interest they could be probed directly with no contribution from the hexane background by combining hexane (C_6H_{14}) and deuterated hexane (C_6D_{14}) in the appropriate ratio such that the scattering length density of the combined solvent is zero. Experiments like this are now so routine that NIST provides an online tool to calculate the scattering length density of various solvent combinations.⁷ SANS is also very useful for the determination of magnetic structure because of the strong interaction between the neutron spin and magnetic fields.

In the most general case, the scattering cross section, σ , is proportional to the spatial Fourier transform of the nuclear (structural) and magnetic scattering length density $\rho_{N,M}$ defined as,

$$N, M(\mathbf{Q}) = \sum_K \rho_{N,M}(K) e^{i\mathbf{Q} \cdot \mathbf{R}_K} \quad (3.1)$$

where J is any Cartesian coordinate and \mathbf{R}_K is the relative position of the K th scatterer. This can also be considered as the product of the form factor, which is the Fourier transform from the scattering centers within one scattering unit, and the structure factor, which is the Fourier transform of the relative locations of the scattering units.³¹ For instance, face-centered cubic (FCC) packed hard spheres would have a hard spherical form factor, and an FCC structure factor.

If only the magnetic structure is of interest, the nuclear and magnetic scattering need to be separated. In unpolarized magnetic SANS experiments the nuclear scattering background is subtracted from the total signal by taking advantage of the scattering

geometry from a magnetically saturated state. Nuclear scattering is isotropic with respect to the scattering wave vector, \mathbf{Q} , but magnetic scattering only occurs from magnetic components perpendicular to \mathbf{Q} . Thus, a truly saturated state only contains nuclear scattering in the applied field direction, as shown along the x-axis in Figure 3.1.

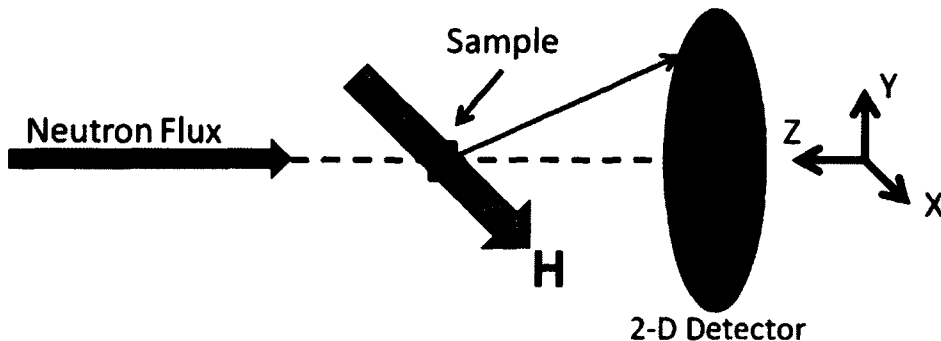


Figure 3.1: Schematic of unpolarized neutron scattering experiment. The 2-D detector array is located in the X,Y-plane as illustrated. A magnetic sample saturated along the applied field direction (x-axis) only contains nuclear scattering in the x-direction.

For the SANS apparatus, 2D scattering patterns are measured by a position sensitive detector array. The detector has an area of 640 mm x 640 mm with a 5.08 mm x 5.08 mm resolution and its distance from the sample can be varied continuously from between 1.3 m and 13.1 m to change the accessible \mathbf{Q} range. The detector is filled with mixture of ^3He and CF_4 gas at about 243 kPa. ^3He is used because it is a very efficient absorber of thermal neutrons. The absorption is shown in the reaction below,



When a neutron is absorbed, a proton (^1H) and tritium nucleus (^3H) are released in opposite directions with a combined kinetic energy of 765 keV which ionizes surrounding CF_4 gas. The CF_4 ions are attracted to an anode held at high voltage where they generate a signal.⁸ Slightly varying sensitivities at different positions in the array are accounted for by taking occasional measurements of the scattering through water or Teflon (PTFE), which are known to have highly isotropic scattering with well known \mathbf{Q} dependence.

In the analysis of the 2D scattering data, sector cuts are taken about a desired direction. The size of a sector cut is chosen as a compromise between increasing statistics and broadening the physics of interest with increasing sector size. To subtract the nuclear scattering contribution from a unpolarized SANS data, $\pm 10^\circ$ sectors would be averaged and normalized by area about the positive and negative x-axis to extract purely nuclear scattering from a saturated sample. The accuracy of this procedure breaks down in the event that a sample cannot be saturated completely.⁹ For all the data presented in this chapter, the maximum available field was 1.2 T. Although greater fields could be

attained by a superconducting magnet, space constraints introduced by the polarization analyzer necessitated the use of a traditional electromagnet.

3.3 POLARIZATION ANALYZED SMALL ANGLE NEUTRON SCATTERING (PASANS)

The advantages of unpolarized SANS experiment are the simplicity of the experiment, the ease of analysis, and the speed with which the necessary scattering statistics can be accumulated, but PASANS is much more powerful. It does not necessitate that the sample is saturated to remove background nuclear scattering, and including the spin degree of freedom of the neutrons before and after interacting with the sample allows the collection of a much greater amount of information than with proper analysis allows the full 3D separation of magnetic structure. This is due to the ability of PASANS to distinguish between non-spin-flip (NSF) and spin-flip (SF) scattering events. The terms refer to whether or not the neutron spin flips from one spin state to another or not. NSF events will be denoted by either + + or - -, and SF events will be denoted by + - or - +, where the first sign corresponds to the initial neutron polarization state and the second corresponds to the final neutron polarization state. Whether a magnetic moment (or for our purposes the magnetic scattering amplitude, M , from Eq. 3.1) contributes to NSF or SF scattering is governed by two general rules. First, only the component of M perpendicular to Q participates in neutron scattering (as was just discussed in the method for subtracting the nuclear contribution by saturating a sample in unpolarized magnetic SANS). Second, of the moments perpendicular to Q , components parallel to the neutron polarization axis, p , contribute to NSF scattering and the remaining components perpendicular to p contribute to SF scattering. Additionally, all nuclear scattering (represented by the nuclear scattering amplitude N in Eq. 3.1) contributes to NSF scattering.^{31,19,10}

3.3.1 THE VELOCITY SELECTOR

A velocity selector takes advantage of the particle nature of neutrons. It is mechanical device consisting of a rotating turbine made from a strongly absorbing material whose rotational speed and pitch correspond to the speed of the neutrons allowed to pass, and thus their wavelength.¹¹ The velocity selector preceding the instrument allows for the selection of wavelengths between 5.0 and 20.0 Å by varying the selector speed. The selection of wavelength spreads between 10% and 30% is controlled by varying the selector pitch.¹² Wavelength spread is defined as $\Delta\lambda/\lambda$ at full-width, half-max (FWHM).

3.3.2 THE SUPERMIRROR

In a PASANS experiment the incident neutron beam which contains an equal number of spin up and spin down neutrons is polarized by a supermirror structure. The concept of polarizing neutrons using a supermirror structure was first proposed in 1967

and developed throughout the decade thereafter.^{13,14,15} A supermirror uses a complex multilayer structure of many alternating magnetic and non-magnetic layers that takes advantage of polarization dependent specular scattering from ferromagnetic layers as shown in Figure 3.2. Supermirrors structures are optimized to maximize the reflection of one polarization state and minimize the reflection of the other while maximizing the angle of total external reflection.

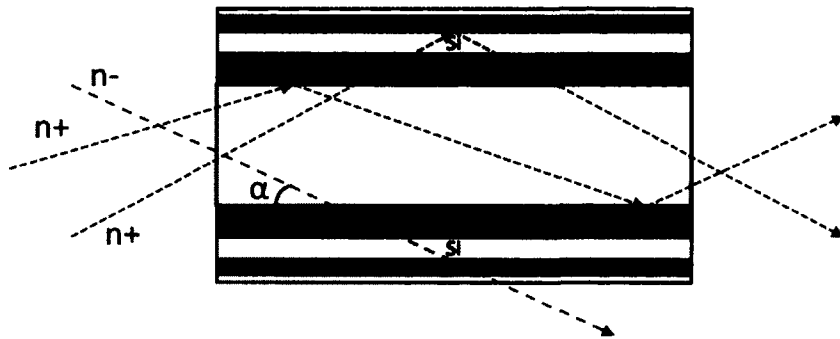


Figure 3.2: A simplified schematic of an FeSi neutron supermirror cavity showing the preferential reflection of spin up neutrons and the transmission of spin down neutrons. The angle between the incident wave vector and the mirror is shown as angle between the incident wave vector and the mirror is shown as α . In reality there would be many more multilayers.

To understand the supermirror structure, it is useful to consider more familiar optical principles such as thin film interference as an analog for supermirror structures. Optically, the maximum angle of total external reflection is the maximum angle between the plane of a mirror and the incident wave vector such that 100% of incident light is reflected. This is important because as neutrons are reflected down the 60 mm x 60 mm guides¹² to the SANS experiment they develop a distribution of incident angles. A wide range of incident angles accepted by the supermirror increases polarized neutron flux for an experiment. The thicknesses of the alternating layers in a supermirror are chosen so that the polarization state reflected from the magnetic layer constructively interferes with that reflected from the layer above it—as in optical thin films—while the opposite polarization state passes through. If only a fixed wavelength and incident angle of neutrons were of interest the layers would all be the same thickness. Instead, supermirrors are intended to polarize a relatively broad range of neutron wavelengths and a monotonically decreasing layer thickness is used.¹⁶ Our experiments used an Fe/Si supermirror to polarize a well collimated incident beam of neutrons to a polarization efficiency of 0.94 at a wavelength of 7.5 Å with a 15% wavelength spread. The polarization efficiency is defined as the absolute value of the difference between the intensities of the two spin states normalized by the sum of the intensities of the two spin states.

Modern supermirrors using $\text{Fe}_{50}\text{Co}_{48}\text{V}_2/\text{TiN}_x$ multilayer structures have been constructed with coercive fields as low as 50 Oe in which the transmitted neutron

polarization can be changed by *in situ* switching of the mirror magnetization.¹⁶ This was not possible in our apparatus, so a separate component called a flipper was necessary to allow access to incident neutrons of both polarization states.

3.3.3 THE FLIPPER

The polarization state of neutrons is maintained in the presence of a finite magnetic field that varies slowly compared to the Larmor precession frequency of the neutrons. If these conditions are carefully met, the spin direction is preserved while the polarization direction can be changed adiabatically. Conversely, if one intends to switch the polarization state (i.e. flip the polarization direction by 180° from spin up to spin down) of the neutrons it is necessary to apply a very rapidly changing, precisely controlled magnetic field. This is the role played by the flipper.

The flipper is an electromagnetic coil that abruptly rotates the polarization axis to an orthogonal direction and back. This can be optimized for different neutron wavelengths—and thus different linear velocities—so that in the time the field is in the orthogonal direction the neutron precesses about the orthogonal axis by π radians and returns to the original guide field anti-parallel to its original state.³¹ The precession coil flipper used in this experiment had an efficiency of 0.95 and was used to switch between the up (+) and down (-) states.¹⁷

3.3.4 THE ^3He ANALYZER

Supermirrors cannot be used as analyzers after the sample scattering for SANS experiments because their acceptance angle (limited by the maximum angle of total external reflection) is at best a few degrees. This would limit the SANS Q-range so much that most experiments could not be performed. Luckily, as we discussed in our description of the 2D area detector, ^3He gas is a very efficient neutron absorber. More specifically, ^3He atoms have a very large absorption cross section for neutrons anti-parallel to the ^3He polarization and a very small absorption cross section for neutrons parallel to the ^3He polarization. After passing through a sufficient length of 100% polarized ^3He gas, all parallel spins will be passed and all anti-parallel spins will be absorbed, giving a transmission of 50% relative to an unpolarized initial flux. Thus, polarized ^3He gas has the potential to be an excellent neutron polarization analyzer, but its use has been limited^{18,19,20,21} until very recently²² due to experimental challenges.

^3He is naturally very scarce. The small amounts of the gas available are products of tritium decay and are either harvested from nuclear weapon storage facilities or heavy water nuclear reactors. The international reduction of nuclear arms stores has reduced the production from the first source since the end of the Cold War. Likewise, heavy water reactors are increasingly less common. The NCNR reactor in Gaithersburg, MD is the last domestic heavy water reactor. Secondly, the cylindrical glass cell must be made from specialty glass boron free glass due to the high neutron absorption cross section of boron. Typically, GE180 glass is used because it is boron free and has a low permeability to ^3He .²³ Fused silica is much more readily available, has a low neutron absorption cross section, and has been used for ^3He cells,²⁴ but is slightly permeable to

^3He and is not stable over long periods of time. The ^3He pressure in SANS cells is typically about 975 Torr.²³

There are two known methods for the polarization of ^3He gas. The first is called the metastability-exchange optical pumping (MEOP) method and involves the direct optical pumping of ^3He atoms at pressures of around 1 Torr, followed by the compression of the polarized gas to near atmospheric pressures (1 atm = 760 Torr) where it has sufficient density to be practical as a neutron spin filter.^{25,26} The second method is spin-exchange optical pumping (SEOP). SEOP is currently the preferred method as it is more suitable for long-term operation because the process does not require a pressure change. The development of high-powered, narrow-band diode lasers has recently made the SEOP method practical. For this method a very small amount of rubidium and some nitrogen is added to the ^3He cell. To polarize the ^3He gas the cell is typically heated to a temperature between 80 °C and 130 °C to ensure the Rb vapor pressure is sufficiently high.²⁷ Optical pumping with tens of watts of circularly polarized light at 794.7 nm spin-polarizes both the electron and nuclear spins of the Rb atoms which polarize the ^3He nucleus during collisions via the hyperfine interaction.²⁷ A small amount of nitrogen is added to absorb the mostly unpolarized light radiated during the Rb relaxation and increases the efficiency of the ^3He polarization process.

The polarization of the ^3He gas is monitored during the SEOP process, and *in situ* on the beamline using nuclear magnetic resonance (NMR) to quantify the polarization of the ^3He gas. The NMR signal is calibrated by measurements of the absolute transmission of both polarization states.²⁸ The polarization of the cell is protected from depolarizing magnetic gradients by transporting it to the beam line, and installing it in a solenoid with a field of about 50 G oriented in the z-direction defined in Figure 4.1.¹⁸ To switch from between spin up and spin down majority states the polarization of the ^3He cell is flipped with an pulsed field via Larmor precession and verified by a subsequent NMR measurement.

3.3.5 MAGNETIC GUIDE FIELDS

Finally, it is important to clarify the role of guide fields in maintaining the polarization of neutrons in the path between the supermirror polarizer and the ^3He analyzer. Polarized neutrons must always be in a non-zero guide field in order for their polarization direction (parallel or anti-parallel to the guide field) to be well defined. The direction of the guide field sets the local polarization direction. As long as it varies slowly with respect to the Larmor precession frequency of the neutrons, the polarization direction will change adiabatically.

The ability to slowly change the polarization direction without losing information about the neutron spin allows for the polarization direction at various elements throughout the experiment to be chosen based on convenience. After the supermirror, flipper, and beam aperture, guide fields created by stacks of ferrite magnets maintain the polarization of the neutrons as they enter the area between the poles of the electromagnet in which the sample is located. The area between the magnet poles immediately before the sample defines the polarization direction for the scattering events as parallel to the applied magnetic field. Even with the electromagnet de-energized, the remanent field in the pole pieces is sufficient to define the neutron polarization direction. After the sample

ferrite magnet stacks and solenoids slowly rotate the guide field from the x-direction to the z-direction before the neutrons pass through the ^3He analyzer which is polarized in the z-direction. If care is taken in the placement of guide fields the only magnetic interactions fast enough to flip the neutron spin direction are those from appropriately oriented spins in the sample.

3.4 POLARIZATION CORRECTIONS

Even in the best conditions, the polarization of ^3He cells decays exponentially. With the current setup the relaxation time, Γ , is 150-300 hours and the time dependence of the polarization must be explicitly included in the data analysis. The range of relaxation times varies widely due to stray field gradients, but is measured explicitly during the course of each experiment. The maximum possible relaxation rate is limited by depolarizing dipole-dipole interactions between ^3He atoms during a collision to $807/P$ hours where P is the ^3He partial pressure in units of bar.²⁸

In describing the polarization elements we refer to the majority spins as those intended to be passed by a polarization filter and the minority spins as those intended to be blocked. The time dependent majority/minority spin transmission through the ^3He cell is described as

$$T(t) = T_e e^{-(1 \pm P_{\text{He}})l} \quad (3.3)$$

where T_e is the empty cell transmission of 0.86-0.87, l is the opacity which varies from 2-3 depending on the cell used, and P_{He} is the ^3He polarization. P_{He} is described by

$$P_{\text{He}}(t) = P_0 e^{-t/\Gamma} \quad (3.4)$$

where t is the elapsed time and P_0 is the initial polarization which is typically about 0.7.¹⁷

Both the initial, P_0 , and time dependent, P_{He} , ^3He polarization efficiencies are measured in two complimentary ways. The first is using in situ NMR measurements to occasionally measure the polarization. The second method is more direct and is used to calibrate the NMR signal. It measures the transmission over a given time period with the supermirror, and ^3He cell removed from the beam, then a transmission just ^3He cell in the beam. When the empty cell transmission and opacity are accounted for, this method assumes an equal mix of incident neutron spin states, and allows a straightforward calculation of the ^3He analyzer polarization by setting the normalized transmission equal to the left hand side of Eq. 4.3.

Incomplete beam polarization and spin leakage are accounted for using Equation 3.5 remove the time varying efficiencies from all four experimentally measured intensities I_{++} , I_{+-} , I_{-+} , and I_{--} where the first subscript represents the beam polarization and the second subscript represents the analyzer polarization. The initial spin state is changed by turning the precession flipping coils on or off, and the analyzer state is controlled by reversing the cell polarization using Larmor procession, as discussed in the description of the precession coil flippers, and subsequently verifying the state using in situ nuclear magnetic resonance (NMR).

$$\begin{bmatrix} N_+^+ T_+^+ & N_+^- T_+^+ & N_-^+ T_+^- & N_-^- T_+^- \\ N_+^+ T_+^- & N_-^- T_+^+ & N_-^+ T_+^- & N_-^- T_+^+ \\ N_+^+ T_-^+ & N_-^- T_-^+ & N_-^+ T_-^- & N_-^- T_-^- \\ N_+^+ T_-^- & N_-^- T_-^+ & N_-^+ T_-^- & N_-^- T_-^+ \end{bmatrix} \begin{bmatrix} \sigma^{++} \\ \sigma^{-+} \\ \sigma^{--} \\ \sigma^{+-} \end{bmatrix} = \begin{bmatrix} I_{++} \\ I_{-+} \\ I_{--} \\ I_{+-} \end{bmatrix} \quad (3.5)$$

$N^{+,-}$ and $T^{+,-}$ are the efficiencies of the polarizing elements, and are defined as the percentage of (+) or (-) neutrons transmitted through the combination of the supermirror and flipper, and through the ${}^3\text{He}$ analyzer, respectively. Subscript spins indicate the majority spin direction of the polarizing element and superscript spins indicate the majority spin direction recorded by the detector. The majority spin direction is the state intended to be passed by a filtering element. After experimentally determining the values for the I 's, N 's, and T 's, Eq. 3.5 is solved to obtain the four scattering cross sections, σ_{++} , σ_{-+} , σ_{--} , and σ_{+-} .¹⁷

The values of T are calculated using Eq. 3.3 and Eq. 3.4. Occasional measurements of the ${}^3\text{He}$ polarization using NMR absorption and occasional measurements of the absolute transmission through the cell provide the data to track the exponential polarization decay in the analyzer and calculate the cell lifetime Γ .¹⁷ The determination of the values for N are slightly more involved as they include both the polarization efficiency of the supermirror, P_{SM} , and the flipper efficiency, P_F . The majority spin fractions are given by $(1+P)/2$ and the minority spin fractions are given by $(1-P)/2$ for the appropriate efficiencies. It is also important here to include the environmental depolarization of spins due to stray magnetic fields in the beam path as χ_D . This environmental depolarization couples to the supermirror polarization efficiency as $P'_{SM} = (1 - \chi_D)P_{SM}$. Thus, it follows that

$$N_+^+ = \left(\frac{1+P'_{SM}}{2} \right) \quad (3.6)$$

$$N_+^- = \left(\frac{1-P'_{SM}}{2} \right) \quad (3.7)$$

$$N_-^+ = \left(\frac{1-P_F P'_{SM}}{2} \right) \quad (3.8)$$

$$N_-^- = \left(\frac{1+P_F P'_{SM}}{2} \right) \quad (3.9)$$

where it is implied that the neutrons exit the supermirror in the (+) state.¹⁷

Without a sample present scattering conditions simplify the calculation of the supermirror and flipper efficiencies. Because the neutrons do not pass through any magnetic material there isn't any SF scattering and thus the spin flip cross sections can be taken as zero, $\sigma^{+-} = \sigma^{-+} = 0$. Similarly, it can be assumed that the NSF scattering is equivalent and $\sigma^{++} = \sigma^{--}$. With these adjustments, experimental transmission measurements, I , of the main beam for all four cross-sections can be used to calculate P'_{SM} and P_F .¹⁷

$$P_{SM} = \frac{(T_+^+ + T_-^-) - (T_+^- + T_-^+) \left(\frac{I_{++}}{I_{+-}} \right)}{(T_+^+ - T_-^-) \left(\frac{I_{++}}{I_{+-}} \right) - (T_+^- - T_-^+) \left(\frac{I_{--}}{I_{-+}} \right)} \quad (3.10)$$

$$P_F = \frac{1}{P_{SM}} \frac{(T_-^+ + T_+^-) - (T_-^- + T_+^+) \left(\frac{I_{--}}{I_{-+}} \right)}{(T_-^+ - T_+^-) \left(\frac{I_{--}}{I_{-+}} \right) - (T_-^- + T_+^+) \left(\frac{I_{++}}{I_{+-}} \right)} \quad (3.11)$$

All calculations made for the polarization correction are made pixel by pixel on the full 2D datasets.

3.5 EXTRACTION OF 3D MAGNETIC STRUCTURE FROM SCATTERING DATA

After the necessary corrections have been made to account for the time dependent polarization efficiency in the ${}^3\text{He}$ cell the desired physics can be extracted. A schematic of the final experimental setup is shown in Figure 3.3a, typical polarization corrected data is shown for all scattering cross sections in Figure 3.3b. From this point on, all cross sections considered have been corrected for the time dependent polarization efficiencies.

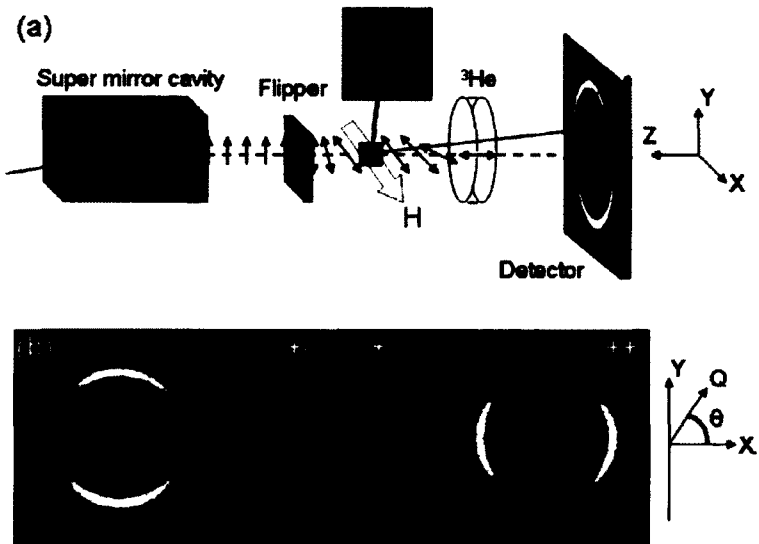


Figure 3.3: a) Schematic of experimental setup including the supermirror, flipper, sample, applied magnetic field, ${}^3\text{He}$ cell, and detector from left to right. Notice that as long as the polarization axis varies slowly, spin information is retained. This allows for the use of convenient geometries for the applied magnetic field and the ${}^3\text{He}$ polarization axis. b) 2D polarization corrected SANS data taken at 1.2 T and 200 K. Notice that θ is measured with respect to the x-axis. (Reproduced from Ref. 34).

To extract the 3D magnetic structure from the 2D intensity plots like the ones shown in Figure 4.3b, $\pm 10^\circ$ area normalized sector averages at θ 's where selection rules

greatly simplify the analysis. This allows the unambiguous separation of N^2 , M_{PARL}^2 , and M_{PERP}^2 , which represent the nuclear scattering profile, the magnetic scattering profile parallel to the applied magnetic field, and the magnetic scattering profile perpendicular to the applied magnetic field, respectively. The selection rules used in this analysis were first derived by Moon, Riste, and Koehler²⁹ and as given in Ref. 34 are:

$$N^2(Q) = \frac{1}{2}(\sigma_{\theta=0^\circ}^{++} + \sigma_{\theta=0^\circ}^{--}) \quad (3.12)$$

$$M_{\text{PARL}}^2(Q) = \frac{(\sigma_{\theta=90^\circ}^{--} - \sigma_{\theta=90^\circ}^{++})^2}{16 N^2} \quad (3.13)$$

$$M_{\text{PERP}}^2(Q) = \frac{1}{6}(\sigma_{\theta=0^\circ, 90^\circ}^{+-} + \sigma_{\theta=0^\circ, 90^\circ}^{-+}) \quad (3.14)$$

$$M_{\text{PARL}}^2(Q) = (\sigma_{\theta=45^\circ, 135^\circ}^{+-} + \sigma_{\theta=45^\circ, 135^\circ}^{-+}) - 5M_{\text{PERP}}^2 \quad (3.15)$$

While selection rules can be calculated to separate the magnetism fully into the x, y, and z-directions, nothing in our sample breaks symmetry in the perpendicular (y, and z-directions) so it is useful to combine statistics for some results and speak only in terms of the uniquely defined directions parallel and perpendicular to the applied magnetic field.

When the magnetization is separated further and presented for the x, y, and z-directions (as in Figure 4.5 below) to verify the separation for magnetic arrangements of known symmetry the scattering cross sections were processed using the following relations as given in Ref. 17:

$$N^2(Q) \propto (\sigma_{\theta=0^\circ}^{++} + \sigma_{\theta=0^\circ}^{--}) \quad (3.16)$$

$$M_x^2(Q) \propto (\sigma_{\theta=90^\circ}^{++} + \sigma_{\theta=90^\circ}^{--}) - N^2 \quad (3.17)$$

$$M_z^2(Q) \propto (\sigma_{\theta=90^\circ}^{+-} + \sigma_{\theta=90^\circ}^{-+}) \quad (3.18)$$

$$M_y^2(Q) \propto (\sigma_{\theta=0^\circ}^{+-} + \sigma_{\theta=0^\circ}^{-+}) - M_z^2 \quad (3.19)$$

An exhaustive set of selection rules in addition to these has recently been derived by Krycka *et al.*^{30,31} The derivation of the selection rules is conceptually straightforward and based only on the SF and NSF scattering rules for the relative orientations of \mathbf{M} , \mathbf{Q} , and \mathbf{p} , the magnetic moment, scattering vector, and neutron polarization directions as discussed at the end of Section 3.2.

3.6 RESULTS AND DISCUSSION

3.6.1 INTERPARTICLE INTERACTIONS

To confirm the viability of our model for the extraction of magnetic scattering profiles in three dimensions using the PASANS analysis, a measurement was made on

the 9 nm iron oxide sample at the electromagnet's remanent field of approximately 25 G and 50 K where the magnetic scattering is expected to be isotropic. The polarization corrected data are shown in Figure 3.4. Generally, these 2D plots contain a Bragg peak due to the particle packing as can be seen near the corners of the NSF data on the left of Fig. 3.4, and an upturn at low-Q near the center and towards the beamstop that corresponds to the long range order. Approximate ordering length scales, L , can be extracted from scattering profiles following the $L=2\pi/Q$ relationship.

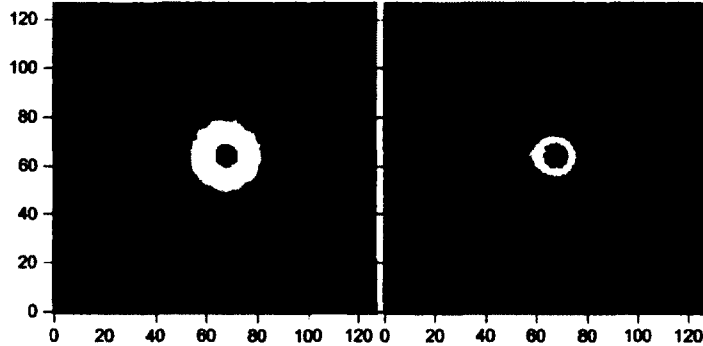


Figure 3.4: Scattering at 50 K in a remanent field of about 25 G. The horizontal and vertical axes represent the pixel number. The image on the left shows NSF scattering dominated by nuclear scattering. The image on the right shows SF scattering is asymmetric due to the M_z scattering along the y-direction, and $M_z + M_y$ scattering along the x-direction. All four cross-sections are not shown due to the similarity between the two NSF patterns and the two SF patterns. (Reproduced from Ref. 17).

The processed, separated data is shown in Figure 3.5. As anticipated from a measurement at remanent field, the magnetic scattering profiles are nearly identical along the x, y, and z-directions. The x-direction is slightly favored because it is the direction of the small remanent field. The nuclear scattering profile shows a Bragg peak that corresponds to the (111) and (200) peaks for the face-centered cubic (FCC) structure that are nearly overlapping and form one large peak due to instrumental broadening mainly caused by the ~15% wavelength spread.

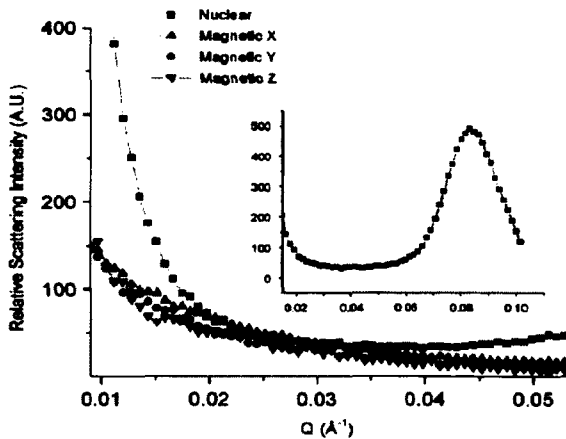


Figure 3.5: Nuclear and magnetic scattering profiles at 50 K and in a remanent field of approximately 25 G. The nuclear scattering exhibits a Bragg peak as expected at 0.083 \AA^{-1} . The magnetic scattering is nearly isotropic, but slightly favors the x-direction because it is the direction of the remanent field. (Reproduced from Ref. 17).

A close look at the low-Q scattering along the x-axis at a series of temperatures in a remanent field gives useful information about the ordering length scales as a function of temperature as shown in Figure 3.6. There is an inverse relationship between the scattering vector, \mathbf{Q} , length scales associated with the scattering structures. Most generally, lower \mathbf{Q} means longer range ordering.

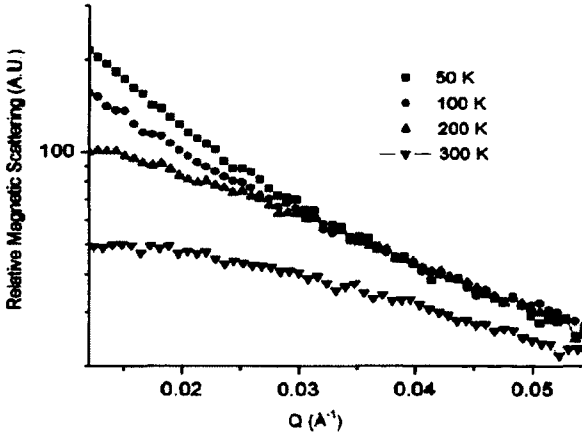


Figure 3.6: Low-Q magnetic scattering in the x-direction in 25 G remanent field representing decreasing long range order as a function of increasing temperature. The ordering continues to decrease well above the blocking temperature of 60 K. (Reprinted from Ref. 17).

One of the most interesting features of Figure 3.6 is that the long range order of $L \sim 300$ nm does not decrease sharply at the blocking temperature—which is measured to be about 60 K as the peak in the ZFC curve—as would be expected if the iron oxide particles became truly superparamagnetic. Due to magnetostatic interactions, there are multi-particle magnetic correlations at temperatures above the peak in the ZFC curve.

At higher \mathbf{Q} , the separation of the magnetic scattering into parallel and perpendicular components at 50 K and 25 G remanent field show magnetic ordering in the x-direction parallel to the applied field with a peak very near the nuclear Bragg peak as shown in Figure 3.7. This is the major advantage of using well ordered crystals of nanoparticles for neutron scattering experiments. The crystalline structure enhances the magnetic scattering at the Bragg peak, allowing useful statistics to be gathered more quickly and interpreted more easily.

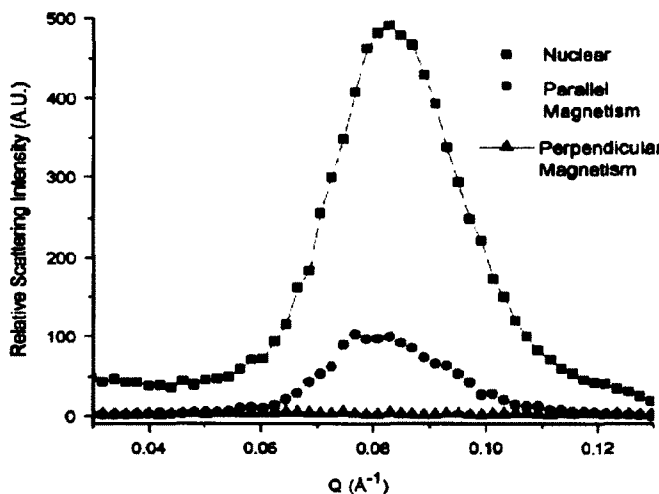


Figure 3.7: Nuclear, and magnetic scattering parallel and perpendicular to a 1.2 T applied field at 50 K. The nuclear scattering shows the interparticle Bragg peak, and the magnetic scattering is dominated by scattering parallel to the magnetic field. (Reproduced from Ref. 17).

Because the large applied field led to significant depolarization of the beam, data in the positive x-quadrant were excluded from this analysis. The depolarization was the result of imperfect guide fields. The guide fields are designed to adiabatically rotate the neutron polarization axis from the x-direction along the applied field to the z-direction of the analyzer polarization. At higher applied fields, discontinuities in the guide fields can be stronger and depolarize the beam to a greater degree. The SF cross sections are most sensitive to beam depolarization, and therefore after excluding the affected quadrant there were not enough statistics to warrant the separation of the perpendicular magnetic scattering further into the y and z-components.

These measured interparticle interactions, while only qualitative in nature agree, well with both the longitudinal and transverse DC SQUID measurements of the magnetic moment of a similar sample discussed in the previous chapter. While encouraging, it should be emphasized that the measurement times, averaging, and measured length scales

associated with the PASANS and DC SQUID magnetometry measurements are extremely different. As the transverse SQUID technique and PASANS are developed further the complimentary information gathered from the two techniques could prove very useful.

3.6.2 INTRAPARTICLE STRUCTURE

Scattering measurements made at 200 K and an applied field of 1.2 T show similar structure in the x-direction, parallel to the applied field as those taken at 50 K and 1.2 T, but the perpendicular magnetic scattering is dramatically different. The raw data, corrected for the time dependent polarization contributions, is shown below in Figure 3.8. The data was processed according to Eqs. 3.12-3.15 is shown in Figure 3.9.

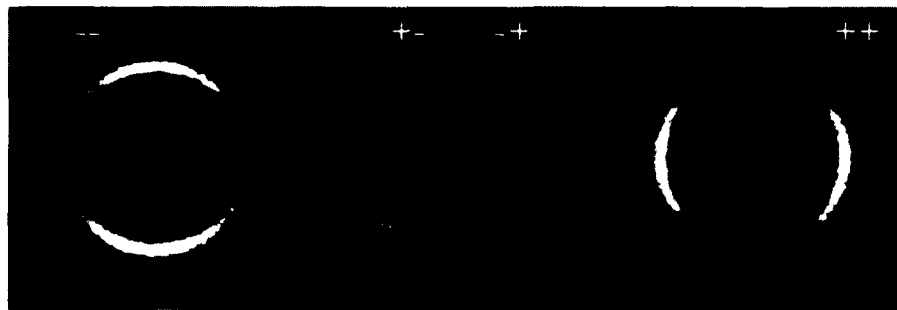


Figure 3.8: The four, polarization corrected cross sections recorded at 1.2 T and 200 K. (Reproduced from Ref. 34).

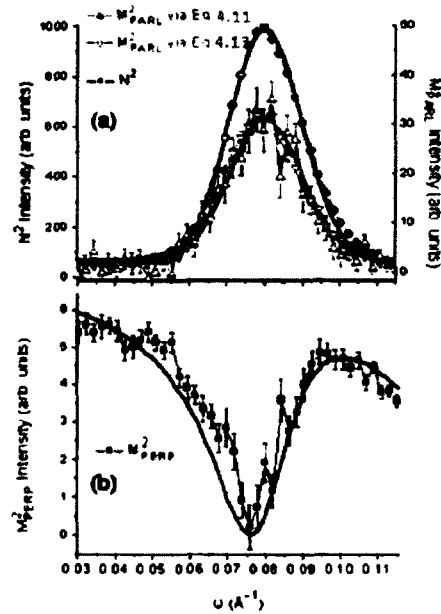


Figure 3.9: a) Nuclear and parallel magnetic scattering profiles at 1.2 T and 200 K. The data were scaled so that the nuclear peak had a value of 1000. Notice the large difference between the magnitude of the parallel scattering (right axis) and the nuclear scattering (left axis). The parallel magnetic scattering is presented as calculated using Eq. 3.11 and Eq. 3.13 in order to show their equivalence. The blue and purple fit lines are associated with the model given in Figure 3.8 b) The perpendicular magnetic scattering shows a prominent dip at about 0.075 \AA^{-1} . The green line shown is associated with the model given in Figure 3.8. (Reproduced from Ref. 34).

The large difference in the magnitude of the nuclear and magnetic scattering is the result of the large difference in the scattering length densities of $\rho_N = 6.97 \times 10^{-6} \text{ \AA}^{-2}$ and $\rho_N = 1.46 \times 10^{-6} \text{ \AA}^{-2}$ ³⁴. As discussed earlier, the scattering profile results from a combination of the structure factor which is due to the nanoparticle packing, and the form factor which is due to the internal structure of the nanoparticles. Here, the structure factor comes from the FCC packing of the nanoparticle crystallites³² with a lattice length of 13.6 nm. The crystals were confirmed to retain long-range FCC ordering up to hundreds of nanometers using TEM as shown in Figure 3.10.

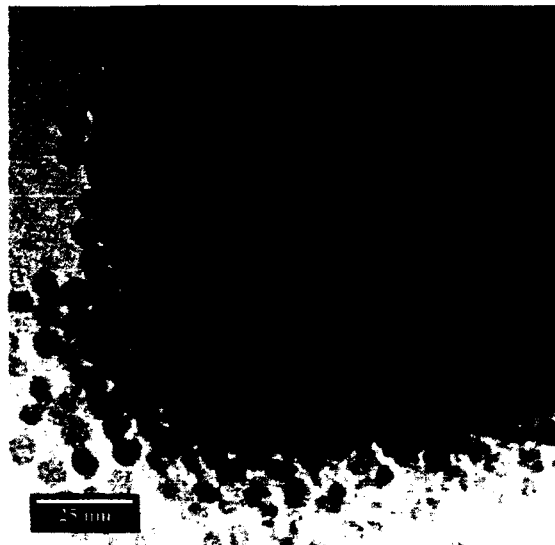


Figure 3.10: Transmission electron microscope (TEM) image showing part of a nanoparticle crystallite made up of FCC packed 9 nm iron oxide nanoparticles.

Within the Q range of 0.030 \AA^{-1} to 0.115 \AA^{-1} we measured there are two FCC Bragg reflections. The (111) and (200) reflections overlap to the extent that they appear as a single peak. With the introduction of stacking faults that are inevitable in the formation of nanoparticle crystals the position of the peak becomes strongly weighted towards the (111) reflection located at 0.080 \AA^{-1} . This structure factor convoluted with the form factor for 7.4 nm hard spheres results in the purple fit to the parallel magnetic scattering

in Figure 3.9. The convolution of the FCC structure factor and a 9.0 nm spherical form factor result in the blue fit to the nuclear scattering profile. The form of the spherical form factor is

$$\langle |F(Q, R)|^2 \rangle = 9 \left[\frac{\sin(QR) - QR \cos(QR)}{(QR)^3} \right]^2. \quad (3.20)$$

Form factors can only be solved analytically for systems of spherical symmetry. Instrumental broadening due mainly to a ~15% spread in the neutron wavelengths was included in the fit calculations.³⁴ The calculated structure factors are shown in Figure 3.11a. The large discrepancy between the parallel/nuclear structure factor and the perpendicular structure factor is due to a much shorter magnetic correlation length in perpendicular direction.

The use of the 7.4 nm spherical form factor for the fitting of the parallel magnetic scattering was necessitated by the parameters needed to fit the dip in the perpendicular magnetic scattering. The presence of a strong dip in the perpendicular scattering implies the scattering profile is dominated by the form factor rather than the structure factor and a dip is a well known feature of spherical form factors.³³

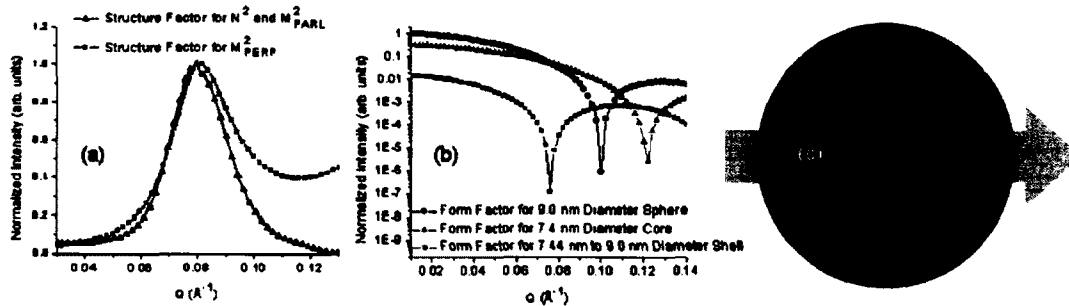


Figure 3.11: a) N^2 , M^2_{PARL} (black triangles and pink curve), and M^2_{PERP} (green curve) structure factors including instrumental broadening. b) Spherical form factors calculated for several structures showing the strong sensitivity of the dip position to the structure. The structure factors in a) and form factors in b) were convoluted to produce the fits shown in Figure 4.9. c) A composite model is depicted containing a 7.4 nm magnetic core and a coherently perpendicular magnetic shell with a thickness between 0.8 and 1.2 nm. (Reproduced from Ref. 34).

In order for the 0.075\AA^{-1} dip to fit a hard sphere model with coherently aligned spins throughout the particle, the particles would have to be 12 nm in diameter which is unphysically large. Rather, modeling the perpendicular form factor as a spherical shell with an average diameter of 8.22 ± 0.02 nm, inner diameter of 7.44 nm, and outer diameter of 9.0 nm gives a physically reasonable fit. This form factor combined with the structure factor from Figure 3.9a results in the green fit shown in Figure 3.7b and agrees well with the data. The shell thickness was further refined by taking into account the relative intensity of N^2 compared with M^2_{PERP} and applying the following additional constraints: i) the shell must reside within a 13.6 nm FCC lattice with a nearest neighbor

spacing of 9.6 nm measured from the particle centers, ii) there must be at least 0.1 nm of surfactant beyond the particle surface, and iii) while it is possible that the magnetic scattering length density is increased due to uncompensated surface spins, it is not allowed to deviate from the bulk value by more than a factor of two. The combination of these constraints gives a magnetic shell thickness of $1.0 \text{ nm} \pm .2 \text{ nm}$.³⁴

The evolution of the magnetic shell thickness as a function of temperature was investigated as shown in Figure 3.12. After zero-field cooling the sample to 10 K before the application of a 1.2 T field the perpendicular magnetic scattering due to the shell structure vanished completely. This does not eliminate the possibility that a magnetically disordered shell exists.

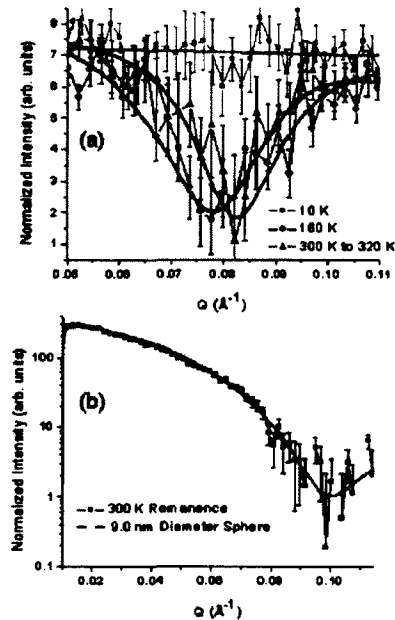


Figure 3.12: a) Temperature dependence of M^2_{PERP} . The temperature was varied in an applied field of 1.2 T and shows the presence of canted magnetic shells at 160, 300, and 320 K, but no ordered shell was found after zero-field cooling to 10 K before the application of a the 1.2 T field. b) At 300 K in a remanent field of 0.005 T, $M^2_{\text{PERP}} = M^2_{\text{PARL}}$ and fits the modeled scattering from a 9.0 nm sphere lacking a distinct shell. (Reproduced from Ref. 34).

After increasing the temperature to 160, the signature dip in M^2_{PERP} returns at nearly the same location as the dip at 200 K. Further increasing the temperature to 300 or 320 K (the data was similar enough to be averaged) shifts the dip to a higher Q value of 0.082 \AA^{-1} . Assuming the outer diameter of the particles remains fixed, this gives shell thicknesses of 1.0 nm and 1.5 nm at temperatures of 160 K and 300-320 K, respectively. The fits to this model are shown as the solid lines in Figure 3.10a.³⁴

Finally, to confirm that the shell is magnetic in nature and not chemical (i.e. a maghemite shell on a magnetite core), data was collected in a remanent field of 0.005 G

and a temperature of 300 K. Indeed, M^2_{PERP} was identical to M^2_{PARL} under these conditions and fit a 9.0 ± 2 nm solid sphere model extremely well as shown in Figure 3.10b. This, along with the disappearance of the shell at 10 K, and its increasing thickness as a function of temperature points to a shell that is entirely magnetic in its origins.

3.7 CONCLUSIONS

We believe this work to be the first measurement of the intraparticle surface spin structure for magnetic nanoparticles of any material. We concluded that between temperatures of 160 and 320 K under a nominally saturating field of 1.2 T a distinct shell 1.0 to 1.5 nm thick exists with a magnetization coherently ordered perpendicular to the applied field and the nanoparticle core.³⁴ This result provides strong evidence to refute many proposed spin configurations including a magnetically dead surface layer or spin-glass like structures.^{35,36,37,38} The addition of surface anisotropy terms to materials with uniaxial anisotropy in the bulk form greatly complicates the energy landscape³⁹ and has lead to the calculation of complicated surface structures such as the “hedgehog” configuration in which all spins point normally outward from the surface^{40,41,42,43}, the “artichoke” structure where spins are parallel to the surface and directed from one pole to the other,⁴² and the “throttled” structure where spins are tilted slightly inward at the south pole and slightly outward at the north pole.⁴² In addition to these there is a large range of more complicated spin configurations⁴ that have been modeled or predicted in the past. Despite the wide range of predictions this work is the first to directly measure intraparticle magnetic spin structure.

The shell canting is likely due to the surface anisotropy of the magnetic nanoparticles as proposed previously^{41,42} and the coherent alignment of the shell spins over the length of several particles comes from interparticle interactions. The competition of these two interactions likely leads to the absence in radial symmetry as might be naively expected.¹⁷ The discovery of such a complex intraparticle structure emphasizes the importance of understanding the nature of magnetic interactions in these samples and significantly limits the cases in which magnetic nanoparticles can be treated as having one coherent spin. Additionally, the coherent perpendicular ordering over many nanoparticles provides a viable physical origin for the transverse magnetic moments measured in the previous chapter using DC SQUID magnetometry, though the measurements are not equivalent.

When considered separately from the discovery of this very interesting intraparticle spin structure, the development of the PASANS setup and analysis formalism as a very important tool for probing magnetic structure on intraparticle length scales cannot be overestimated. We hope in the future to build on the PASANS technique and elucidate other often modeled, but never before measured spin structures like those proposed at the interface of the AFM and FM layers exchange biased nanoparticle systems like MnO/Mn₃O₄. Although some methods like transmission electron microscopy using electrons with orbital angular momentum⁴⁴ that could in theory probe similar spin structures are currently being developed, PASANS is the only current technique able to probe local spin structures.

3.8 REFERENCES

-
- ¹ S. Sun, H. Zeng, D. B. Robinson, S. Raoux, P. M. Rice, S. X. Wang, and G. X. Li, *J. Am. Chem. Soc.* 126 (2004) 273.
 - ² Q. A. Pankhurst, J. Connolly, S. K. Jones, and J. Dobson, *J. Phys. D: Appl. Phys.* 36 (2003), R167-R181.
 - ³ C. A. Ross, *Annu. Rev. Mater. Res.* 31 (2001), 203-235.
 - ⁴ R. A. Kodama and A. E. Berkowitz, *Phys. Rev. B* 59 (1999), 6321.
 - ⁵ K. L. Krycka, J. A. Borchers, R. A. Booth, C. R. Hogg, Y. Ijiri, W. C. Chen, S. M. Watson, M. Laver, T. R. Gentile, S. Harris, L. R. Dedon, J. J. Rhyne, and S. A. Majetich, *J. Appl. Phys.* 107 (2010), 09B525.
 - ⁶ W. Knoll, K. Ibel, and E. Sackmann, *Biochemistry* 20 (1981), 6379-6383.
 - ⁷ Scattering Length Density Calculator,
<http://www.ncnr.nist.gov/resources/sldcalc.html>.
 - ⁸ “Chapter 13 – Neutron Area Detectors,”
http://www.ncnr.nist.gov/staff/hammouda/distance_learning/chapter_13.pdf
 - ⁹ Y. Ijiri, C. V. Kelly, J. A. Borchers, J. J. Rhyne, D. F. Farrell, and S. A. Majetich, *Appl. Phys. Lett.* 86 (2006), 243102.
 - ¹⁰ A. Michels, J. Weissmuller, *Rep. Progr. Phys.* 71 (2008), 066501.
 - ¹¹ C. D. Clark, E. W. J. Mitchell, D. W. Palmer, and I. H. Wilson, *J. Sci. Instrum.* 43 (1966), 1.
 - ¹² NG3 SANS Instrument Information, <http://www.nist.gov/ncnr/ng3-sans-small-angle-neutron-scattering.cfm>.
 - ¹³ V. F. Turchin, Deposited Paper, *At. Energy* 22 (1967).
 - ¹⁴ F. Mezei, “Novel polarized neutron devices: supermirror and spin component amplifier,” *Communications on Physics* 1 (1976).
 - ¹⁵ F. Mezei and P. A. Dagleish, “Corrigendum and first experimental evidence on neutron supermirror,” *Communications on Physics* 2 (1977).
 - ¹⁶ P. Böni, *Physica B*, 234-236 (1997), 1038-1043.
 - ¹⁷ K. L. Krycka, R. A. Booth, J. A. Borchers, W. C. Chen, C. Conlon, T. R. Gentile, C. Hogg, Y. Ijiri, M. Laver, B. B. Maranville, S. A. Majetich, J. J. Rhyne, and S. M. Watson, *Physica B* 404 (2009) 2561-2564.
 - ¹⁸ T. R. Gentile, G. L. Jones, A. K. Thompson, J. Barker, C. J. Glinka, B. Hammouda, J. W. Lynn, *J. Appl. Crystallogr.* 33 (2000), 771.
 - ¹⁹ A. Wiedenmann, *Physica (Amsterdam)* 356B (2005) 246.
 - ²⁰ A. M. Gaspar S. Busch, M. S. Appavou, W. Haeussler, R. Georgii, Y. X. Su, and W. Doster, *Biochim. Biophys. Acta* 1804 (2010), 76.
 - ²¹ W. G. Williams, *Polarized Neutrons*. New York: Oxford (1988).
 - ²² W. C. Chen, R. Erwin, J. W. McIver, S. Watson, C. B. Fu, T. R. Gentile, J. A. Borchers, J. W. Lynn, G. L. Jones, *Physica (Amsterdam)* 404B (2009), 2663.
 - ²³ W. C. Chen, T. R. Gentile, K. V. O’Donovan, J. A. Borchers, and C. F. Majkrzak, *Rev. Sci. Instrum.* 75 (2004), 3256.
 - ²⁴ C. B. Fu, T. R. Gentile, G. L. Jones, W. C. Chen, R. Erwin, S. Watson, C. Broholm, J. A. Rodriguez-Rivera, and J. Scherschlight, *Physica B* 407 (2011), 2419-2423.
 - ²⁵ F. D. Colegrove, L. D. Schearer, and G. K. Walters, *Phys. Rev.* 132 (1963), 2561.

-
- ²⁶ J. Becker, W. Heil, B. Krug, M. Leduc, M. Meyerhoff, P. J. Nacher, E. W. Otten, T. Prokscha, L. D. Schearer, and R. Surkau, *Nucl. Instr. And Meth. in Phys. Res. A* 346 (1994), 45-51.
- ²⁷ T. G. Walker and W. Happer, *Rev. Mod. Phys.* 69 (1997), 629.
- ²⁸ B. Chann, E. Babcock, L. W. Anderson, T. G. Walker, W. C. Chen, T. B. Smith, A. K. Thompson, and T. R. Gentile, *J. Appl. Phys.* 94 (2003), 6908.
- ²⁹ R. M. Moon and T. Riste, and W. C. Koehler, *Phys. Rev.* 181 (1969), 181.
- ³⁰ K. Krycka, W. Chen, J. Borchers, B. Maranville, and S. Watson, *J. Appl. Cryst.* 45 (2012), 546-553.
- ³¹ K. Krycka, J. Borchers, Y. Ijiri, R. Booth, and S. Majetich, *J. Appl. Cryst.* 45 (2012), 554-565.
- ³² D. A. Farrell, Y. Ijiri, C. V. Kelly, J. A. Borchers, J. J. Rhyne, Y. Ding, S. A. Majetich, *J. Magn. Magn. Mater.* 303 (2006), 318.
- ³³ A. Guinier, *X-Ray Diffraction in Crystals, Imperfect Crystals, and Amorphous Bodies* (Dover, New York, 1994).
- ³⁴ K. L. Krycka, R. A. Booth, C. R. Hogg, Y. Ijiri, J. A. Borchers, W. C. Chen, S. M. Watson, M. Laver, T. R. Gentile, L. R. Dedon, S. Harris, J. J. Rhyne, and S. A. Majetich, *Phys. Rev. Lett.* 104 (2010) 207203.
- ³⁵ P. Dutta, S. Pai, M. S. Seehra, N. Shah, G. P. Huffman, *J. Appl. Phys.* 105 (2009), 07B501.
- ³⁶ J. Curiale, Granada, H. E. Troiani, R. D. Sanchez, A. G. Leyva, P. Levy, K. Samwer, *Appl. Phys. Lett.* 95 (2009), 043106.
- ³⁷ A. Kovacs, K. Sato, V. K. Lazarov, P. L. Galindo, T. J. Konno, Y. Hirotsu, *Phys. Rev. Lett.* 103 (2009), 115703.
- ³⁸ C. Westman, S. Jang, C. Kim, S. He, G. Harmon, N. Miller, B. Graves, N. Poudyal, R. Sabirianov, H. Zeng, M. DeMarco, J. P Liu, *J. Phys. D* 41 (2008), 225003.
- ³⁹ R. Yanes, O. Chubykalo-Fesenko, H. Kachkachi, D. A. Garanin, R. Evans, R. W. Chantrell, *Phys. Rev. B* 76 (2007) 064416.
- ⁴⁰ J. Mazo-Zuluaga, J. Restrepo, and J. Majía-López, *Physica (Amsterdam)* 398B (2007), 187.
- ⁴¹ J. Mazo-Zuluaga, J. Restrepo, F. Munoz, J. Mejia-Lopez, *J. Appl. Phys.* 105 (2009), 123907.
- ⁴² L. Berger, Y. Labaye, M. Tamine, and J. M. D. Coey, *Phys. Rev. B* 77 (2008), 104431.
- ⁴³ Y. Hu and A. Du, *J Nanosci. Nanotechnol.* 9 (2009), 5829.
- ⁴⁴ B. J. McMorran, A. Agrawal, I. M. Anderson, A. A. Herzing, H. J. Lezec, J. J. McClelland, and J. Unguris, *Science* 331 (2011), 192-195.

Chapter 4

Synthesis and Characterization of Highly Monodisperse, Single Crystal MnO|Mn₃O₄ Nanoparticles with Variable Shell Thickness

4.1 INTRODUCTION

As discussed in the previous chapters, recent advances in nanoparticle synthesis, control, characterization, and assembly techniques have lead to exciting and diverse scientific advances over the last half century. Meiklejohn and Bean's discovery of exchange bias in cobalt-core, cobalt oxide-shell nanoparticles in 1956 was one such disruptive innovation with widespread implications.¹ The empirical understanding of exchange bias eventually lead to the development of synthetic antiferromagnets, the discovery of giant magnetoresistance (GMR)—which lead to a Nobel prize in 2007 for Fert and Grünberg²—and early developments in the rapidly growing field of spintronics. GMR sensors have been used extensively in magnetic hard drives, and have been critical in allowing data storage densities to grow at the amazing rates we've witnessed over the last several decades.³ Curiously, even with the widespread use technologies based on exchange bias, details of the physics involved are still elusive. As an interface phenomenon acting over length scales of only a few angstroms it is inherently hard to study. Basic research in exchange biased thin films and nanoparticle structures continues to be one of the most fruitful avenues of investigation.

Research on thin film-based, exchange biased structures has several advantages. Thin film devices can be created with a wide range of film thicknesses, from a wide range of materials, and technological advances can be developed into consumer products following well established pathways. Many characteristics of thin film structures can also be easily characterized using traditional magnetometry and x-ray techniques. Despite these advantages of the thin film approach, a detailed, comprehensive understanding of the microscopic magnetic origins of exchange bias has been elusive for the 56 years since its discovery.

In this chapter, we focus on understanding exchange bias in the MnO|Mn₃O₄ core/shell nanoparticle system. While involved, nanoparticle synthesis facilities can be developed and maintained at a small fraction of the cost of thin film deposition facilities. Additionally, for the study of the interface between two materials, nanoparticles maximize the volume of interest. In a composite of many core/shell nanoparticles, the interfacial area scales with the sample volume rather than the sample area as in thin film materials. This provides a significant boost in the available signal for many techniques. Although not presented here, we hope in the future to use PASANS and the increased magnetic scattering intensity at nanoparticle crystal Bragg peaks to investigate the ordering of interfacial spins in the MnO|Mn₃O₄ structure under a variety of conditions.

In the following chapter we will discuss a novel chemical synthesis and the magnetic characterization of the MnO|Mn₃O₄ exchange biased nanoparticle system. Additionally, anomalies between the existing literature and our experiments will be presented and explanations will be proposed.

4.1.1 EXCHANGE BIAS IN NANOPARTICLE SYSTEMS

The most naturally accessible nanoparticle systems for the early study of exchange bias were ferromagnetic transition metals and their native antiferromagnetic oxides. Throughout this chapter, the notation core-material|shell-material will be used for simplicity in describing these structures. Some examples of the nanoparticle exchange biased systems studied are the transition metal core / native oxide shell systems like Co|CoO,^{4,5} Ni|NiO,⁶ (Co,Ni)|(Co,Ni)O,⁷ Fe|Fe_xO_y,⁸ and Mn|Mn_xO_y.⁹ Additionally, oxide / oxide systems like CrO₂|Cr₂O₃,^{10,11} and Fe₃O₄|\(\alpha\)-Fe₂O₃ and Fe₃O₄|FeO.^{12,13} Exchange bias like behavior has even been observed in oxide / protein systems of Fe_{3-x}Co_xO₄|ferritin¹⁴ although the nature of the AFM in this structure was not explained. Here we build on a growing body of work on the MnO|Mn₃O₄ system^{15,16,17,44} with the development of a highly monodisperse synthesis of single crystal MnO particles and the creation of an epitaxial Mn₃O₄ shell of controllable thickness.

4.1.2 THE MnO|Mn₃O₄ SYSTEM

The MnO|Mn₃O₄ system is unique for several reasons. Magnetically, it is considered a doubly inverted system because AFM|FiM structure is opposite of the FM|AFM structure more typical of the exchange biased nanoparticle systems and at 42 K the Curie temperature of Mn₃O₄¹⁸ is lower than the 122 K Ne l temperature of MnO.¹⁹ Typically the Ne l temperature is lower than the Curie temperature. This is especially true for the transition metal / native oxide systems.

Structurally, the manganese oxide system is unique because there is epitaxial registry at the interface of the MnO and Mn₃O₄.²⁰ Both the core and the shell are single crystals. This greatly simplifies the application of theoretical models to experimental measurements of exchange bias in the MnO|Mn₃O₄ system. In the following chapter we

discuss the synthesis, controlled oxidation, self-assembly, microscopic, and magnetic characterization of $\text{MnO}|\text{Mn}_3\text{O}_4$ core-shell nanoparticles.

4.2 EXPERIMENTAL

The synthesis of the manganese oxide nanoparticles was carried out using Schlenk line techniques and argon gas for the inert environment. All magnetic measurements were made using a Quantum Design MPMS SQUID magnetometer. Transmission electron microscope (TEM) images were taken using a JEOL 2000x operated at 200 kV.

4.2.1 SYNTHESIS

In a typical reaction, 15 mL trioctylamine, 12 mmol (3 g) oleic acid (OA), and 4 mmol (0.6921 g) manganese acetate were combined. This mixture was thoroughly degassed by alternating vacuum and argon gas at room temperature. The degassed mixture was then dried by heating to 70 °C under vacuum of 100 millitorr and stirring for 1 hour. Complete removal of water from the solution is necessary in order to obtain spherical particles. Figure 4.1a shows nanocrosses obtained from a preparation in which no drying step was used. This morphology was investigated in detail previously by very carefully controlling the amount of water present in each synthesis.²¹ More recently, An *et al.* did a thorough investigation of the effects of different coordinating solvents and surfactants on the morphology of MnO nanoparticles produced from a manganese oleate precursor and found a wide range of accessible shapes and sizes.²² The mixture was then heated under argon gas flow at a 35°C/min to 350 °C. This rapid heating rate was achieved by setting the control temperature on the temperature controller to 500 °C to ensure the mantle was being powered at 100% duty cycle during the ramp. After the temperature of the reaction had reached 335 °C, the control temperature was set to 335 °C. The ramp setting on the temperature controller was set to its maximum value. The temperature of the reaction as a function of time is shown in Figure 4.2.

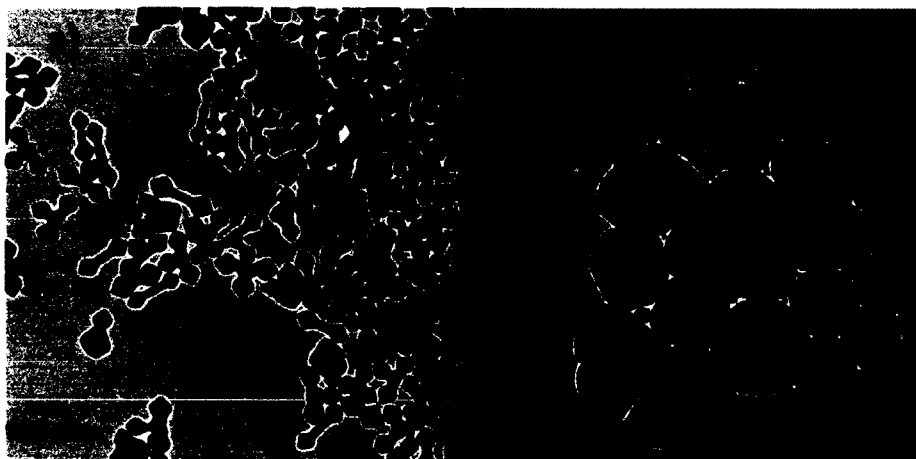


Figure 4.1: a) nanocross morphology caused by the presence a very small amount of water and b) micron sized particles caused by the condensation of acetone into the solution.

By 100 °C, the acetate was fully dissolved and the solution appeared a clear light-pink color. By 200 °C, the solution was clear and colorless. During the heating process it is critical to keep all surfaces of the reaction vessel above 60 °C using a heat gun, and the argon flow arranged in such a way that the acetone product does not condense back into the solution and affect the solubility of the OA. For this reason, it is also important not to use a reflux tube. If acetone is allowed to condense into the solution, irregular micron sized particles are produced as shown in Figure 4.1b. Following the acetate decomposition route proposed by Arii *et al.* about 4.3 mmol (0.3 mL) of acetone is produced and must be properly removed while heating.²³

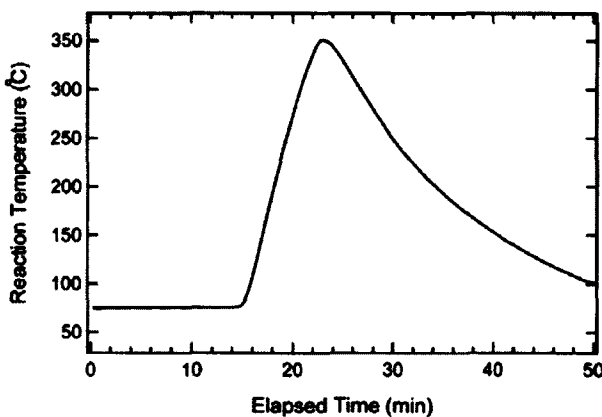


Figure 4.2: Temperature of the reaction as a function of time. The last 15 minutes of the drying cycle, the fast ramping to 350 °C, and the cooling can be seen clearly.

Nucleation of the MnO nanoparticles begins very quickly after the maximum temperature is reached. The color change proceeded from clear, to yellow, to dark yellow, to light brown over about 30 seconds before abruptly changing to a milky green color. The evolution of the color change is shown in Figure 4.3.

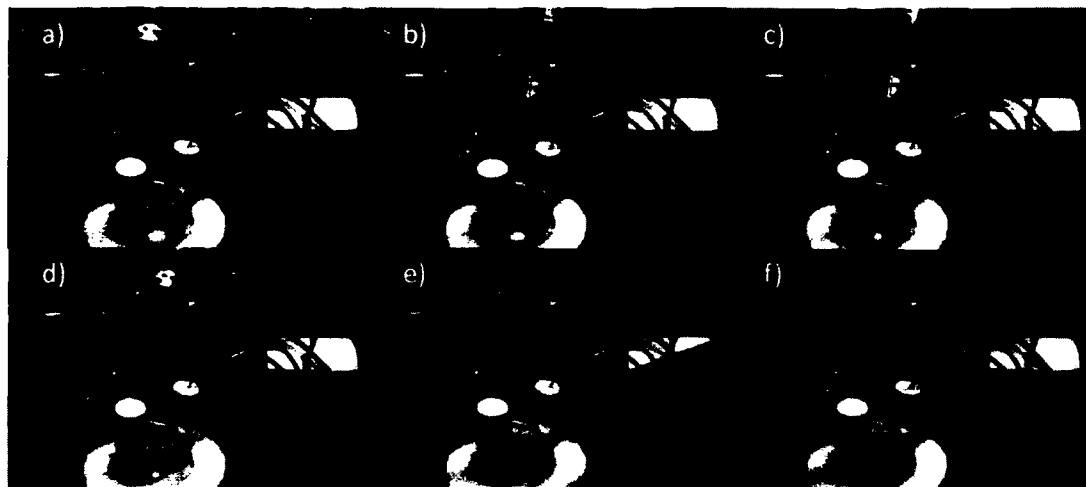


Figure 4.3: Reaction vessel at a) about 200 °C after precursor had dissolved completely, b) beginning to turn clear yellow, c) turning brownish-yellow, d) turning to a white milky-green, e) turning to a deeper milky green, f) synthesis is complete with a deep milky-green. The total time shown in the figure is about 3 minutes.

The solution was then cooled slowly to room temperature by turning off the heater but leaving the flask on the heating mantle, over which time it cleared and darkened to a deeper, translucent green. The particles were washed with ethanol and precipitated by centrifugation in oxygen-free conditions. The supernatant was discarded and the retentate was redispersed in 15 mL of toluene and 50 μ L of OA, and then sonicated for 5 minutes. The resulting particles are well-dispersed and remain stable in solution indefinitely. The particle diameters varied slightly in size from 25-30 nm between syntheses, but were extremely monodisperse. A similar preparation published by Yin and O'Brien²⁴ suggests that the particles can be grown by a post-nucleation annealing step at 100 °C, but we were not able to reproduce their results. The final solution is a translucent green color if the particles are washed in oxygen-free conditions and remain MnO.

In order to wash the particles in oxygen-free conditions, the reaction flask partially evacuated, sealed with glass stoppers, removed from the Schlenk line, and transferred into the argon filled glovebox. It is important to partially evacuate the flask before passing it through the airlock into the glovebox to reduce forces on the flask due to the pressure difference when the airlock is evacuated. Likewise, it is advisable to use solid glass stoppers instead of hollow glass stoppers. Degassed ethanol is used to wash the particles and they are passed to out of the glovebox to the centrifuge in sealed plastic centrifuge tubes. If the native Mn₃O₄ oxide is allowed to form by exposing the solution to air the solution appears dark brown but still remains colloidally stable indefinitely. The color difference between the two phases is very obvious as shown in Figure 4.4.

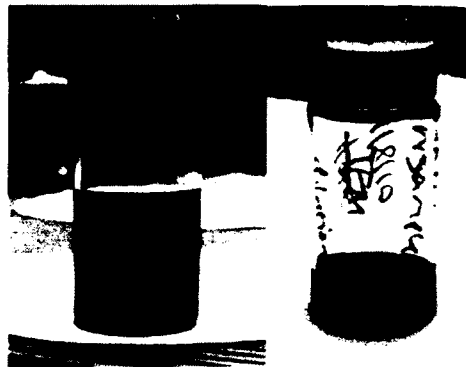


Figure 4.4: Photographs of manganese oxide nanoparticle suspensions showing a) the green color of MnO and b) the brown color of Mn₃O₄.

4.2.2 Mn₃O₄ SHELL FORMATION

If oxygen-free conditions are maintained during the washing step and the particles are stored in an inert atmosphere, they remain entirely MnO which has a cubic rock salt structure with a lattice parameter of $a=4.44 \text{ \AA}$ and is green in color.²⁵ If the particles are exposed to air a thin poorly crystalline layer of Mn₃O₄ is quickly formed. This oxidation is accompanied by a rapid color change from green to brown. It has been confirmed that this gentle, room temperature oxidation forms the spinel phase of Mn₃O₄²⁶ with lattice parameters of $a=5.75 \text{ \AA}$ and $c=9.42 \text{ \AA}$.²⁷

Particles oxidized by exposing the solution to air and sonicating for 5 minutes at room temperature are shown in Figure 4.5a. The contrast between the core and shell of the particles observed in the bright field transmission electron microscope (TEM) images is not dominated by a difference in electron density, but rather the particles are oriented such that non-overlapping zone axes of MnO and Mn₃O₄ were distinctly separated. Notice that the shell is about 2-3 nm thick, but poorly crystalline, as shown by the mottled Bragg contrast at the shell.

The crystallinity and thickness of the Mn₃O₄ shell can be increased by oxidizing the particles at higher temperature. For this, yet unoxidized particles were dispersed in 15 mL of trioctylamine and the toluene was evaporated by heating the solution to 100 °C while maintaining oxygen free conditions. Trioctylamine was chosen because it is a readily available high boiling point (b.p. 366 °C) solvent that maintains a stable dispersion of oleic acid coated particles. Trioctylamine, [CH₃(CH₂)₇]₃N, is useful as a solvent for annealing the MnO particles in oxygen free conditions as it contains no oxygen. Prior to oxidation at 100 °C, the particles were annealed in oxygen free conditions at 300 °C for 3 hours. The temperature was then reduced to 100 °C and the solution was oxidized by bubbling with air while stirring. After stirring for 3 hours the particles have a well defined 3.5 - 4.5 nm shell as shown if Figure 4.5b. Stirring for 80 hours increased the shell thickness to 4.0-6.0 nm as shown in Figure 4.5c.



Figure 4.5: a) particles oxidized at room temperature, and by bubbling air into particles suspended in trioctylamine at 100 °C for b) 3 hours and c) 80 hours.

High resolution (HR-TEM) images were also recorded using a Technai F20 Field Emission TEM. At high resolution the difference in the lattice fringes between the two phases is clearly visible as shown in Figure 4.6. Lattice fringe spacing can be used to verify structure, but the approach is imperfect in nanoparticle systems because the spacing is highly susceptible to strain. It is, however, indicative of the overall particle crystallinity.

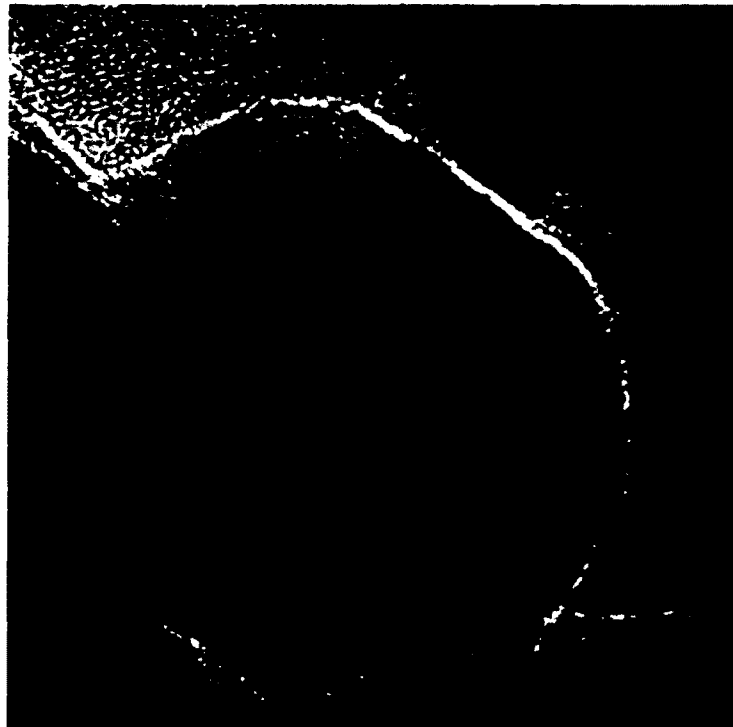


Figure 4.6: High resolution TEM image of $\text{MnO}|\text{Mn}_3\text{O}_4$ nanoparticle showing contrast variation between the core and shell due to Bragg

orientation, and a lattice spacing variation between the core and shell. The parallel orientation of the lattice fringes for the core and the shell are evidence of the epitaxial registry. (Courtesy of Yoosuf Picard).

4.2.3 MAGNETIC MEASURMENTS

Since MnO is antiferromagnetic below a Néel temperature of 122 K and Mn₃O₄ is ferrimagnetic below a Curie temperature of 42 K, exchange bias between the two phases can be observed below 42 K. Exchange bias is manifest in large coercive (H_c) and exchange fields (H_{ex}) of hysteresis loops measured after field cooling through the Curie and Néel temperatures of the material. The coercive field is the field required to reduce the magnetic moment of a material to zero, because of the shift of the hysteresis loop due to the exchange bias, the coercive field is more easily reported as half of the width of the hysteresis loop of the sample. The exchange field is defined as the shift of the center of the hysteresis loop. Both H_c and H_{ex} are schematically illustrated in Chapter 1. In this case, all measurements were made after field cooling the particles at a rate of 10 K/min from at least 250 K in a 50 kOe field to 10 K. Samples were made by precipitating particles from solution using ethanol and evaporating the solvents. No effort was made to fully remove the surfactant coating so neighboring particles are separated from each other by 2-3 nm. Both H_c and H_{ex} increase with increasing shell thickness and oxidation time as shown in Figure 4.7. H_c was measured to be 85, 865, 2075, and 4550 Oe for the unoxidized, 3 hours oxidized, 12 hours oxidized, and 80 hours oxidized respectively. H_{ex} for the same samples was measured to be 22, 585, 925, and 950 Oe respectively.

Note that we do not report the magnetization (emu/g), but rather report only the magnetic moment measured in our hysteresis loops. This is because we believe the sample mass cannot be accurately measured in these core shell samples due to compounding errors. For homogeneous particles—for instance 100% Fe₃O₄—in solution, the sample weight can be determined using methods discussed in Chapter 2. With a two-phase core/shell systematic error in the estimation of the core volume and shell volume would dominate the calculation. Directly weighing a sample also has significant error due to the large amount of surfactant typically present in these samples. While magnetization is typically presented in the literature for these core/shell samples, the method used to do the normalization is rarely presented, and these numbers should be considered with caution.

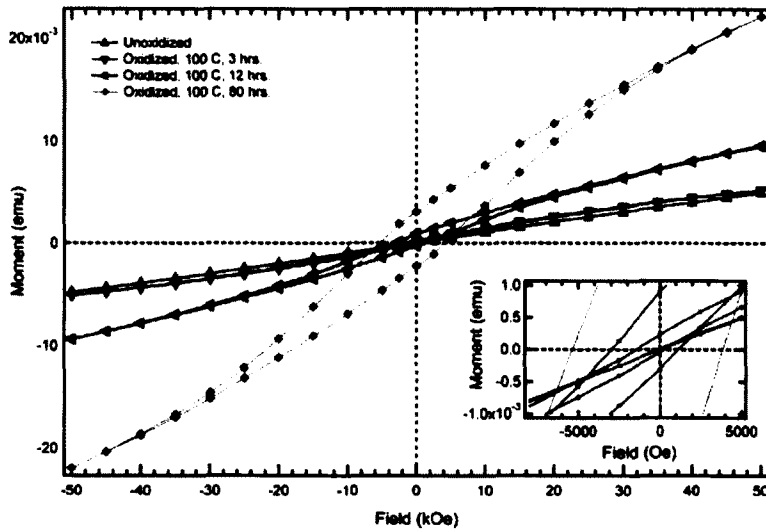


Figure 4.7: Hysteresis loops of unoxidized MnO particles and oxidized MnO|Mn₃O₄ particles of varying oxidation times and shell thicknesses recorded after field cooling in a 55 kOe field from 250 K to 10 K. Inset shows detail at the zero crossing.

The evolutions of the coercive and exchange fields as a function of increasing oxidation time are shown in Figure 4.8. As expected, the coercive and exchange field are very small for the unoxidized particles. Most of the observed magnetism comes from uncompensated AFM spins and the particles behave very similar to a paramagnet. In reality, what appears to be exchange bias in these particles could with equal likelihood be irreversibility due to crystallographic surface disorder because the unoxidized particles have not been annealed. In the exchange biased nanoparticle literature this possibility is often overlooked and will be discussed in more detail in Section 4.3. The sharp increase in both values after three hours of oxidation can be attributed to the onset of exchange bias after the creation of the Mn₃O₄ shell and thus the FIM/AFM interface. It is reasonable that after this the exchange field should not increase significantly as a function of shell thickness as it depends mostly on the interface. The coercive field continues to increase dramatically as a function of oxidation time.

As the particles are annealed, they are expected to become magnetically harder as defects that would allow domain nucleation at lower applied fields are removed from the crystal structure. Naively, one would not expect any benefit from heat treating the MnO nanoparticles at 300 °C. The fact that the useful annealing temperature is much lower in nanoparticles than in bulk alloys is partly due to finite size effects. Since nanoparticles are composed of at most a few thousand atoms, the distance that defects have to diffuse to be removed from the crystal structure is much smaller than bulk materials. Additionally, the defects in nanoparticles prepared by the high temperature decomposition of organic solvents are mainly dislocations and carbon inclusions.²⁸ Because they are lighter elements, the carbon inclusions will be mobile at a lower temperature.

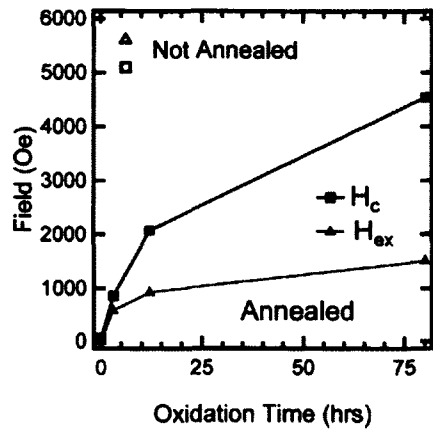


Figure 4.8: Coercive and exchange fields as a function of oxidation time for MnO nanoparticles. Notice the large discrepancy between particles that were and were not annealed. Error in the measured field is on the order of 50 Oe, error in the oxidation time is on the order of 0.25 hours.

For comparison to the annealed particles, similar particles were oxidized for 6 hours by bubbling air in a trioctylamine solution at 300 °C. H_{ex} and H_c were 5600 Oe and 5100 Oe, respectively for these particles. The values were much higher for the unannealed particles than the annealed particles. The TEM image in Figure 4.9 shows a 2-3 nm shell on the unannealed particles of comparable thickness to sample oxidized for 3 hours at 100 °C shown in Figure 4.6b, therefore the higher values cannot be attributed to a dramatically different shell thickness. There is, however, a noticeable difference in the Bragg contrast with the core of an individual particle compared to those in Figure 4.6b. This is indicative of a poorer crystallinity.

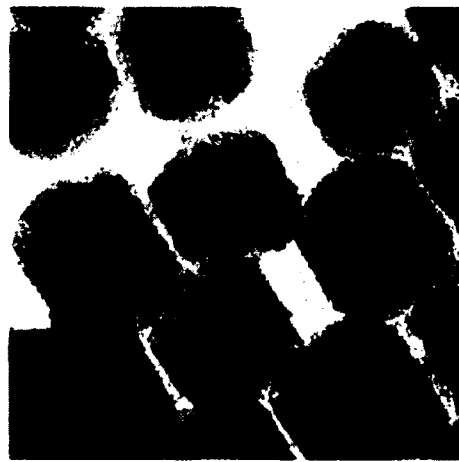


Figure 4.9: TEM image of particles oxidized at 300 °C for 6 hours. Notice the shell thickness of 2-3 nm is comparable to the sample shown in

Figure 4.6b, but the Bragg contrast in the core is much less uniform indicating poorer crystallinity.

To investigate the nature of this anomaly, a remanent hysteresis loop was measured as shown in Figure 4.10. A remanent hysteresis loop is measured by recording the magnetic moment and remanent moment for each applied field. The remanent state is accessed by setting the applied magnetic field to zero between consecutive measurements at a non-zero applied field.

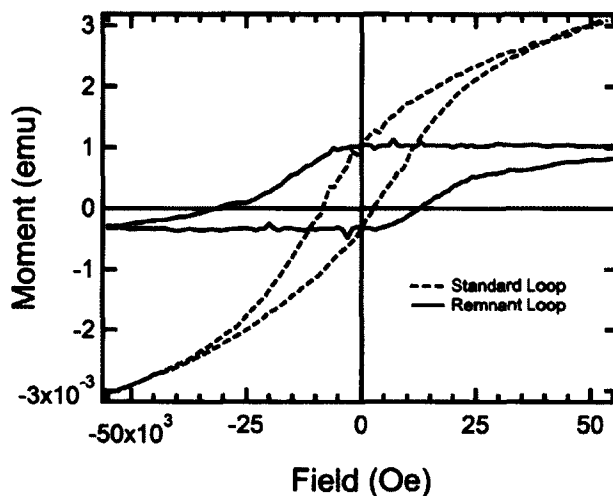


Figure 4.10: Remanent (blue) and standard hysteresis loop (green) for unannealed $\text{MnO}|\text{Mn}_3\text{O}_4$ particles in which the shell was formed by oxidizing the particles in solution for 6 hours at 300 °C.

The remanent loop is very useful in understanding the contribution from ferromagnetic and ferrimagnetic moments in the particles. Since ideal antiferromagnetic and paramagnetic systems do not have coercivity, they don't have a remanent moment and do not contribute to the remanent loop. Several features immediately stick out. First, there is a dramatic vertical shift in the position of the loop. A vertical shift like this is often attributed to thermal training which is distinct from athermal training.²⁹ Thermal training is most often characterized by a dramatic reduction in H_{ex} and H_c between the first and second hysteresis loops recorded on a sample. It is most likely the result of the complex energy landscape of the AFM in many exchange biased systems, and is due to energy minima other than the state set during the field-cooling process that are accessible through thermal fluctuations of the AFM spins. The accepted model for thermal training was described by Hoffman and attributes the complex energy landscape to a distribution of easy-axes within the AFM.³⁰ Because the thermal fluctuations that change the energy minimum of the system are stochastic in nature there is a time dependence to the behavior. This can be seen in the lack of agreement between the positive saturation values on the remanent loop in Figure 4.9 that developed over the several hours it took to

complete the measurement. AFM moments should not contribute to the remnant loop directly, but couple strongly to the FiM spins that do.

Another striking feature of the remanent loop is the existence of two distinctly different slopes in the approach to saturation. This clearly shows two different spin regimes: one that saturates at fields of about 25 kOe, and another that barely saturates by 55 kOe. This could be attributed to softer spin components in well ordered regions of the particle and harder spin components in the vicinity of vacancies and crystalline imperfections. Although it is likely a small effect in the measurement of a standard hysteresis loop, the vertical shift in the remnant loop clearly leads to very different values in the measured H_c and H_{ex} .

4.2.4 3D SELF ASSEMBLY

For many measurements, analyses, and applications, having structures with long range order simplifies the investigation of the building blocks of a material (*i.e.* atoms, proteins, polymers, or nanoparticles). For instance, self assembly induced crystallization DNA allowed for its structure to be determined using x-ray diffraction techniques long before it could be directly observed.³¹ Similarly, we have investigated methods to self assemble nanoparticles into crystals with long range order to facilitate the use of small angle neutron scattering (SANS) in understanding inter and intra-particle interactions of magnetic nanoparticle systems.

Previous work on 3D self-assembly of nanoparticles has focused on small < 10 nm particles. These methods proceeded in one of two ways. In the first case, nanoparticles were suspended in a solution initially consisting of a majority (~90%) low boiling point, stable solvent such as an alkane and a small amount (~10%) high boiling point, destabilizing alcohol.³² Because of the large difference in the evaporation rate between the alkane and the alcohol, the solution is slowly destabilized. If the destabilization proceeds slowly enough so that a particle can find its minimum energy position in an assembly before being pinned in a disordered state by the next particles to arrive, long range order and close packed colloidal crystals tens of microns in size can be formed. The second case is a variation on the first technique, but instead of destabilizing the solution by the differential evaporation of a solvent and a non-solvent, the non-solvent is allowed to slowly diffuse into a stable suspension of particles. For instance, a stable suspension of particles in an alkane is placed in the bottom third of a test tube, then a buffer layer of 2-propanol is carefully added so that it floats on the particle suspension, then an alcohol (ethanol or methanol) is added carefully so that it floats on the 2-propanol buffer.^{33,34} Over a period of months, the alcohol slowly diffuses through the buffer layer very slowly destabilizing the nanoparticles and allowing them ample time to find their minimum energy position.

While we have used these methods in the past to form large crystals with <10 nm particles in the past,³⁵ they did not successfully form colloidal crystals with long range order using the ~30 nm MnO particles described above when the experiment was carried out at room temperature. Large colloidal crystals were successfully formed at elevated temperature. Specifically, the MnO particles were precipitated from the toluene and redispersed in heptane at a concentration 5x less than the as-made concentration. Heptanol was added at 5% by volume as a destabilizing non-solvent. This mixture was

placed in test tubes that were suspended in an oil bath maintained at 70 °C until the solvent evaporated completely over approximately 2 days. High-resolution scanning electron microscopy (HR-SEM) of the resulting particles confirms highly ordered colloidal crystals of tens of microns in size were produced as shown in Figure 4.11. Disordered regions can be seen surrounding the larger crystallites. Careful optimization of temperature, solvent, and non-solvent along with a slower crystallization rate would likely improve the overall colloidal crystal yield.



Figure 4.11: HR-SEM micrographs showing colloidal crystals of MnO nanoparticles. The images show a) the large size and faceting of the crystallites, and b) the high degree of long range order.

Nanoparticles self-assemble into colloidal crystals because of the energy balance between the attractive van der Waals potential and the randomizing thermal energy mediated by the steric barrier provided by the particles' surfactant coating. If the van der Waals potential is much greater than the thermal energy, the particles will be immobilized as soon as they contact each other resulting in a glassy packing instead of the ordered packing achieved when the particles have enough thermal energy to find the lowest energy position in the crystal structure. The Hamaker constant, which mediates the van der Waals interaction, was recently calculated for iron oxide nanoparticles in their typical colloidal environments by Faure *et al*³⁶ and with the given values the van der Waals attraction is of the same order of magnitude as the thermal energy.

4.3 DISCUSSION

4.3.1 POSSIBLE ORIGINS OF ANOMALOUSLY HIGH H_{ex}

There are many discrepancies in the exchange biased core-shell magnetic nanoparticle literature due to the complicated synthetic chemistry, structural characterization, and the unresolved nature of the magnetism in such samples. One large

discrepancy between this work and the other recently published papers on MnO|Mn₃O₄ is the two order of magnitude difference in the H_{ex} and H_c of MnO with just the native oxide. Here I am taking the native oxide to be the layer of Mn₃O₄ that develops naturally under ambient conditions. When freshly synthesized particles were allowed to oxidize naturally during the washing steps extremely small values of tens of Oersteds were measured. This is in stark contrast with other papers in the literature. For instance, Berkowitz *et al.* measured H_{ex} and H_c to be about 1800 Oe and 3800 Oe, respectively, for their similarly sized (but less monodispersed) 26-28 nm MnO|Mn₃O₄ particles cooled to 10 K in after cooling in a 50 kOe field. They specifically state that particles were not oxidized at high temperature, but we do not preclude the formation of a stable Mn₃O₄ shell prior to their measurements.³⁷ For similarly sized 23.7 nm MnO|Mn₃O₄ particles with a shell thickness of 5.7 nm, Salazar-Alvarez *et al.* report H_{ex} and H_c values of about 1800 Oe and 5400 Oe, respectively, at 10 K after cooling in a 50 kOe field. These particles were cooled to room temperature before being exposed to air.³⁸ Our measurements on particles maintained under inert atmosphere until reaching room temperature and oxidized naturally during the washing process gave H_{ex} and H_c values two orders of magnitude lower than those reported by Berkowitz *et al.* and Salazar-Alvarez *et al.* Indeed, after oxidizing for 3 hours at 100 °C, with H_{ex}=585 Oe and H_c=865 Oe, our values are still significantly less. It is natural that there would be some variations in these parameters between particle batches, and different precursors (Berkowitz *et al.* used manganese oleate,³⁷ Salazar-Alvarez *et al.* used manganese acetylacetone,³⁸ and this work used manganese acetate), but a one to two order of magnitude discrepancy warrants closer consideration.

We believe that a significant degree of what has been attributed to large exchange bias and coercive fields in the other published work on the MnO|Mn₃O₄ system is a manifestation of particle defects, spin-glass like behavior, and polycrystallinity, especially in the AFM core. The AFM ordering in MnO is the result of the superexchange interaction in which oxygen ions mediate the exchange interaction between two adjacent Mn moments.³⁹ Because of this particle defects like an oxygen vacancies or grain boundaries have a strong effect on the exchange coupling and could dramatically change the magnetic behavior. It is not unreasonable that defects could cause clusters of several atoms inside the AFM to couple ferromagnetically and thus dramatically change the interface participating in exchange bias. Ferrimagnetism is also mediated by superexchange so the Mn₃O₄ shell will have similar sensitivity to defects.

A spin glass is a material that exhibits frustrated interactions between AFM and FM coupling of spins leading to a complicated energy landscape below a certain critical temperature. Spin glass behavior has been observed in bulk MnO.⁴⁰ The signature of spin glass behavior is a sharp cusp in the susceptibility measured as a function of temperature in a very low field. This sharp feature is not directly observed in nanoparticle systems because of broadening from a distribution surface effects and local strain. Often in nanoparticle systems this complex, frustrated, temperature dependent, magnetic interaction is referred to as spin glass-like behavior. Frustrated magnetic coupling could dramatically change observed exchange bias effects.

A distribution of polycrystalline grain orientations within the AFM could also lead to a change in observed exchange bias behavior. In Hoffman's model thermal training in exchange biased materials is the result of biaxial anisotropy in the AFM.³⁰ He

clearly points out that this comes from the high symmetry of cubic AFM materials and is not manifest in lower symmetry systems. Training effects dramatically increase H_c and H_{ex} of the first hysteresis loop measured after field cooling. In the $\text{MnO}|\text{Mn}_3\text{O}_4$ literature no training experiments have been published and we assume all hysteresis loops to be the virgin loops after field-cooling. If a distribution in AFM easy-axes resulting from the symmetry of a single AFM crystal can cause training, the effects of a polycrystalline AFM or an AFM with defects should be dramatic.

In all of these cases, the large discrepancy between our measured H_{ex} and H_c , and other values in the literature could be explained by the poor crystallinity of the particles synthesized by other groups. Indeed, one reference even presents evidence from the broadening of neutron diffraction peaks that suggests AFM domains of about 9 nm in size inside a 19 nm MnO core.⁴⁴ It is reasonable that as synthesized, our particles are more crystalline than those studied by other groups. Our distribution in particle size is significantly lower, and the Bragg contrast observed in bright field TEM within a single particle is much more uniform than those studied by others. These features tend to be indicative of overall particle crystallinity. Additionally, annealing our particles for 3 hours at 300 °C would only improve the quality. It is curious, however, that oxidizing the particles by bubbling with air at 300 °C for 6 hours results in anomalously high values of H_{ex} and H_c . One possible explanation for this is that a high degree of order must exist in the MnO before oxidation to preserve crystallinity during the oxidation process.

4.3.2 FALSELY ATTRIBUTED EXCHANGE BIAS

There are also many examples in the literature in which the authors incorrectly attribute measured values of H_{ex} and H_c to exchange bias. As a case study, we will examine a recent paper by Hwang *et al.* that claims evidence of exchange bias in $\text{Fe}_3\text{O}_4|\gamma\text{-Fe}_2\text{O}_3$ core-shell nanoparticles.⁴¹ This is an example of a research group very well known for their synthetic prowess making simple errors in trying to explain the magnetism and physics of their particles. Fe_3O_4 (Magnetite) and $\gamma\text{-Fe}_2\text{O}_3$ (Maghemite) are both ferrimagnets and thus cannot have true exchange bias at the interface between them. The measured H_{ex} in this system is significantly higher for samples cooled in a 500 Oe field than for samples cooled in a 50 kOe field. This trend is typically attributed to spin-glass systems,^{42,43} and is opposite to what is observed in exchange biased systems. With access to a very wide range in particle sizes, Hwang *et al.* show very clearly that due to the surface anisotropy term, the total anisotropy of their particles increases for decreasing particle size reaching 60 times the anisotropy of bulk Fe_3O_4 for 2 nm particles.⁴³ This work is an important example because it shows it is possible to have contributions from surface anisotropy and spin-glass behavior that can appear (at least naively) to behave as an exchange biased system. Surface disorder and poor crystallinity could certainly contribute in this way. It also illustrates how readily the surface anisotropy of small particles could dominate the larger particles in a non-monodispersed sample.

In examining exchange bias in core-shell nanoparticle systems it is essential to have monodispersed nanoparticles. The particles synthesized in this paper have a distribution in diameters of <5% calculated as one standard deviation in the diameter

divided by the mean diameter. Salazar-Alvaraz *et al.* claim a <20% distribution in diameters, and their TEM images show a very wide distribution of irregularly shaped particles.³⁸ The two papers by Berkowitz *et al.* do not quote a quantitative size distribution, but the TEM images show a relatively bimodal distribution of particles where the 26-28 nm particles discussed are accompanied by a large amount of 5-15 nm particles.^{16,37} Since smaller particles can have higher coercivity due to the increased contribution of the surface anisotropy term to the total anisotropy, it is entirely reasonable that part of the very large exchange bias and coercivity values reported for these samples comes from the contribution of the smaller particles.

The last possibility we will consider is that the values found in the literature are much larger than the values measured in this paper due to interactions. Berkowitz *et al.* explicitly state that their particles were washed “until they were free of excess surfactant (clear solution, particles readily precipitated).”¹⁶ The work from the Nogués group does not discuss this part of their magnetic sample preparation.^{38,44} This could be a very important detail in the MnO|Mn₃O₄ nanoparticle system as particles washed until the surfactant was completely removed could be very close to their neighbors and the FIM shells may interact via dipolar or even weak exchange interactions. On the other hand particles that retain their surfactant coating are separated by 2-3 nm and interact dipolarly. It is possible that if the favored interparticle interaction is exchange that H_c and H_{ex} could be larger than if the particles interact as dipoles because the lowest energy arrangement for two spins interacting via exchange is parallel and the lowest energy arrangement for two spins interacting dipolarly is anti-parrallel. Further investigation should be done on the role of interactions in exchange biased core-shell nanoparticle systems.

4.4 CONCLUSION

In conclusion, we have demonstrated the development of a novel, highly monodispersed synthesis of MnO nanoparticles. We have also shown that they can be oxidized in a controlled way that allows the tuning of the shell thickness and as a consequence the exchange bias field and coercivity. A method was also developed to self assemble the particles into crystals tens of microns in dimension. We believe this to be the first colloidal crystallization of particles in the ~30 nm size range with most previous work focusing on particles under 10 nm and over 100 nm in size. Finally, we would like to emphasize the importance of high quality, monodispersed nanoparticles in doing repeatable work that can be interpreted with simple models. This is true for all nanoparticle studies, but especially true for exchange biased nanoparticle studies because of the extreme importance of the interface and surface effects. We believe our superior particle quality to be the source of the dramatic disagreement between our measured H_{ex} and H_c and those values typically presented in the literature.

Future work on using polarized small angle neutron scattering (PASANS) to investigate the inter- and intra-particle 3D magnetic structure and interactions of crystallized MnO|Mn₃O₄ particles is underway.

4.5 REFERENCES

-
- ¹ W. H. Meiklejohn , and C.P. Bean, *Phys. Rev.* 120 (1956) 1413.
 - ² "The Nobel Prize in Physics 2007". Nobelprize.org. 19 Aug 2012
http://www.nobelprize.org/nobel_prizes/physics/laureates/2007/
 - ³ C. Walter, *Scientific American* 293 (2005), 32-33.
 - ⁴ S. Gangopadhyay, G. C. Hadjipanayis, C. M. Sorensen, and K. J. Klabunde, *J. Appl. Phys.* 73 (1993), 6964.
 - ⁵ J. B. Tracy, D. N. Weiss, D. P. Dinega, and M. G. Bawendi, *Phys. Rev. B* 72 (2005), 064404.
 - ⁶ I. S. Lee, N. Lee, J. Park, B. H. Kim, Y. W. Yi, T. Kim, T. K. Kim, I. H. Lee, S. R. Paik, and T. Hyeon, *J. Am. Chem. Soc.* 128 (2006) 10658.
 - ⁷ C. Luna, M. P. Morales, C. J. Serna, M. Vazquez, *Nanotechnology* 15 (2004), S293.
 - ⁸ R. K. Zheng, G. H. Wen, X. X. Zhang, *Phys. Rev. B* 69 (2004), 214431.
 - ⁹ P. Z. Si, D. Li, J. W. Lee, C. J. Choi, Z. D. Zhang, D. Y. Geng, and E. Brück, *Appl. Phys. Lett.* 87 (2005) 133122.
 - ¹⁰ M. H. Yu, P. S. Devi, L. H. Lewis, P. Oouma, J. B. Parise, and R. J. Gambino, *Mater. Sci. Eng. B* 103 (2003), 262.
 - ¹¹ R. K. Zheng, H. Liu, X. X. Wang, *Apply Phys. Lett.* 84 (2004), 702.
 - ¹² F. X. Redl, C. T. Black, G. C. Papaefthymious, R. L. Sandstrom, M. Yin, H. Zheng, C. B. Murria, and S. P. O'Brien, *J. Am. Chem. Soc.* 126 (2004), 14583.
 - ¹³ C. J. Bae, Y. Hwang, J. Park, K. An, Y. Lee, J. Lee, T. Hyeon, J. G. Park, *J. Magn. Magn. Mater.* 310 (2007), E806.
 - ¹⁴ M. T. Klem, D. A. Resnick, K. Gilmore, M. Young, Y. U. Idzerda, and T. Douglas, *J. Am. Chem. Soc.* 129 (2007), 197.
 - ¹⁵ G. Salazar-Alvarez, J. Sort, S. Suriñach, M. D. Baró, and J. Nogués, *J. Am. Chem. Soc.* 129 (2007), 9102.
 - ¹⁶ A. E. Berkowitz, G. F. Rodriguez, J. I. Hong, K. An, T. Hyeon, N. Agarwal, D. J. Smith, and E. E. Fullerton, *J. Phys. D: Appl. Phys.* 41 (2008), 134007.
 - ¹⁷ I. V. Golosovsky, G. Salazar-Alavarez, A. López-Ortega, M. A. González, J. Sort, M. Estrader, S. Suriñach, M. D. Baró, and J. Nogués, *Phys. Rev. Lett.* 102 (2009), 247201.
 - ¹⁸ K. Dwight, and N. Menyuk, *Phys. Rev.* 119 (1960), 1470.
 - ¹⁹ C. G. Shull, and J. S. Smart, *Phys. Rev.* 76 (1949), 1256.
 - ²⁰ A. E. Berkowitz, G. F. Rodriguez, J. I. Hong, K. An, T. Hyeon, N. Agarwal, D. J. Smith, and E. E. Fullerton, *J. Phys. D: Appl. Phys.* 41 (2008), 134007.
 - ²¹ T. Ould-Ely, D. Prieto-Centurion, A. Kumar, W. Guo, W. V. Knowles, S. Asokan, M. S. Wong, I. Rusakova, A. Luttge, and K. H. Witmire, *Chem. Mater.* 18 (2006), 1821-1829.
 - ²² K. An, M. Park, J. H. Yu, H. B. Na, N. Lee, J. Park, S. H. Choi, I. C. Song, W. K. Moon, T. Hyeon, *Eur. J. Inorg. Chem.* (2012), 2148-2155.
 - ²³ T. Arii, A. Kishi, M. Ogawa, and Y. Sawada, *Anal. Sci.* 17 (2001), 875.
 - ²⁴ M. Yin, and S. O'Brien, *J. Am. Chem. Soc.* 125 (2003), 10180.
 - ²⁵ Collaboration: Authors and editors of the volumes III/17G-41D: *MnO: phase diagram, crystal structure, lattice parameters*. Madelung, O., Rössler, U., Schulz, M. (ed.).

-
- SpringerMaterials - The Landolt-Börnstein Database
(<http://www.springermaterials.com>). DOI: 10.1007/10681735_449
- ²⁶ I. Rusakova, *et al.*, *Chem. Mater.* 19 (2007), 1369-1375.
- ²⁷ Collaboration: Authors and editors of the volumes III/17G-41D: *Mn₃O₄: lattice parameters*. Madelung, O., Rössler, U., Schulz, M. (ed.). SpringerMaterials - The Landolt-Börnstein Database (<http://www.springermaterials.com>). DOI: 10.1007/10681735_462
- ²⁸ A. J. Barker, B. Cage, S. Russek, and C. R. Stoldt, *J. Appl. Phys.* 98 (2005), 063528.
- ²⁹ B. Kaeswurm and K. O'Grady, *Appl. Phys. Lett.* 99 (2011), 222508.
- ³⁰ A. Hoffman, *Phys. Rev. Lett.* 93 (2004), 097203-1.
- ³¹ J. D. Watson and F. H. C. Crick, *Cold Spring Harb Symp Quant Biol.* 18 (1953), 123-131.
- ³² C. B. Murray, C. R. Kagan, M. G. Bawendi, *Science* 270 (1995), 1335-1338.
- ³³ D. V. Talapin, E. V. Shevchenko, A. Kornowski, N. Gaponik, M. Hasse, A. L. Rogach, H. Weller, *Adv. Mater.* 13, No. 24 (2001), 1868.
- ³⁴ E. Shevchenko, D. Talapin, A. Kornowski, F. Wiekhorst, J. Kotzler, M. Hasse, A. Rogach, H. Weller, *Adv. Mater.* 14, No. 4 (2002), 287.
- ³⁵ D. F. Farrell, Y. Ijiri, C. V. Kelly, J. A. Borchers, J. J. Rhyne, Y. Ding, S. A. Majetich, *J. Magn. Magn. Mater.* 303 (2006), 318-322.
- ³⁶ B. Faure, G. Salazar-Alvarez, and L. Bergström, *Langmuir* 27 (2011), 8659-8664.
- ³⁷ A. E. Berkowitz, G. F. Rodriguez, J. I. Hong, K. An, T. Hyeon, N. Agarwal, D. J. Smith, and E. E. Fullerton, *Phys Rev. B* 77 (2008) 024403.
- ³⁸ G. Salazar-Alvarez, J. Sort, S. Suriñach, M. D. Baró, and J. Nogués, *J. Am. Chem. Soc.* 129 (2007), 9102-9108.
- ³⁹ P. W. Anderson, *Phys. Rev.* 79 (1950), 350.
- ⁴⁰ J. J. Hauser, and J. V. Waszczak, *Phys. Rev. B* 30 (1984), 5167.
- ⁴¹ Y. Hwang, S. Angappane, J. Park, K. An, T. Hyeon, and J. Park, *Curr. Appl. Phys.* 12 (2012), 808-811.
- ⁴² L. del Bianco, D. Fiorani, A. M. Testa, E. Bonetti, L. Signorini, *Phys. Rev. B* 70 (2004), 052401.
- ⁴³ H. Wang, T. Zhu, K. Zhao, W. N. Wang, C. S. Wang, Y. J. Wang, W. S. Zhan, *Phys. Rev. B*. 70 (2004), 082409.
- ⁴⁴ A. López-Ortega, D. Tobia, E. Winkler, I. V. Golosovsky, G. Salazar-Alvarez, S. Estradé, M. Estrader, J. Sort, M. A. González, S. Suriñach, J. Arbiol, F. Peiró, R. D. Zysler, M. D. Baró, and J. Nogués, *J. Am. Chem. Soc.* 132 (2010), 9398-9407.

Chapter 5

Conclusions

5.1 SUMMARY OF RESULTS

Throughout the course of this work, we have presented the results from studies of inter- and intra-particle interactions in magnetic nanoparticle assemblies. In Chapter 2, this included efforts to modify the Langevin function—which is only applicable in the superparamagnetic realm where nanoparticles are non-interacting—to include interparticle interactions in the superferromagnetic realm. We modified the Langevin function to include a local demagnetizing field, but it only fit experimentally measured 6.7 nm Fe₃O₄ nanoparticle crystals for large values of the local demagnetizing field and was considered unphysical.

Fits of our experimental magnetization curves to an interaction model recently proposed by Al-Saei *et al.*, which includes an even distribution of positive and negative dipolar interaction fields,¹ gave physically reasonable values for the dipolar field distributions. After using Monte Carlo calculations to model a three dimensional distribution of dipolar interaction fields, Al-Saei *et al.* simplified their model so that it only includes dipolar interaction fields in the applied field direction so it could be more easily compared with experiment. Based on Figure 2.14, our work suggests that although it would practically difficult to apply, experimental data would more accurately match the model when dipolar interaction fields are included in all three dimensions.

We further investigated the nature of interactions orthogonal to the applied magnetic field in magnetization measurements by developing a data processing route that allowed for the qualitative measurement of a magnetic moment perpendicular to the applied magnetic field in our SQUID magnetometer. We believe this to be the first application of the transverse measurement coils in a SQUID magnetometer for the measurement of a magnetic nanoparticle system. Strong qualitative agreement was found between the measured transverse moment and the deviations between both the effective demagnetizing field and dipolar distribution field models from the experimental longitudinal (parallel to the applied magnetic field) magnetization curves. This suggests that a model, like that proposed by Al Saei *et al.*, which incorporates dipolar interaction fields perpendicular to the applied magnetic field may accurately describe magnetic nanoparticle interactions in the superferromagnetic regime.

In Chapter 3, we introduced the development of polarization analyzed small angle neutron scattering (PASANS) and its application to measurements of the intraparticle

magnetic structure in nanoparticle crystals of 9 nm Fe₃O₄ particles. To date, this work has resulted in four publications.^{2,3,4,5} The PASANS experiments demonstrated that from 160 to 320 K in an applied field of 1.2 T, the 9 nm particles had a 7 nm core with spins oriented along the applied magnetic field and a 1.0 to 1.5 nm thick shell in which the spins are coherently oriented perpendicular to the magnetic shell as illustrated in Figure 3.11.5. We believe that the striking perpendicular orientation of the shell, in which the perpendicular orientation direction is coherent over several particles, is the result of competing surface anisotropy and dipolar interactions. This measurement of this structure provides evidence that the simple monodomain model often applied to nanoparticles is not strictly correct under certain conditions. Under the conditions probed, it also disproves many theoretically proposed arrangements of the surface spins on magnetic nanoparticles.^{6,7,8,9,10}

In Chapter 4, we presented the development of a novel synthesis for MnO nanoparticles and outlined a procedure for their controlled oxidation and the subsequent creation of an epitaxial Mn₃O₄ shell of variable thickness. Our values for the exchange and coercive fields were significantly lower than those presented in the literature for similar MnO|Mn₃O₄ core shell nanoparticle systems. We attribute this discrepancy to a combination of the high crystallinity and narrow size distribution of our particles. It is proposed that defects in the MnO core of particles studied by other groups lead to magnetic frustration and spin-glass-like behavior that manifests itself as exchange bias.

5.2 FUTURE WORK

We are involved in discussions with the Roy Chantrell group to further develop the application of the model they proposed in Ref. 1 for the distribution of dipolar interaction fields to our experimental measurements. We will be preparing our work fitting their interaction field model and the simpler effective demagnetizing field model to our experimental data for publication. While there are many publications proposing models for interactions in magnetic nanoparticle systems, and many experimental measurements of magnetic nanoparticle systems, direct applications of a model to experimental data are scarce. We hope the publication of the results presented in Chapter 2 will help fill this void.

The results presented in Chapter 3 will also be developed for publication. We hope to show that defects in core/shell exchange biased nanoparticle systems can lead to dramatically overestimated exchange bias parameters. Additionally, we plan to apply the PASANS technique to investigate the local spins at the AFM/FiM interface in the MnO|Mn₃O₄ system. As discussed in Chapter 3, the PASANS technique is perfectly suited for the investigation of magnetic structure on this length scale, and the extremely large interfacial area in a core/shell nanoparticle assembly presents an ideal sample. It is our hope that this study will help clarify the understanding of the fundamental physics involved in the exchange bias phenomenon.

5.3 REFERENCES

-
- ¹ J. Al Saei, M. El-Hilo, and R. W. Chantrell, *J. Appl. Phys.* 110 (2011), 023902.
 - ² K. L. Krycka, J. A. Borchers, R. A. Booth, C. R. Hogg, Y. Ijiri, W. C. Chen, S. M. Watson, M. Laver, T. R. Gentile, S. Harris, L. R. Dedon, J. J Rhyne, and S. A. Majetich, *J. Appl. Phys.* 107 (2010), 09B525.
 - ³ K. L. Krycka, R. A. Booth, J. A. Borchers, W. C. Chen, C. Conlon, T. R. Gentile, C. Hogg, Y. Ijiri, M. Laver, B. B. Maranville, S. A. Majetich, J. J. Rhyne, and S. M. Watson, *Physica B* 404 (2009) 2561-2564.
 - ⁴ K. Krycka, J. Borchers, Y. Ijiri, R. Booth, and S. Majetich, *J. Appl. Cryst.* 45 (2012), 554-565.
 - ⁵ K. L. Krycka, R. A. Booth, C. R. Hogg, Y. Ijiri, J. A. Borchers, W. C. Chen, S. M. Watson, M. Laver, T. R. Gentile, L. R. Dedon, S. Harris, J. J. Rhyne, and S. A. Majetich, *Phys. Rev. Lett.* 104 (2010) 207203.
 - ⁶ R. Yanes, O. Chubykalo-Fesenko, H. Kachkachi, D. A. Garanin, R. Evans, R. W. Chantrell, *Phys. Rev. B* 76 (2007) 064416.
 - ⁷ J. Mazo-Zuluaga, J. Restrepo, and J. Majía-López, *Physica (Amsterdam)* 398B (2007), 187.
 - ⁸ J. Mazo-Zuluaga, J. Restrepo, F. Munoz, J. Mejia-Lopez, *J. Appl. Phys.* 105 (2009), 123907.
 - ⁹ L. Berger, Y. Labaye, M. Tamine, and J. M. D. Coey, *Phys. Rev. B* 77 (2008), 104431.
 - ¹⁰ Y. Hu and A. Du, *J Nanosci. Nanotechnol.* 9 (2009), 5829.

APPENDIX I

SQUID Magnetometer Sample Preparation

This guide is designed to help guide those not familiar in SQUID magnetometer measurements to prepare successful samples. For nearly all measurements, samples should be prepared inside of a plastic drinking straw. The drinking straws that our group uses are about 0.5 cm in diameter and 19.5 cm in length. The drinking straw will be taped on the end of a sample rod and lowered into the sample chamber inside the SQUID's cryostat.

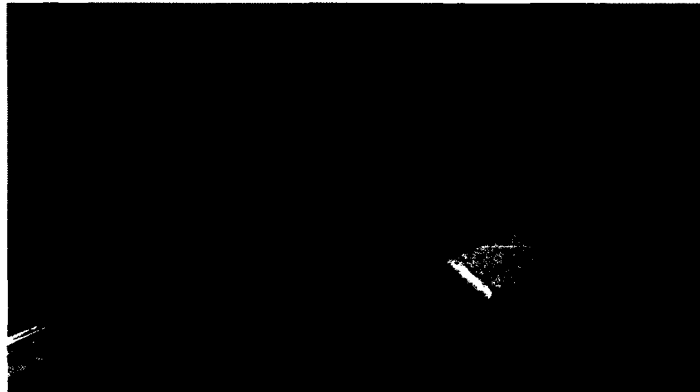


Figure A1.1: Empty drinking straw attached to sample rod.

I will elaborate on techniques for different sample types later, but in preparing samples for successful, low noise measurements several general considerations are very important.

1. The SQUID can measure the magnetic moment of a sample directly. Our SQUID is sensitive to moments between 1.0×10^{-6} and 1.0 emu. The lower end of this range is problematic because diamagnetic and paramagnetic contributions from the sample holder are of the same order of magnitude as the sample. If you must make a measurement in the low end of this range it is very important to prepare your sample carefully and it might be necessary to do background subtraction. Ideally, a sample's moment falls somewhere in

the middle of this range. In making your sample please estimate the amount of magnetic material so that the signal will fall in this range.

2. To make a measurement the SQUID magnetometer moves a sample through a set of superconducting second-derivative pickup coils. These coils were cleverly arranged by Quantum Design so that their chirality automatically cancels constant and linearly changing flux through them. Thus, in an ideal situation, the SQUID only records the flux due to the sample moving through the coils. We can take advantage of this to help minimize noise in measurements and increase the regression value when fitting the SQUID voltage as a function of sample position to that of an ideal dipole.

For these reasons symmetry in a sample is very important. Any material that you put on or in the straw (i.e. other pieces of straw, tape, gelatin capsules...) above the sample should be a mirror image of the material below the sample.

3. Most materials used to make sample holders have a diamagnetic response. Efforts should be made to minimize this diamagnetism. Large amounts of polymer, epoxy, wax, resin, etc... are especially problematic. If you must use materials like this use as little as possible and be sure they are arranged symmetrically above and below your sample.
4. The longitudinal coils of the SQUID magnetometer interpret any sample less than 3.0 mm tall as a point dipole. The accuracy of measurements with samples taller than this will suffer because the response cannot be fit to that of an ideal dipole. In addition, the vertical distribution of the sample is important. Ideally all of a sample lies exactly in a cross-sectional plane of the drinking straw. Great care should be taken to prepare samples to meet this requirement.
5. Please make sure that your sample is secured in such a way that it will not move in large applied magnetic fields or fall out of the drinking straw and contaminate our sample chamber. Also, before being inserted into the sample chamber of the magnetometer, the sample passes through an airlock which is repeatedly evacuated and then purged with helium gas. Your sample should be prepared in such a way that this cycle will not damage it.

Most magnetic samples exist either as liquids, powders, or thin films. I will treat preparation of samples for each of these separately.

1. Liquid: If your sample exists in a liquid form (such as a suspension of nanoparticles) it is best to dry them and make a sample from their powder. One of my favorite ways to do this is to put very small drops of the liquid in a the outer half of a gelatin capsule. To keep the vertical spread of the sample small it is important to do this in very small amounts ($\sim 10 \mu\text{L}$) at a time and allowing the liquid to dry completely between drops. After this is complete, the sample can be immobilized in the gelatin capsule by inverting the inner piece of the capsule and nesting it inside the larger piece. This nested arrangement should then be mirrored below the sample to maintain symmetry. Gelatin capsules fit very nicely inside a drinking straw.

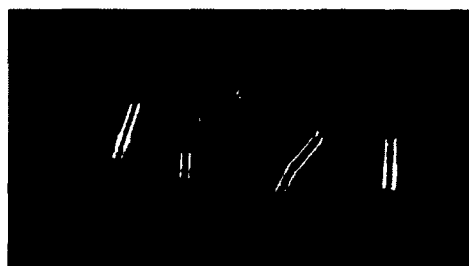


Figure A1.2: Left to right, disassembly and nesting of gelatin capsule.

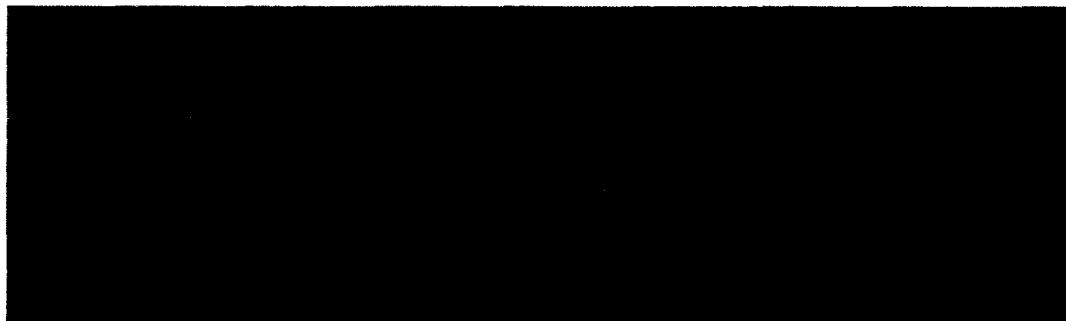


Figure A1.3: Assembled sample prepared with gelatin capsules. Notice that the nested capsules containing the sample open to the right. Underneath, opening to the left is an empty set of nested capsules to increase the symmetry of the diamagnetic contribution from the gelatin capsules. Above and below the capsules folded pieces of drinking were inserted into the main straw to support sample. Please take note of the approximate position of the sample inside the straw.

If your sample must remain in the liquid form during a measurement it must be sealed under vacuum inside a glass or quartz ampoule. It is important to seal it under vacuum to avoid a paramagnetic contribution from any enclosed oxygen. The glass of the ampoule should be as uniform as possible. Large gobs of glass on the bottom of the ampoule should be especially avoided because of the asymmetric diamagnetic contribution. Glass and quartz have

similar susceptibilities, but quartz has the advantage of a relatively constant susceptibility over a wide range of temperatures. Ampoules should be a size that can easily fit inside a straw. Please note that the liquid must be frozen during measurement.



Figure A1.4: Glass ampoule with liquid sample taped inside drinking straw.

2. Powder: Use gelatin capsules and follow same procedure as drying a liquid. A powder can usually be packed nicely into the outer half of a gelatin capsule by using the inner half as a tamper. The powder can also be secured by the nesting the inner half in the outer half.
3. Wafer or thin Film: A wafer or thin film can simply be taped to the outside of a drinking straw using Kapton tape for measurements in which the magnetic field is applied in-plane. Kapton tape maintains its stickiness over a very wide range of temperatures and has a relatively low susceptibility that is mostly constant as a function of temperature. For out of plane measurements cut a small piece of drinking straw that can fit inside the main drinking straw. Tape your sample to that piece. Fold the small piece with the sample on it and insert it into the drinking straw. Support that small piece so that your sample is parallel to a cross section of the drinking straw. For support you may use smaller, folded pieces of straw inserted longitudinally into the main drinking straw.



Figure A1.5: Wafer taped to straw for in-plane measurement.



Figure A1.6: Example of a small piece of straw with a sample taped to it supported inside main straw with folded pieces of straw. Use this arrangement or similar technique for out of plane measurements.

Sample preparation is one of the most important aspects of making a successful measurement with the SQUID magnetometer. Since the SQUID needs very expensive liquid helium to run it is desirable not to have to repeat measurements due to bad sample preparation. Therefore, it is worthwhile to invest time in careful preparation before making a measurement. Following this guide should help a great deal in that process. For additional information and techniques consult the application notes on Quantum Design's website (<http://www.qdusa.com/resources/index.html>).

APPENDIX II

Transverse SQUID Measurement Details

A2.1 INTRODUCTION

Most magnetometers measure the magnetic moment of a sample in the direction of the applied magnetic field. This is referred to as the longitudinal direction. Measurements of the magnetic moment in the longitudinal geometry are the most commonly made magnetization measurement by a wide margin. Our Quantum Design, Magnetic Properties Measurement System (MPMS), super conducting quantum interference device (SQUID) magnetometer also has an option to measure the magnetic moment transverse to the applied field. The transverse magnetic moment is typically much smaller than the longitudinal magnetic moment, so proper data analysis requires the careful treatment of instrumental artifacts. This appendix will describe the origins of these artifacts, how to minimize them prior to a measurement, and how to correct for them after a measurement.

A2.2 DETECTION COILS

Before explaining the transverse pickup coils, it is best to develop an understanding of the more straightforward longitudinal pickup coils, which are pictured in Figure A2.1a. The magnetic moment of a sample is calculated by measuring the current generated by the flux of a magnetic sample as it moves longitudinally through the coils in both the longitudinal and transverse geometry.

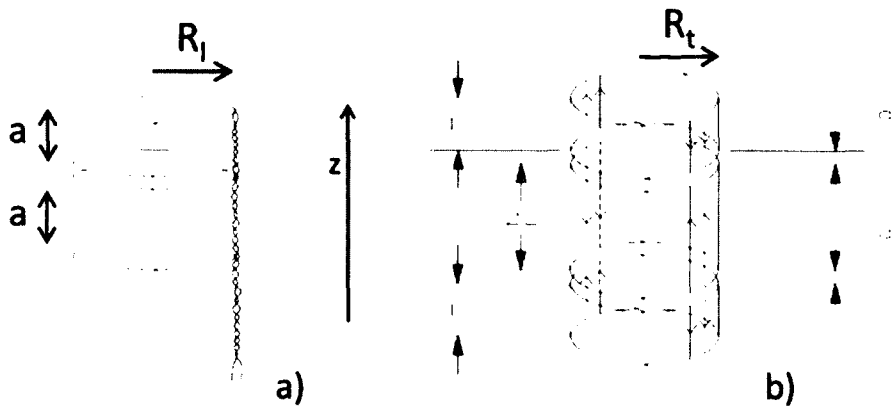


Figure A2.1: Diagrams of the a) $R_l=0.97$ cm radius, longitudinal pickup coils and b) the $R_t=0.8$ cm radius transverse pickup coils for the MPMS SQUID magnetometer. $L=0.97$ cm, $d=0.0508$ cm, and $a=1.529$ cm.¹ (Reproduced from Ref. 2 and modified).

Both the longitudinal, and transverse pickup coils are second derivative coils, which are designed to reject both uniform, and linearly varying magnetic fields by nature of the coil chirality.² The chirality of the loops is indicated by the arrows in the diagram. Faraday's law gives the expression for the electromotive force generated by a time varying flux through surface as,

$$\varepsilon = -\frac{d\phi_B}{dt}, \quad (\text{A2.1})$$

where ε is the electromotive force, and ϕ_B is the flux. The direction of the electromotive force relative to the flux is given by Lenz's law, and indicated by the minus sign in Eq. A2.1. The sign of the flux comes from the direction of the area vector as shown in Eq. A2.2,

$$\phi_B = \iint_{\Sigma(t)} \mathbf{B}(\mathbf{r}, t) \cdot d\mathbf{A}, \quad (\text{A2.2})$$

where $\mathbf{B}(\mathbf{r}, t)$ is the magnetic field which is integrated over the time varying surface $\Sigma(t)$ with area vector \mathbf{A} . The direction of \mathbf{A} in this case depends on the direction of the coil winding following the right-hand rule convention as shown in Figure A2.2.

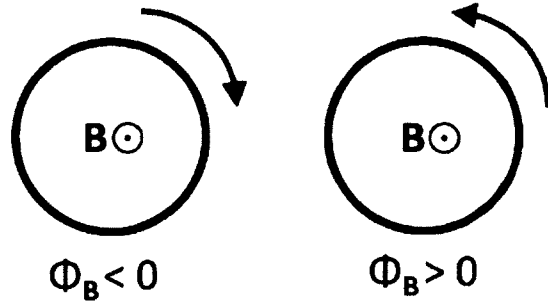


Figure A2.2: Illustration of the magnetic flux sign convention. In the context of the SQUID detection coils, the arrow indicates the chirality of a given loop.

The detection loops are wired in series for both the transverse and longitudinal pickup coils. The sign of the electromotive force governs how the currents induced in the individual loops add; the signal is proportional to the net current generated in the detection coils by the motion of the sample. It can be easily seen that a uniform magnetic field in the longitudinal pickup coils would not generate a net current because the current generated by the outer loops cancels the current generated by the inner loops.

The net current generated in the detection coils is measured by the SQUIDs and converted to a signal voltage. The signal voltage generated by a point dipole moving longitudinally (in the z -direction) through the longitudinal pickup coils can be calculated exactly. The signal generated in an individual coil is,

$$v_l(z) = \frac{1}{(R_l^2 + z^2)^{3/2}} , \quad (\text{A2.3})$$

where $R_l=0.97$ cm is the radius of the longitudinal pickup coil, and z is the longitudinal position of the point dipole pointing in the $+z$ direction, where $z=0$ is the center of the longitudinal pickup coil assembly. The contribution of the individual loops is added, including their chirality and longitudinal separation, $a=1.529$ cm, to give the total longitudinal signal:

$$V_l(z) = 2v_l(z) - v_l(z-a) - v_l(z+a) . \quad (\text{A2.4})$$

An example of an ideal longitudinal signal is shown in Figure A2.3. The magnetic moment of a sample is proportional to the amplitude of the response signal. The instrument software typically takes the center of the pickup coils to be $z=2$ cm as a matter of convention. This is not reflected in the fit functions given in this appendix.

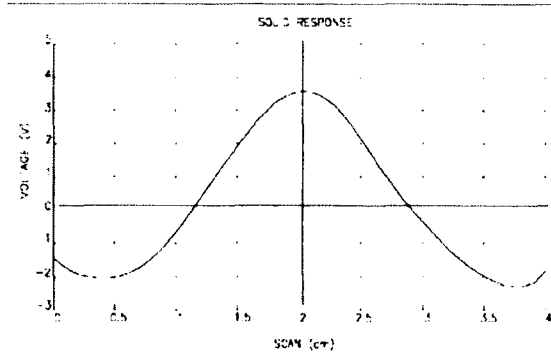


Figure A2.3: Ideal longitudinal SQUID response voltage, $V_l(z)$, to a centered, longitudinal, point dipole. Note that the center of the pickup coils is taken to be $z=2$ cm. (Reproduced from Ref. 2)

The transverse SQIUD response to a point dipole oriented in the transverse direction was modeled using MATHCAD software by Quantum Design.¹ The signal generated in one loop is,

$$v_t(\alpha) = \frac{\pi}{R_t^2} \left[\frac{\alpha(4\alpha^2 + 6R_t^2 - R_t\sqrt{\alpha^2 + R_t^2})}{(\alpha^2 + R_t^2)^{3/2}} - \text{atan}\left(\frac{\alpha}{R_t}\right) \right]. \quad (\text{A2.5})$$

The contribution of each loop is combined, including the location as the argument α , and the loop chirality, to calculate the total signal generated in the transverse detection coils as,

$$V_t(z) = -[v_t(2L + d - z) - v_t(L + d - z)] + [v_t(L - z) - v_t(-L - z)] - [v_t(-2L - d - z)], \quad (\text{A2.6})$$

where $L=0.97$ cm, $R_t=0.8$ cm, and $d=0.0508$. The ideal transverse SQUID response voltage is shown in Figure A2.4.

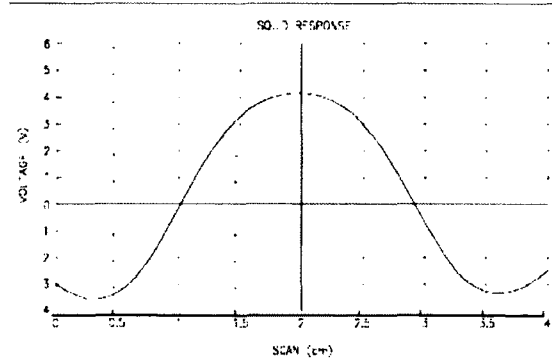


Figure A2.4: Ideal transverse SQUID response voltage, $V_t(z)$, to a centered, transverse, point dipole. Note that the center of the pickup coils is taken to be $z=2$ cm. (Reproduced from Ref. 2).

The transverse SQUID coils also have a sensitivity that varies with the direction of the transverse moment in the x,y-plane. Because of the gap in the coils there is a sinusoidal dependence with zero SQUID response resulting from a transverse moment oriented in the y-direction toward the gap, and the maximum SQUID response resulting from a transverse moment oriented in the x-direction, toward the center of the coils. These arrangements are shown in Figure A2.5. This rotational dependence is one of the many reasons that it is difficult to obtain quantitative measurements of the transverse magnetization. We will only focus on qualitative results. Prior to a measurement of the transverse moment, the sample is rotated to maximize the signal.

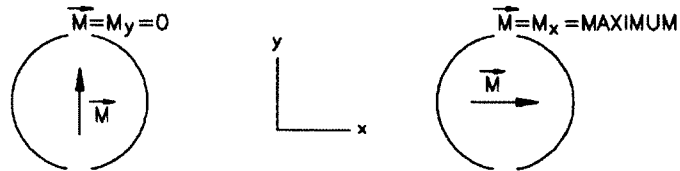


Figure A2.5: A transverse moment oriented in the y-direction does not generate a signal. A transverse moment oriented in the x-direction, towards the center of the pickup coils generates the maximum signal. (Reproduced from Ref. 2).

A2.2 TRANSVERSE ARTIFACTS

Ideally, the longitudinal and transverse pickup coils are perfectly orthogonal. Therefore a longitudinal measurement cannot measure a transverse moment, and a transverse measurement cannot measure a longitudinal moment. For a perfectly centered sample containing both longitudinal and transverse magnetization components, there is a very small leakage of the longitudinal moments into the transverse measurement, and likewise, the transverse measurements into the longitudinal moment. This is due to two factors. First, the longitudinal and transverse pickup coils are not perfectly orthogonal. Quantum Design estimates this uncertainty to be about 1%.² Because of this, there will always be some slight leakage between the longitudinal and transverse channels. Additionally, because the wires connecting the pickup coils in both directions consist of twisted pairs, as illustrated explicitly in Figure A2.1a, flux passing through the helical wire generates some signal. In the transverse measurement, this artifact dominates only at high fields. Although they can be significant, neither of these artifacts dominate the transverse measurements we discussed in this thesis.

In our measurements, the longitudinal moment is significantly larger than the transverse moment, and it is impossible to center the sample perfectly. These two factors combine to create the dominant artifact in our transverse measurement. As illustrated in Figure A2.6, a longitudinal moment that is perfectly centered radially in the pickup coils

does not contribute to the transverse signal because the flux through the coils (1) and (2), and the flux between coils (5) and (6) cancel. When the sample is at $z=0$, no transverse flux is generated in coils (3) and (4) because there is not a net component of the magnetic field parallel to the area vector after integrating over the coil area. As the sample moves through the coils along the z -axis, the flux through the coils always cancels completely.

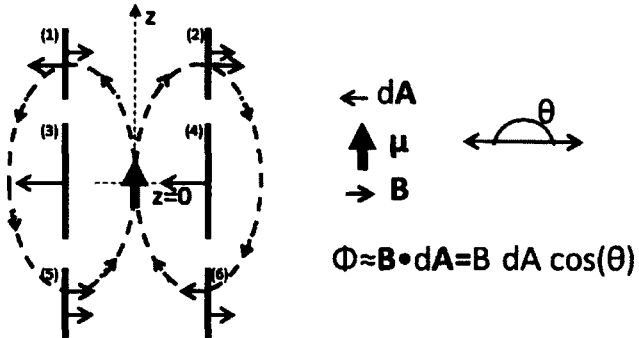


Figure A2.6: Diagram of flux generated by a perfectly centered longitudinal point dipole. The angle between the area vector, dA , and the enclosed magnetic field, B , defines the sign of the magnetic flux, Φ . Their product defines the magnitude.

If a longitudinal moment isn't perfectly centered, as in most real systems, it can generate a net transverse magnetic flux. This is illustrated in Figure A2.7. Notice the magnitude of the B -field. Notice that coils (1) and (2), and coils (5) and (6) no longer cancel and a net flux is generated.

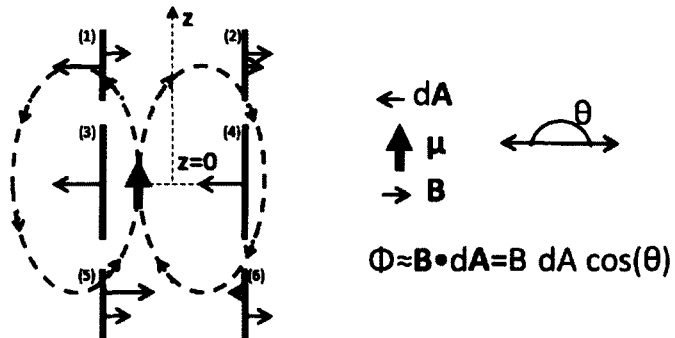


Figure A2.7: Diagram of flux generated by an off-center, longitudinal point dipole. The angle between the area vector, dA , and the enclosed magnetic field, B , defines the sign of the magnetic flux, Φ . Their product defines the magnitude.

Luckily, the symmetry of the transverse signal along the z -axis, about $z=0$, is different for a purely transverse moment and an off-center longitudinal moment. A

longitudinal moment that is not centered produces an odd response as shown in Figure A2.8.

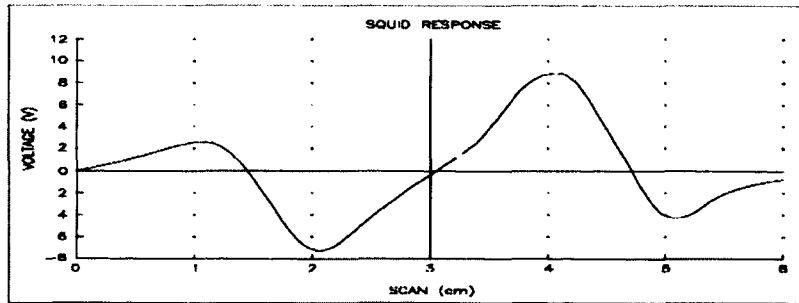


Figure A2.8: Transverse SQUID response to an off-center longitudinal moment from a measurement of a nickel sphere. The response is the combination of small, functionally even contribution from a transverse component, and a functionally odd contribution from the off center longitudinal component. (Reproduced from Ref 2).

A true transverse moment always produces an even response about $z=0$. This is illustrated schematically in Figure A2.9; notice that none of the fluxes cancel as in the perfectly centered longitudinal case. An example of the even transverse response is shown in Figure A2.4.

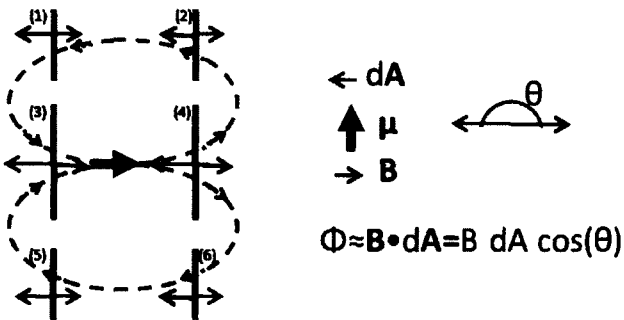


Figure A2.9: Schematic of the transverse pickup coil response to a transverse moment. The sign is the same for the flux through each coil.

A2.3 REMOVAL OF TRANSVERSE ARTIFACTS

To extract the transverse signal from a response dominated by an off-center longitudinal artifact, we take advantage of the odd symmetry of the artifact and the even symmetry of the signal. Naively, one might consider taking the magnitude of the SQUID response at $z=0$ as proportional to the transverse moment. While it would be the simplest way to remove the artifacts, blindly taking the value of the transverse magnitude at $z=0$

does not allow one to see the full transverse response function. It is useful to examine the full response function to understand the limitations of a data set because deviations of the experimental response from the fit to the ideal transverse response inform the rejection of low confidence data.

If the sample is well centered along the z-axis of the response coils, the separation of the even and odd functional components is simple:

$$f_{odd}(z) = \frac{1}{2}[f(z) - f(-z)] \quad (\text{A2.7})$$

$$f_{even}(z) = \frac{1}{2}[f(z) + f(-z)]. \quad (\text{A2.8})$$

If the sample is not well centered, the same procedure can be used but it is then necessary to iterate through the range of possible center positions and use the center position with the optimum fit of the experimental response to the ideal transverse response. After separating the artifacts, the amplitude of the fit to the ideal transverse response function (Eq. A2.6) is proportional to the transverse moment.

A2.4 CONCLUSION

In conclusion, we have described the longitudinal and transverse pickup coils for the MPMS SQUID magnetometer. The nature and symmetry of artifacts encountered when measuring the transverse moment of a sample with a much larger, off-center longitudinal moment were discussed. A procedure was given for the separation of artifacts and the fitting of the transverse moment.

A2.5 REFERENCES

¹ Private communication with Jim O'Brien of Quantum Design Inc.

² MPMS Application Note, 1014-202 A (2000).